Gas Heating Inside Radio Sources
to Mildly Relativistic Temperatures
via Induced Compton Scattering

S. Yu. Sazonov[1, 2]* and R. A. Sunyaev[1, 2]

[1] *Space Research Institute, Russian Academy of Sciences, Profsoyuznaya ul. 84/32, Moscow, 117810 Russia*
[2] *Max-Planck-Institut für Astrophysik, Karl Schwarzschild Strasse 1, Garching bei München, 86740 Germany*

Abstract—The measured brightness temperatures of the low-frequency synchrotron radiation from intense extragalactic sources reach 10^{11}–10^{12} K. If there is some amount of nonrelativistic ionized gas within such sources, it must be heated through induced Compton scattering of the radiation. If cooling via inverse Compton scattering of the same radio radiation counteracts this heating, then the plasma can be heated up to mildly relativistic temperatures $kT \sim 10$–100 keV. In this case, the stationary electron velocity distribution can be either relativistic Maxwellian or quasi-Maxwellian (with the high-velocity tail suppressed), depending on the efficiency of Coulomb collisions and other relaxation processes. We derive several simple approximate expressions for the induced Compton heating rate of mildly relativistic electrons in an isotropic radiation field, as well as for the stationary electron distribution function and temperature. We give analytic expressions for the kernel of the integral kinetic equation (one as a function of the scattering angle, and the other for an isotropic radiation field), which describes the photon redistribution in frequency through induced Compton scattering in thermal plasma. These expressions can be used in the parameter range $h\nu \ll kT \lesssim 0.1mc^2$ [in contrast to the formulas written out previously in Sazonov and Sunyaev (2000), which are less accurate]. © *2001 MAIK "Nauka/Interperiodica"*.

Key words: *active galactic nuclei, quasars, and radio galaxies*

1. INTRODUCTION

According to milliarcsecond-resolution interferometric radio observations, individual components of the central parsec-scale regions in active galactic nuclei (AGNs) are often sources of low-frequency radiation with rest-frame brightness temperatures $T_b \sim 10^{11}$–10^{12} K. If there were thermal plasma in these regions, it could be effectively heated through induced Compton scattering of the radio radiation by electrons (Levich and Sunyaev 1971). Such plasma has not yet been observed in extragalactic sources. On the other hand, there is evidence that relatively cold matter accounts for a significant fraction of the total mass contained in the jets, including their inner ($\leq 10^{12}$ cm) regions, of the well-known Galactic source SS 433 [see Vermeulen (1992) for a review]. Of course, these jets are only mildly relativistic ($v \sim 0.26c$) and, therefore, differ greatly from the relativistic jets in AGNs, whose bulk Lorentz factors are $\gamma \sim 5$. Nevertheless, it would be reasonable to

expect that some amount of quasi-thermal plasma can also be present in extragalactic jets (see, e.g., Celotti *et al.* 1998).

A formula for the induced Compton heating rate of thermal electrons in an isotropic radiation field can be derived directly from the Kompaneets kinetic equation (Levich and Sunyaev 1971). However, this formula is applicable only when the electron temperature is relatively low: $kT \lesssim$ several keV. As the electrons become more relativistic, their heating rate monotonically decreases. Theoretical studies in the 1970s (Vinogradov and Pustovalov 1972; Blandford 1973; Blandford and Scharlemann 1975) yielded several useful formulas that allow one to calculate the heating rate of relativistic electrons and their distribution function in various limits, for example, for ultrarelativistic electrons, for narrow radiation beams, or for peculiar radiation spectra. Illarionov and Kompaneets (1976) derived a general expression for the heating rate of an electron moving at an arbitrary velocity in an isotropic radiation field. However, this formula is complex: for the heating rate of an ensemble of electrons with a given velocity distri-

* E-mail address for contacts: ss@hea.iki.rssi.ru

bution (e.g., Maxwellian) to be determined, a three-dimensional integral must be calculated.

Here, we show that electrons can be heated by Compton scattering up to mildly relativistic temperatures $kT \sim$ several tens of keV, but no more, in an isotropic radiation field with $T_b < 10^{12}$ K. For such plasma temperatures, nonrelativistic estimates of the heating rate and certain relevant quantities are inaccurate. However, as we show below, these expressions can be improved by adding several correction terms, with the simple structure characteristic of the original expressions being retained.

It should be noted that although only AGNs were mentioned above, induced Compton heating could play a major role in other astrophysical objects as well. Note also that the problem of plasma heating near, but outside, sources of low-frequency radiation requires a special study.

2. HEATING AND COOLING OF THERMAL ELECTRONS DURING COMPTON SCATTERING

Let us derive formulas for the rates of heating and cooling of mildly relativistic thermal electrons ($kT \lesssim 0.1mc^2$, where T is the electron temperature) in an isotropic radiation field through spontaneous and induced Compton scattering.

The radiation field can be defined in terms of its spectral energy density, ϵ_v (measured in erg cm^{-3} Hz^{-1}), or, equivalently, in terms of the occupation number in photon phase space, $n = \epsilon_v c^3/(8\pi h v^3)$. We require that the spectrum be sufficiently broad; i.e., its characteristic width $\Delta v/v$ should be much larger than the typical fractional photon frequency shift during a scattering event produced either by the Doppler effect, $\sim \pm(kT/mc^2)^{1/2}$, or by Compton recoil, $\sim -hv/mc^2$. In this case, the integral kinetic equation describing the time evolution of ϵ_v (due to the Compton interaction of the radiation with electrons) can be transformed to a Fokker–Planck-type differential equation. In the limit kT, $hv \ll mc^2$, we arrive at the equation of Kompaneets (1956).

The expressions for the electron heating and cooling rates (Levich and Sunyaev 1971), which are fairly accurate for electron and photon energies $\lesssim 0.01mc^2$, can be derived from the Kompaneets equation. The Kompaneets equation can be generalized to the mildly relativistic range of parameters (kT, $hv \lesssim 0.1mc^2$) by adding relativistic correction terms $\sim (kT/mc^2)^m (hv/mc^2)^n$ (Itoh *et al.* 1998; Challinor and Lasenby 1998; Sazonov and Sunyaev 2000). For example, the first-order generalized Kompaneets equation (which is derived by Fokker–Planck-type expansion of the integral kinetic equation to the fourth order in Δv) is

$$\frac{\partial n}{\partial t} = \frac{\sigma_T N_e h}{mc} \frac{1}{v^2} \frac{\partial}{\partial v} v^4 \left\{ n(1+n) + \frac{kT}{h} \frac{\partial n}{\partial v} \right.$$

$$+ \frac{7}{10} \frac{hv^2}{mc^2} \frac{\partial n}{\partial v} + \frac{kT}{mc^2} \left[\frac{5}{2} \left(n(1+n) + \frac{kT}{h} \frac{\partial n}{\partial v} \right) \right.$$

$$+ \frac{21}{5} v \frac{\partial}{\partial v} \left(n(1+n) + \frac{kT}{h} \frac{\partial n}{\partial v} \right) + \frac{7}{10} v^2 \left(-2 \left(\frac{\partial n}{\partial v} \right)^2 \right.$$

$$\left. \left. + 2(1+2n) \frac{\partial^2 n}{\partial v^2} + \frac{kT}{h} \frac{\partial^3 n}{\partial v^3} \right) \right] \right\}, \quad (1)$$

where σ_T is the Thomson cross section and N_e is the electron number density. Multiplying Eq. (1) by hv and integrating over photon phase space yields an expression for the change in total radiation energy density $\epsilon = \int_0^\infty \epsilon_v dv$ and, at the same time, for the change in mean electron energy $E_e \approx 1.5kT(1 + 1.25kT/mc^2)$:

$$-\frac{1}{N_e} \frac{\partial \epsilon}{\partial t} = \frac{dE_e}{dt} = \frac{8\pi\sigma_T h}{c^2} \left[-4 \frac{kT}{mc^2} \int_0^\infty v^3 n \, dv \right.$$

$$+ \frac{h}{mc^2} \int_0^\infty v^4 (n + n^2) dv - 10 \left(\frac{kT}{mc^2} \right)^2 \int_0^\infty v^3 n \, dv$$

$$- \frac{21}{5} \left(\frac{h}{mc^2} \right)^2 \int_0^\infty v^5 n \, dv + \frac{kT}{mc^2} \frac{h}{mc^2} \left(\frac{47}{2} \int_0^\infty v^4 (n + n^2) dv \right.$$

$$\left. \left. - \frac{21}{5} \int_0^\infty v^6 \left(\frac{\partial n}{\partial v} \right)^2 dv \right) \right]. \quad (2)$$

The first two terms in the square brackets in Eq. (2) describe the electron heating and cooling rates in the nonrelativistic limit (Peyraud 1968; Zel'dovich and Levich 1970; Levich and Sunyaev 1971). The additional terms are relativistic corrections of the order of kT/mc^2 or hv/mc^2. Note that the correction to the heating rate associated with the induced Compton effect (the corresponding terms are nonlinear in n) includes a term that is expressed in terms of the derivative squared, $(\partial n/\partial v)^2$. The higher order $[(kT/mc^2)^2$, etc.] corrections to the rate of energy transfer through the induced Compton effect, which are not written out in Eq. (2), depend on the higher order derivatives of n, as is explicitly shown below (in Section 3).

The rate of energy transfer between electrons and blackbody radiation of temperature T_r can be found from Eq. (2):

$$\frac{d\epsilon}{dt} = 4\epsilon\sigma_T N_e c \left(\frac{kT}{mc^2} - \frac{kT_r}{mc^2} \right) \left(1 + \frac{5}{2} \frac{kT}{mc^2} - 2\pi^2 \frac{kT_r}{mc^2} \right). \quad (3)$$

This expression was originally derived (in a different way) by Woodward (1970).

Note that the problem of energy transfer between radiation and thermal plasma via spontaneous Compton scattering has been extensively studied and the corresponding part of Eq. (2) directly follows from the first moment of the Compton scattering kernel (Shestakov *et al.* 1988; Sazonov and Sunyaev 2000; also see the appendix). We are concerned with the terms that describe the contribution of induced scattering.

3. INDUCED COMPTON HEATING OF THERMAL ELECTRONS

Intense extragalactic radio sources emit low-frequency continuum radiation, which, in some cases, has a very high brightness temperature, $T_b = nh\nu/k \sim 10^{11}$–$10^{12}$ K, i.e., $kT_b > mc^2$. Induced Compton scattering can be a major heating mechanism for free electrons in such a radiation field. Moreover, nonrelativistic estimates lead one to conclude that electrons can be heated up to relativistic temperatures: $kT \sim$ fractions of kT_b (Levich and Sunyaev 1971). Clearly, the nonrelativistic treatment is unsuitable here. Below, we show that, in reality, only mildly relativistic electron temperatures (i.e., kT is considerably less than mc^2) are reachable in this situation. As a result, all the relevant physical quantities can be described by simple analytic expressions.

Below, we consider an isotropic radiation field. In this section, we also assume a relativistic Maxwellian distribution of electrons (which can be maintained, e.g., by Coulomb collisions). This assumption is relaxed in Section 4.

The rate of energy transfer by induced Compton scattering from an isotropic radiation field to an electron moving at velocity $v = \beta c$ is given by (Illarionov and Kompaneets 1976)

$$W^+(\beta) = \frac{12\pi\sigma_T h^2}{mc^4}\int_0^\beta \Phi(y')G(\beta, \beta')d\beta',$$

$$\Phi(y) = \int_0^\infty n(\nu)n(y\nu)\nu^4 d\nu,$$

$$G(\beta, \beta') = \frac{\beta'^2}{\gamma^5\beta^8(1+\beta')^5}\Big[(30 - 24\beta^2 + 2\beta^4)\ln\frac{y'}{y}$$
$$+ 28\beta^3 - 60\beta + 5(3 - \beta^2)^2\beta' + (5 - \beta^2)(3 + \beta'^2)\beta'\Big(\frac{\gamma'}{\gamma}\Big)^2\Big], \quad (4)$$

$$y = \frac{1-\beta}{1+\beta}, \quad y' = \frac{1-\beta'}{1+\beta'},$$

$$\gamma = (1-\beta^2)^{-1/2}, \quad \gamma' = (1-\beta'^2)^{-1/2}.$$

Eq. (4) is valid for arbitrary electron velocities provided that $h\nu \ll mc^2$. This formula can be simplified in some limits, in particular, for narrow spectral emission lines ($\Delta\nu \ll \nu$), such as those formed in cosmic masers and laboratory lasers (Vinogradov and Pustovalov 1972; Blandford and Scharlemann 1975). Instead, we are interested in the $\Delta\nu \gtrsim \nu$ case.

For the instantaneous heating rate of an actual plasma to be calculated, Eq. (4) must be weighted with a given electron velocity distribution f_β. Consequently, calculating the heating rate involves taking a three-dimensional integral: (1) over the radiation spectrum [when calculating $\Phi(y')$], (2) over $d\beta'$, and (3) over f_β. However, if the electrons obey a relativistic Maxwellian distribution and are only mildly relativistic ($kT \lesssim 0.1mc^2$), the calculational procedure can be significantly simplified by reducing it to integration over the radiation spectrum, as shown below.

If $kT \lesssim 0.1mc^2$, then $\beta \lesssim 0.5$ for most electrons; therefore, the typical (random) Doppler frequency shift due to a single scattering is relatively small: $\delta\nu \lesssim \nu$. The function $\Phi(y')$ in Eq. (4) can then be expanded in a Taylor series:

$$\Phi(y') = \int_0^\infty n^2\nu^4 d\nu + (y'-1)\int_0^\infty n\frac{\partial n}{\partial\nu}\nu^5 d\nu$$
$$+ \frac{1}{2}(y'-1)^2\int_0^\infty n\frac{\partial^2 n}{\partial\nu^2}\nu^6 d\nu + ..., \quad (5)$$

where, in turn,

$$y' - 1 = -2\beta' + 2\beta'^2 + ...,$$
$$\frac{1}{2}(y'-1)^2 = 2\beta'^2 + ..., \quad (6)$$

etc. A similar expansion is possible for the kernel $G(\beta, \beta')$ of Eq. (4):

$$G = \frac{4}{\beta}\Big[\Big(\frac{\beta'}{\beta}\Big)^3 - 2\Big(\frac{\beta'}{\beta}\Big)^5 + 2\Big(\frac{\beta'}{\beta}\Big)^7\Big]$$
$$+ 20\Big[-\Big(\frac{\beta'}{\beta}\Big)^4 + 2\Big(\frac{\beta'}{\beta}\Big)^6 - 2\Big(\frac{\beta'}{\beta}\Big)^8\Big] + ... \quad (7)$$

The subsequent straightforward calculations lead to

$$W^+(\beta) = \frac{\sigma_T c^2}{8\pi m}\Big[J_0 + \Big(-\frac{17}{30}J_0 - \frac{7}{5}J_1\Big)\beta^2$$
$$+ \Big(-\frac{47}{600}J_0 + \frac{17}{150}J_1 + \frac{11}{30}J_2\Big)\beta^4 + \Big(-\frac{899}{19600}J_0$$
$$+ \frac{2833}{29400}J_1 + \frac{4261}{14700}J_2 - \frac{64}{1575}J_3\Big)\beta^6 + ...\Big], \quad (8)$$

$$J_0 = \int\limits_0^\infty \epsilon_\nu^2 \nu^{-2} d\nu, \quad J_1 = \int\limits_0^\infty \left(\frac{\partial \epsilon_\nu}{\partial \nu}\right)^2 d\nu,$$

$$J_2 = \int\limits_0^\infty \left(\frac{\partial^2 \epsilon_\nu}{\partial \nu^2}\right)^2 \nu^2 d\nu, \quad J_3 = \int\limits_0^\infty \left(\frac{\partial^3 \epsilon_\nu}{\partial \nu^3}\right)^2 \nu^4 d\nu.$$

Note that the Planck constant h is absent from Eq. (8), which reflects the well-known fact that induced Compton scattering is a classical process (see, e.g., Zel'dovich 1975).

Next, we replace β^2, β^4, and β^6 in Eq. (8) by their means $\langle\beta^2\rangle$, $\langle\beta^4\rangle$, and $\langle\beta^6\rangle$ calculated for a mildly relativistic Maxwellian distribution with temperature T, which is given by (see, e.g., Sazonov and Sunyaev 2000)

$$f_\beta = \left(\frac{2\pi kT}{mc^2}\right)^{-3/2}\left[1 + \frac{15}{8}\frac{kT}{mc^2} + \frac{105}{128}\left(\frac{kT}{mc^2}\right)^2\right.$$

$$-\frac{315}{1024}\left(\frac{kT}{mc^2}\right)^3 + \dots\left.\right]^{-1}\left(1 + \frac{5}{2}\beta^2 - \frac{3}{8}\frac{\beta^4 mc^2}{kT} + \frac{35}{8}\beta^4\right.$$

$$-\frac{5}{4}\frac{\beta^6 mc^2}{kT} + \frac{9}{128}\frac{\beta^8 m^2 c^4}{k^2 T^2} + \frac{105}{16}\beta^6 - \frac{345}{128}\frac{\beta^8 mc^2}{kT} \tag{9}$$

$$+\frac{75}{256}\frac{\beta^{10} m^2 c^4}{k^2 T^2} - \frac{9}{1024}\frac{\beta^{12} m^3 c^6}{k^3 T^3} + \dots\left.\right)\exp\left(-\frac{\beta^2 mc^2}{2kT}\right).$$

As a result, the heating rate as a function of the plasma temperature is

$$W^+(T) = \frac{\sigma_T c^2}{8\pi m}\left[J_0 - \left(\frac{17}{10}J_0 + \frac{21}{5}J_1\right)\frac{kT}{mc^2}\right.$$

$$+\left(\frac{123}{40}J_0 + \frac{61}{5}J_1 + \frac{11}{2}J_2\right)\left(\frac{kT}{mc^2}\right)^2 \tag{10}$$

$$-\left(\frac{1989}{280}J_0 + \frac{453}{14}J_1 + \frac{1899}{140}J_2 + \frac{64}{15}J_3\right)\left(\frac{kT}{mc^2}\right)^3 + \dots\left.\right],$$

where J_0, J_1, J_2, and J_3 were introduced in Eq. (8).

For cold electrons ($kT \ll mc^2$), only the first term of the series in powers of kT/mc^2 in Eq. (10) is important, and the heating rate due to induced Compton scattering is described by the well-known formula (Zel'dovich and Levich 1970; Levich and Sunyaev 1971)

$$W_0^+ = \frac{\sigma_T c^2}{8\pi m}\int\limits_0^\infty \epsilon_\nu^2 \nu^{-2} d\nu. \tag{11}$$

Both the nonrelativistic expression (11) and the first-order relativistic correction to it [see Eq. (10)] were already derived in Section 2 by a using a different approach [see Eq. (2)]. Thus, two independent approaches yield the same result.

3.1. Heating in the Field of Self-Absorbed Synchrotron Radiation

Let us now consider one particular spectral distribution, namely, the spectrum of synchrotron radio emission with self-absorption at low frequencies. The radiation spectrum generated by a spherically symmetric homogeneous source is given by (Gould 1979)

$$\epsilon_\nu^0(\nu) = A\left(\frac{\nu}{\nu_0}\right)^{5/2}\left[\frac{1}{2} + \frac{\exp(-t)}{t} - \frac{1 - \exp(-t)}{t^2}\right], \tag{12}$$

$$t = \left(\frac{\nu_0}{\nu}\right)^{0.5p + 2}.$$

The shape of the distribution (12) is described by a single parameter, p, which is the index of the power-law energy distribution of the electrons that produce the synchrotron radiation: $dN_e \sim \gamma^p d\gamma$. The other two parameters ν_0 and A that appear in Eq. (12) determine the position of the spectrum along the frequency axis and its amplitude, respectively. Far enough from the intensity peak ($\nu_{peak} \approx 1.15\nu_0$), the spectrum (12) assumes a power-law shape: $\epsilon_\nu^0 \sim \nu^{5/2}$ in the region of self-absorption ($\nu \ll \nu_0$) and $\epsilon_\nu^0 \sim \nu^{(1-p)/2}$ in the optically thin part ($\nu \gg \nu_0$).

Since the integral $\epsilon = \int_0^\infty \epsilon_\nu^0 d\nu$ diverges at infinity for $p \leq 3$, and this quantity determines the Compton cooling rate, which we will take into account below, we modify Eq. (12) as follows:

$$\epsilon_\nu(\nu) = \begin{cases} \epsilon_\nu^0(\nu), & \nu \leq \nu_b \\ (\nu/\nu_b)^{-0.5}\epsilon_\nu^0(\nu), & \nu > \nu_b. \end{cases} \tag{13}$$

Here, we assume that the spectrum steepens (the slope increases by 0.5) above some (break) frequency $\nu_b \gg \nu_0$ due to the fast synchrotron cooling of more energetic electrons.

For definiteness, we assume the slope of the optically thin part of the spectrum (before the break) to be $\alpha = -0.7$, which corresponds to $p = 2.4$. We additionally take $\nu_b = 10^3\nu_0$ as a tentative value in our treatment of electron cooling, although this parameter just enters in the relevant formulas as a multiplicative factor as long as $\nu_b \gg \nu_0$. The resulting spectrum is shown in Fig. 1. Note that mechanisms other then synchrotron self-absorption, including free–free absorption in the ambient medium (see, e.g., Bicknell *et al.* 1997) and induced Compton scattering outside or inside the radio source (see, e.g., Sunyaev 1971; Sincell and Krolik 1994; Kuncic *et al.* 1998), are occasionally proposed to account for the low-frequency breaks observed in the spectra of some radio sources. However, the radiation field inside the source that we are concerned with may

well be the superposition of the self-absorbed synchrotron spectra generated by individual plasma components.

In Fig. 2a, the heating rate of thermal electrons in the field of self-absorbed synchrotron radiation is plotted against electron temperature. The exact result was obtained by weighting the heating rate for monoenergetic electrons given by Eq. (4) with the relativistic Maxwellian distribution,

$$dN_e = \text{const}\gamma(\gamma^2 - 1)^{1/2}\exp(-\gamma mc^2/kT)d\gamma.$$

We additionally confirmed this dependence by Monte Carlo simulations using the Comptonization code described in Pozdnyakov *et al.* (1983) with a slight modification to allow for induced Compton scattering. The computation proves to be faster with the semi-analytic formula (4) of Illarionov and Kompaneets. Also shown in Fig. 2a are the various approximations for the heating rate that result from retaining a different number of temperature terms in Eq. (10).

We see that the heating rate begins to decrease appreciably (>5%) at $kT \sim 5$ keV. The temperature range in which this decrease is described well by the approximate relation (10) extends to $kT \sim 30$ keV, when the heating rate is already smaller by $\sim 30\%$ than that for cold electrons. The further decrease in heating rate that takes place at even higher temperatures cannot be properly described in terms of the Fokker–Planck approximation, which was used to derive Eq. (10). The exact dependence presented in Fig. 2a is convenient to describe by an approximate formula, which is accurate to within 3% for $kT < 5\ mc^2$:

$$W^+(T) = \left\{0.8\exp\left[-3.7\left(\frac{kT}{mc^2}\right)^{0.8}\right]\right.$$

$$\left.+ 0.2\exp\left[-1.8\left(\frac{kT}{mc^2}\right)^{0.6}\right]\right\}W_0^+, \tag{14}$$

where, as follows from Eqs. (11) and (12),

$$W_0^+ = 1.1 \times 10^{24} A^2 \nu_0^{-1}\ \text{eV s}^{-1} \tag{15}$$

(A and ν_0 are measured in erg $\text{Hz}^{-1}\ \text{cm}^{-3}$ and GHz, respectively).

It is worth noting that the heating rate approaches an asymptote $W^+(T) \sim (mc^2/kT)^3$ when $kT \gg mc^2$. This is because only the lower energy part of the relativistic Maxwellian distribution, i.e., electrons with $\gamma \lesssim 1$, contribute significantly to the net heating rate (since $W^+ \sim \gamma^{-5}$ for $\gamma \gg 1$; see Illarionov and Kompaneets 1976), and the relative number of such electrons is proportional to $(mc^2/kT)^3$.

Although we chose a particular slope (-0.7) for the optically thin part of the radiation spectrum, it turns out that the dependence of the heating rate on electron temperature changes very slowly with slope. Quantita-
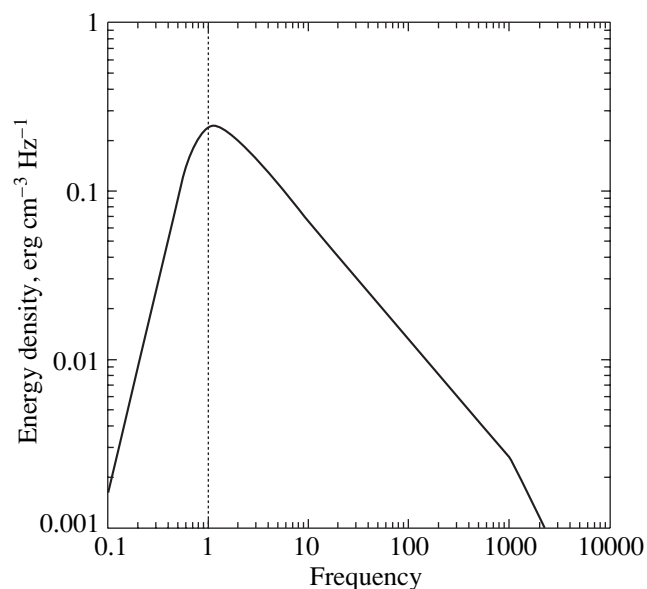
Fig. 1. The radiation spectrum of a self-absorbed synchrotron source described by Eqs. (12) and (13). The frequency is measured in units of the characteristic frequency ν_0.
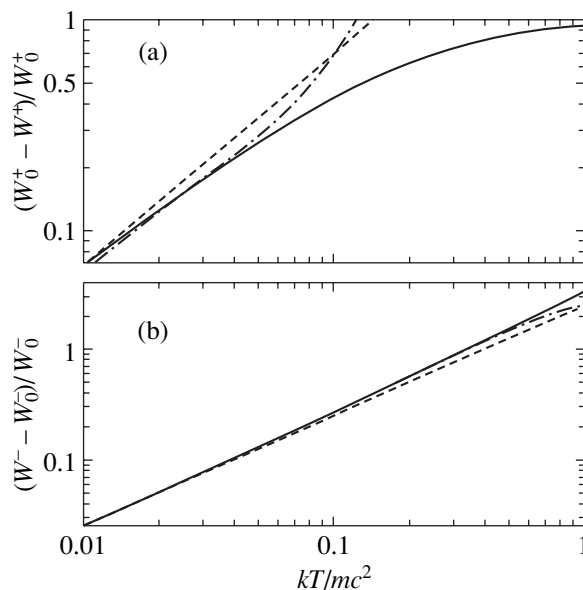

Fig. 2. (a) Deviation of the induced Compton heating rate of Maxwellian electrons in an isotropic field of self-absorbed synchrotron radiation from the nonrelativistic estimate W_0^+ (11) versus temperature. The solid line represents the exact result obtained by weighting Eq. (4) with the relativistic Maxwellian distribution. The dashed and dash–dotted lines represent the results of our calculations using the mildly relativistic formula (10) in which only the correction term $O(kT/mc^2)$ and all the quoted terms up to $O((kT/mc^2)^3)$ were retained, respectively. (b) Deviation of the inverse Compton cooling rate from the nonrelativistic estimate $W_0^-(T)$ (19). The solid line represents the exact result (17). The dashed and dash–dotted lines represent the results of our calculations using the mildly relativistic formula (20).

tively, $W^+(T)$ remains constant to within 10% for α in the range $[-0.9; -0.5]$. Thus, formula (14) is quite useful, because it yields reasonably good estimates for the heating rate of essentially relativistic Maxwellian electrons in an isotropic field of self-absorbed synchrotron radiation.

Of course, the mildly relativistic Eq. (10), which is applicable when $kT \lesssim 30$ keV, explicitly depends on the spectral shape, so it can be used to calculate the heating rate for an arbitrary (broad) radiation spectrum.

3.2. Stationary Electron Temperature

Zel'dovich and Levich (1970) studied, in the nonrelativistic approximation, the problem on the establishment of a stationary distribution of electrons during their interaction with an isotropic field of low-frequency radiation with a high brightness temperature. These authors proved that if cooling through inverse (spontaneous) Compton scattering counteracts induced Compton heating, then the stationary distribution will be Maxwellian with a temperature

$$kT_{eq}^0 = \frac{c^3}{32\pi\epsilon}\int_0^\infty \epsilon_\nu^2 \nu^{-2} d\nu, \qquad (16)$$

where $\epsilon = \int_0^\infty \epsilon_\nu\, d\nu$.

It is reasonable to suggest that only small deviations from the Maxwellian distribution will arise in the mildly relativistic limit. Moreover, if other mechanisms, for example Coulomb collisions, play a significant role in the redistribution of electrons in momentum space, then the Maxwellian distribution can easily be maintained. We postpone a detailed discussion of the questions pertaining to the electron distribution until Section 4; for now, we assume, as we did before, that the electrons obey the relativistic Maxwellian distribution and determine the stationary electron temperature by assuming inverse Compton scattering (of the same low-frequency synchrotron radiation that heat the electrons) to be the only cooling mechanism. Other possible cooling mechanisms that may turn out to be more important under certain conditions will be mentioned in Subsection 3.3.

The inverse Compton cooling rate is given by (see, e.g., Pozdnyakov *et al.* 1983)

$$W^-(T) = \left(\langle\gamma\rangle + \frac{kT}{mc^2}\right)W_0^-(T), \qquad (17)$$

where the mean electron energy (in units of mc^2) is

$$\langle\gamma\rangle = \frac{3kTK_2(mc^2/kT) + mc^2 K_1(mc^2/kT)}{2kTK_1(mc^2/kT) + mc^2 K_0(mc^2/kT)}. \qquad (18)$$

Here, $K_p(x)$ are the modified Bessel functions, and the cooling rate in the nonrelativistic limit ($kT \ll mc^2$) is

$$W_0^-(T) = \frac{4\sigma_T \epsilon kT}{mc}. \qquad (19)$$

We can expand Eq. (17) in powers of kT/mc^2 to derive a formula similar in structure to the corresponding relation for the heating rate (10), which is applicable in the mildly relativistic limit:

$$W^-(T) = \frac{4\sigma_T \epsilon kT}{mc^2}\left[1 + \frac{5kT}{2mc^2} + \frac{15}{8}\left(\frac{kT}{mc^2}\right)^2 - \frac{15}{8}\left(\frac{kT}{mc^2}\right)^3 + \dots\right]. \qquad (20)$$

An excellent fit to the exact formula (17) in the range $kT \lesssim 5\ mc^2$ is given by

$$W^-(T) = \left[1 + 3.4\left(\frac{kT}{mc^2}\right)^{1.1}\right]W_0^-(T), \qquad (21)$$

where W_0^- is defined in (19).

The dependences $W^-(T)$ described by Eqs. (17) and (20) are plotted in Fig. 2b. They may be compared with the corresponding dependences for the heating rate (Fig. 2a). Note that, in contrast to $W^+(T)$, the relation $W^-(T)$, of course, does not depend on the shape of the radiation spectrum (it depends only on the total energy density).

We can now calculate the equilibrium electron temperature by solving the equation $W^+(T_{eq}) = W^-(T_{eq})$. For this to be done, we must determine the constant A appearing in Eq. (12), which specifies the amplitude of the spectral distribution. It is natural to express this coefficient in terms of the maximum brightness temperature $T_b^{max} = \max[\epsilon_\nu(\nu)c^3/(8\pi\nu^2)]$. T_b peaks at $\nu^{max} = 0.61\nu_0$ for $\alpha = -0.7$ (although the peak position depends only slightly on α for the observed radiation spectra of extragalactic radio sources). As a result, we obtain

$$A \approx 22\pi kT_b^{max}\nu_0^2/c^3. \qquad (22)$$

In Fig. 3, equilibrium electron temperature T_{eq} is plotted against T_b^{max}. The exact result is compared with that in the nonrelativistic approximation (16) and with the different-order mildly-relativistic estimates obtained by equating Eqs. (10) and (20). We see that the nonrelativistic Eq. (16) remains valid for $T_{eq} \lesssim 5$ keV, which, in our case, corresponds to brightness temperatures $T_b^{max} \lesssim 3 \times 10^{10}$ K. In this regime,

$$kT_{eq}^0 = 1.9\frac{T_b^{max}}{10^{10}\ K}\left(\frac{\nu_b}{1000\nu_0}\right)^{-0.33}\ keV. \qquad (23)$$

The next decade of equilibrium temperatures, up to $kT_{eq} \sim 40$ keV, is well described by the approximate formulas (10) and (20). Note that $kT_{eq} = 40$ keV corre-

sponds to $T_b^{max} \sim 4 \times 10^{11} \times (\nu_b/1000\nu_0)^{0.33}$ K. The following important conclusion can be reached: electrons can be heated up to mildly relativistic temperatures $kT \sim$ several keV through the induced Compton scattering of synchrotron radiation with $T_b \sim 10^{11}$–10^{12} K but not above these temperatures.

3.3. Evolution of the Electron Temperature during Compton Interaction

Let us now consider a related timing problem; more specifically, let us examine how rapidly electrons can be heated to mildly relativistic temperatures through induced Compton scattering.

We will first estimate the basic characteristic quantities in the nonrelativistic limit. Substituting A from Eq. (22) in Eq. (15) yields

$$W_0^+ = 1.4 \times 10^{-9} \left(\frac{T_b^{max}}{10^{11} \text{ K}}\right)^2 \left(\frac{\nu_0}{1 \text{ GHz}}\right)^3 \text{ e Vs}^{-1}. \quad (24)$$

If there were no cooling, then the initially cold electrons would acquire a kinetic energy kT_{eq}^0 given by Eq. (23) in the time

$$t_{heat} = \frac{kT_{eq}^0}{W_0^+}$$

$$= 1.4 \times 10^{13} \left(\frac{T_b^{max}}{10^{11} \text{ K}}\right)^{-1} \left(\frac{\nu_0}{1 \text{ GHz}}\right)^{-3} \left(\frac{\nu_b}{1000\nu_0}\right)^{-0.33} \text{ s.} \quad (25)$$

We see that the heating time depends strongly on the characteristic frequency of the synchrotron self-absorption: $t_{heat} \sim \nu_0^{-3}$.

The corresponding cooling rate can be derived from Eq. (19):

$$W_0^-(T) \quad (26)$$

$$= 3.8 \times 10^{-8} \frac{kT}{mc^2} \frac{T_b^{max}}{10^{11} \text{ K}} \left(\frac{\nu_0}{1 \text{ GHz}}\right)^3 \left(\frac{\nu_b}{1000\nu_0}\right)^{-0.33} \text{ e Vs}^{-1}.$$

In the mildly relativistic regime, the heating and cooling rates are, respectively, lower and higher than those given by Eqs. (24) and (26). We computed the evolution of the electron temperature for several T_b^{max} by integrating the differential equation

$$\frac{dT}{dt} = \left(\frac{d\langle\gamma\rangle(T)}{dT}\right)^{-1} \frac{W^+(T) - W^-(T)}{mc^2} \quad (27)$$

using Eq. (18) to describe the dependence $\langle\gamma\rangle(T)$ and the fitting formulas (14) and (21) for $W^+(T)$ and $W^-(T)$, respectively. The resulting time histories are presented
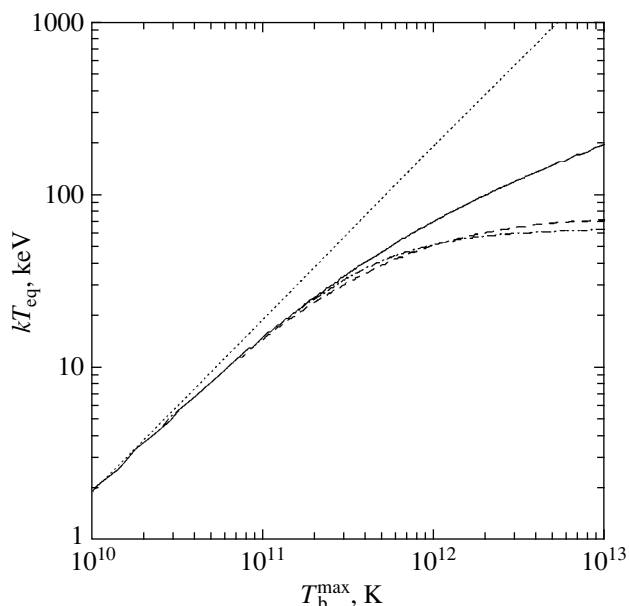
Fig. 3. Stationary electron temperature versus peak brightness temperature. This dependence results from the balance $W^+(T_{eq}) = W^-(T_{eq})$, where $W^+(T)$ and $W^-(T)$ are plotted in Fig. 2. The notation is the same as in Fig. 2. Also shown (dotted line) is the nonrelativistic result (16) or (23).

in Fig. 4, where $\nu_0 = 1$ GHz was used. For a given ν_0, the time axis in Fig. 4 should be simply rescaled as $(\nu_0/1 \text{ GHz})^{-3}$.

Each of the time histories in Fig. 4 can be divided into two intervals. During the first period, the temperature increases linearly, because $W^+ \gg W^-$. After T becomes $\gtrsim 0.5T_{eq}$, the second (longer) period begins, during which the cooling plays a major role and the temperature slowly approaches its equilibrium value. This transition period is additionally lengthened by relativistic effects (compare the different solutions in Fig. 4). The characteristic time of induced heating can be defined as the time it takes for the plasma to be heated to $\sim 0.5T_{eq}$. For example, at $T_b^{max} = 10^{12}$ K, it takes $\sim 3 \times 10^4 (\nu_0/1 \text{ GHz})^{-3}$ years to heat the electrons to $kT = 0.5kT_{eq} \sim 34$ keV. If $\nu_0 \sim 10$ GHz, then the heating time becomes ~ 30 years. Interestingly enough, the simple nonrelativistic Eq. (25) gives a good estimate (to within a factor of 2) of the heating time even for T_b^{max} as high as $\sim 10^{13}(\nu_b/1000\nu_0)^{0.33}$ K (naturally, the equilibrium temperature in this case is much lower than its nonrelativistic estimate).

In real situations, mechanisms can operate by which the plasma cools down more effectively than through inverse Compton scattering of the synchrotron radiation. In this case, the cooling rate $W^-(T)$ must be modified accordingly in the above treatment. If the energy density of a possible high-frequency radiation component is larger than that of the low-frequency synchro-
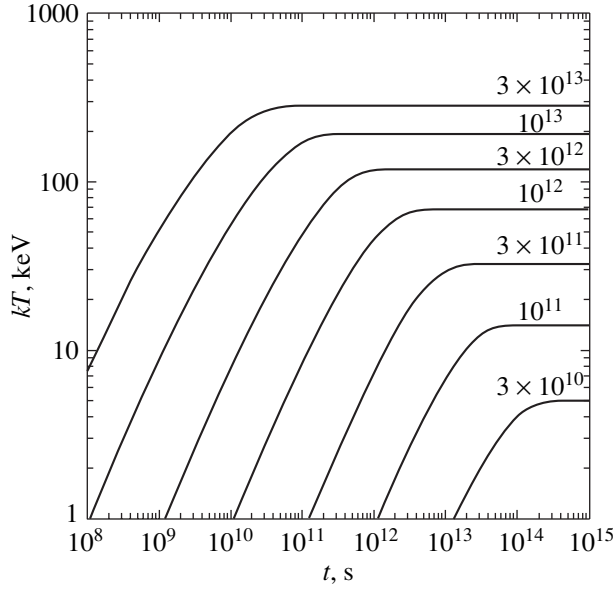
Fig. 4. Evolution of the temperature of Maxwellian electrons during their Compton interaction with self-absorbed synchrotron radiation. The curves are labeled with the corresponding peak brightness temperatures $T_{\rm b}^{\rm max}$ (in K). At time $t = 0$, the plasma is cold.

tron radiation, then the contribution of this component to the inverse Compton cooling rate will be accordingly larger. In addition, cooling through bremsstrahlung will become more important than inverse Compton cooling if the plasma is dense enough, more specifically, when $N_{\rm e} T^{-1/2} \epsilon^{-1} > 10^4$ K$^{-1/2}$ erg^{-1}. For the synchrotron spectrum described by Eqs. (12) and (13), this condition transforms to

$$N_{\rm e} > 6 \left(\frac{T_{\rm b}^{\rm max}}{10^{11}\,{\rm K}} \right)^{3/2} \left(\frac{\nu_0}{1\,{\rm GHz}} \right)^3 \left(\frac{\nu_{\rm b}}{1000\nu_0} \right)^{0.166} {\rm cm}^{-3}.$$

Another possible cooling mechanism is the adiabatic expansion of a plasma cloud. The characteristic time scale for this process is $t_{\rm ad} = 3 \times 10^{10}(R/1\,{\rm pc})(U/10^3\,{\rm km\,s}^{-1})^{-1}$ s, where R is the cloud size and U is the expansion velocity (under the assumption of spherical symmetry).

4. EFFECTS OF INDUCED COMPTON SCATTERING ON THE ELECTRON DISTRIBUTION

We have assumed that the distribution of the electrons in momentum space remains relativistic Maxwellian during their interaction with the low-frequency radiation. This must be the case if the plasma is so dense that electron–electron collisions have time to smooth out any arising deviations from the Maxwellian distribution. In order to find out whether this thermalization actually takes place, it is necessary to compare

the induced Compton heating time $t_{\rm heat}$ (25) with the time scale on which electrons can relax to the Maxwellian distribution (Spitzer 1978),

$$t_{\rm e-e} = 2.5 \times 10^{12} \left(\frac{\ln\Lambda}{40} \right)^{-1} \left(\frac{kT}{mc^2} \right)^{3/2} N_{\rm e}^{-1}\ {\rm s},$$

where $\ln\Lambda$ is the Coulomb logarithm. Taking $T = T_{\rm eq}^0$ (23), we find that the relaxation is effective when

$$\frac{t_{\rm e-e}}{t_{\rm heat}} = 10^{-3} \left(\frac{\ln\Lambda}{40} \right)^{-1} \left(\frac{T_{\rm b}^{\rm max}}{10^{11}\,{\rm K}} \right)^{5/2} \left(\frac{\nu_0}{1\,{\rm GHz}} \right)^3 \left(\left(\frac{\nu_{\rm b}}{1000\nu_0} \right) \right)^{-0.166}$$

$$\times\, N_{\rm e}^{-1} < 1. \tag{28}$$

Let us consider several examples. At $T_{\rm b}^{\rm max} = 10^{11}$ K and $\nu_0 = 1$ GHz, the electron spectrum is Maxwellized if $N_{\rm e} \gtrsim 10^{-3}$ cm^{-3}. For $T_{\rm b}^{\rm max} = 5 \times 10^{11}$ K and $\nu_0 = 10$ GHz, the corresponding range is $N_{\rm e} \gtrsim 10^2$ cm^{-3}. It should be noted here that the high-velocity tail of the Maxwellian distribution is established on a time scale larger than $t_{\rm e-e}$ given above. In the nonrelativistic limit, the corresponding characteristic time is proportional to $(v/\langle v\rangle)^3$ when $v \gg \langle v\rangle$, where v is the electron velocity and $\langle v\rangle$ is the typical thermal electron velocity (see, e.g., Krall and Trivelpiece 1973).

Consider an extreme case where $t_{\rm e-e} \gg t_{\rm heat}$; i.e., no Maxwellization of electrons takes place due to collisions. To find out what momentum distribution $f(p)$ arises in this case, we need to consider the diffusion of electrons in momentum space caused by induced and spontaneous (inverse) Compton scattering. The corresponding Fokker–Planck equation for the electron momentum distribution is (Illarionov and Kompaneets 1976)

$$\frac{\partial f}{\partial t} = \frac{1}{p^2}\frac{\partial}{\partial p} p^2 \left[D\frac{\partial f}{\partial p} - F_{\rm sp}f \right], \tag{29}$$

where the diffusion coefficient

$$D(\beta) = \frac{12\pi\sigma_{\rm T}h^2}{c^4}\int_0^\beta \Phi(y')G_D(\beta, \beta')d\beta',$$

$$G_D(\beta, \beta') = \frac{2\beta'^2}{\gamma^4\beta^8(1+\beta')^5}\left[(3 - \beta^2)\ln\frac{y}{y'} + 2\beta \right. \tag{30}$$

$$\left. -\, 2\beta'\left(\frac{\gamma'}{\gamma} \right)^2 + 2(\gamma^2 + \gamma^{-2})(\beta - \beta') \right],$$

and the breaking force due to spontaneous scattering (Landau and Lifshits 1975) is

$$F_{\rm sp}(\beta) = -\frac{4}{3}\sigma_{\rm T}\epsilon\beta\gamma^2. \tag{31}$$

The electron velocity is related to the electron momentum by

$$\beta = \frac{p}{\gamma mc} = \frac{p}{mc}\left[1 + \left(\frac{p}{mc}\right)^2\right]^{-1/2}. \qquad (32)$$

The remaining quantities in Eqs. (30) and (31) are the same as in Eq. (4).

The cumbersome expression (30) can be simplified by assuming that $\beta \ll 1$. A expansion into a series can then be carried out, which is quite similar to those written out in Section 3 for the induced Compton heating rate:

$$D(\beta) = \frac{\sigma_T c^2}{24\pi}\int\limits_0^\infty \epsilon_\nu^2 \nu^{-2} d\nu$$

$$\times \left[1 + \beta^2\left(\frac{4}{25}\frac{21\int\limits_0^\infty (\partial\epsilon_\nu/\partial\nu)^2 d\nu}{25\int\limits_0^\infty \epsilon_\nu^2 \nu^{-2} d\nu}\right) + \dots\right]. \qquad (33)$$

The equilibrium momentum distribution is given by

$$f_{eq}(p) = \text{const} \times \exp\left[\int\limits_0^p \frac{F_{sp}(p')}{D(p')}dp'\right]. \qquad (34)$$

In the nonrelativistic limit, $D(p) = \text{const}$ and $f_{sp}(p) \sim p$; hence $F_{eq} \sim \exp(-p^2/2mkT_{eq}^0)$, where T_{eq}^0 is given by Eq. (16). Therefore, the equilibrium distribution is Maxwellian in this limit, which was first shown by Zel'dovich and Levich (1970).

The first-order relativistic correction to the nonrelativistic equilibrium distribution can be derived from Eq. (34) by using the approximate expression (33) for the diffusion coefficient and transforming Eq. (31) to

$$F_{sp} = -4/3\sigma_T\epsilon\left(\frac{p}{mc}\right)\left[1 + 0.5\left(\frac{p}{mc}\right)^2 + \dots\right].$$

As a result, we obtain

$$f_{eq}(p) = \text{const} \qquad (35)$$

$$\times \exp\left\{-\frac{p^2}{2mkT_{eq}^0}\left[1 + \left(\frac{p}{mc}\right)^2\left(\frac{17}{100} + \frac{21\int\limits_0^\infty (\partial\epsilon_\nu/\partial\nu)^2 d\nu}{50\int\limits_0^\infty \epsilon_\nu^2 \nu^{-2} d\nu}\right)\right]\right\},$$
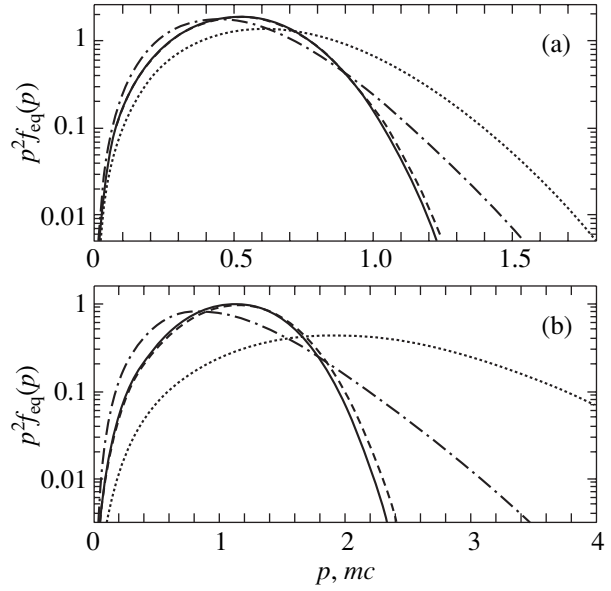
where T_{eq}^0 is given by Eq. (16).

Fig. 5. (a) The equilibrium distribution of electrons in an isotropic field of self-absorbed synchrotron radiation with $T_b^{max} = 5 \times 10^{11}$ K. The solid line represents the exact result obtained from Eqs. (34), (30), and (31). The dotted line indicates the nonrelativistic Maxwellian distribution with $kT_{eq}^0 = 95$ keV found from Eq. (16). The dashed line (almost coincident with the solid line) represents the mildly relativistic approximation (36). The dash–dotted line indicates the relativistic Maxwellian distribution with $kT = kT_{eff} = 45$ keV found from Eq. (37). The mean electron energy for this distribution is the same as that for the equilibrium distribution.

(b) The same as (a), but $T_b^{max} = 5 \times 10^{12}$ K. In this case, $kT_{eq}^0 = 950$ keV and $kT_{eff} = 140$ keV.

For synchrotron radiation with self-absorption at low frequencies [see Eqs. (12) and (13)], the equilibrium distribution is

$$f_{eq}(p) = \text{const} \times \exp\left\{-\frac{p^2}{2mkT_{eq}^0}\left[1 + 0.69\left(\frac{p}{mc}\right)^2\right]\right\}. \qquad (36)$$

In Fig. 5, the equilibrium distributions are plotted for two values of $T_b^{max} = 5 \times 10^{11}$ K and 5×10^{12} K. The corresponding stationary temperatures, as follows from estimates based on the nonrelativistic Eq. (16), are $kT_{eq} = 95$ and 950 keV. The exact result was obtained by numerical calculation of Eq. (34) using Eqs. (30) and (31). Also shown in the figure are the nonrelativistic Maxwellian distribution at temperature T_{eq}^0 and the mildly relativistic approximation (36). We see that the right wing of the distribution is significantly suppressed compared to the nonrelativistic Maxwellian distribution. This is because the diffusion coefficient decreases and the breaking force increases with increasing p. Sur-
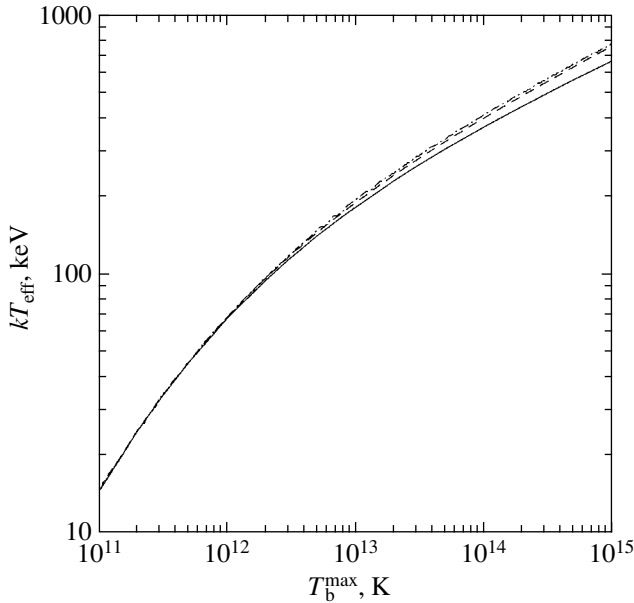
Fig. 6. Effective temperature of the stationary electron distribution defined by Eq. (37) versus peak brightness temperature. The solid line represents the exact result obtained from Eqs. (34), (30), and (31). The dashed line represents the result for the distribution described by the approximate formula (35). The dependence of the stationary temperature of Maxwellian electrons on $T_{\mathrm{b}}^{\max}$ is reproduced from Fig. 3 for comparison (dash–dotted line).

prisingly enough, the approximate formula (36) provides an excellent fit even when $kT_{\mathrm{eq}}^{0} > mc^2$.

Since the distribution (34) becomes Maxwellian in the limit $kT_{\mathrm{eq}}^{0} \ll mc^2$ and assumes a quasi-Maxwellian shape in the mildly relativistic regime, it seems natural to characterize this type of distribution by some effective temperature T_{eff}. We define T_{eff} as the temperature of the relativistic Maxwellian distribution for which the mean electron energy $\langle\gamma\rangle mc^2 = \langle(p^2 + 1)^{1/2}\rangle$ is equal to the corresponding value for the quasi-Maxwellian distribution:

$$\frac{\int (p^2 + 1)^{1/2} p^2 f_{\mathrm{eq}}(p)dp}{\int p^2 f_{\mathrm{eq}}(p)dp} = \langle\gamma\rangle(T_{\mathrm{eff}})mc^2, \qquad (37)$$

where the temperature dependence of $\langle\gamma\rangle$ is given by Eq. (18).

For the two examples given in Fig. 5, kT_{eff} takes on values of 45 and 140 keV; these should be compared with $kT_{\mathrm{eq}}^{0} = 95$ and 950 keV, respectively. The relativistic Maxwellian distributions that correspond to these T_{eff} are shown in Fig. 5.

In Fig. 6, T_{eff}, calculated using the exact formula (34) and its mildly relativistic approximation (35), is plotted against $T_{\mathrm{b}}^{\max}$. For comparison, the dependence

$T_{\mathrm{eq}}(T_{\mathrm{b}}^{\max})$ for Maxwellian electrons is reproduced from Fig. 3. We see that the two exact dependences essentially coincide (the difference is less than 10%) in an extremely wide range of parameters: $kT_{\mathrm{eff}}, kT_{\mathrm{eq}} \lesssim mc^2$. Even more surprising is the almost perfect agreement between the exact solution for $T_{\mathrm{eq}}(T_{\mathrm{b}}^{\max})$ and the mildly relativistic approximation (35) for $T_{\mathrm{eff}}(T_{\mathrm{b}}^{\max})$. It should be emphasized that the differences between the dependences shown in Fig. 6 are real (as confirmed by the fact that they diverge significantly when $T_{\mathrm{eff}} \gg mc^2$), although they are very small. This leads us to an important conclusion: the energy that can be accumulated by an ensemble of electrons through induced Compton heating (if inverse Compton scattering serves to cool down the electrons) in the mildly relativistic regime is virtually independent of whether or not the electrons are maintained Maxwellian while being heated.

We also checked that the contribution of the heated electrons to the gas pressure, which is proportional to $\langle p\beta\rangle \sim f(p^2 + 1)^{1/2}[1 - (1 + p^2)^{-1}]p^2 f(p)dp$ [compare with Eq. (37) for the mean energy], is virtually the same (to within 2% for any T_{eff}) for a quasi-Maxwellian plasma with the distribution function (34) and for a thermal plasma with $T = T_{\mathrm{eff}}$ (note that in the limit $kT_{\mathrm{eff}} \gg mc^2$ the two pressures must be equal, because $\beta \longrightarrow 1$). Thus, the effective temperature T_{eff} perfectly characterizes the thermodynamic properties of a mildly relativistic quasi-Maxwellian plasma heated through the induced Compton process.

It also follows from the above discussion that the simple expression (35) can be used to estimate the mean stationary electron energy with a high accuracy in a wide range of parameters, at least up to $T_{\mathrm{eff}} \sim mc^2$, which for our model spectrum corresponds to $T_{\mathrm{b}}^{\max} \sim 10^{15}$ K, irrespective of whether thermalization takes place or not.

Suppose that plasma with the electron distribution (35) does exist. Does it differ from thermal plasma observationally? In particular, will the energy spectrum of hard X-ray bremsstrahlung from such plasma be peculiar? We computed this spectrum for the momentum distribution shown in Fig. 5a ($kT_{\mathrm{eff}} = 45$ keV). The result is presented in Fig. 7. The computation consisted in weighting the Bethe–Heitler formula (Jauch and Rohrlich, 1976) for the electron–ion bremsstrahlung cross section with the given momentum distribution (36). We see that the deviation from the spectrum generated by an ensemble of relativistic Maxwellian electrons with temperature T_{eff} is negligible. Only when $kT_{\mathrm{eff}} \gtrsim 100$ keV does the bremsstrahlung spectrum forming in a quasi-Maxwellian plasma become markedly different from the spectrum corresponding to a thermal plasma.
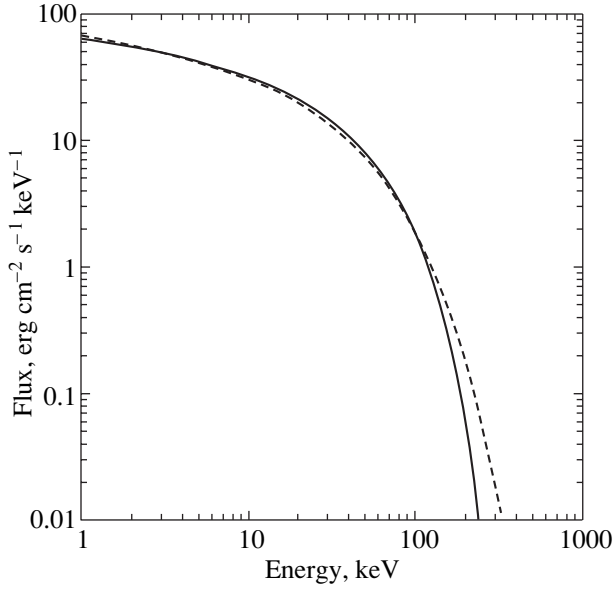
Fig. 7. The spectrum of hard X-ray bremsstrahlung from plasma whose electrons are distributed as shown in Fig. 5a (solid line) in comparison with the spectrum (dashed line) that corresponds to the relativistic Maxwellian distribution with $kT = kT_{\rm eff} = 45$ keV.

APPENDIX

In our recent paper (Sazonov and Sunyaev 2000), we gave an analytic expression for the kernel of the integral kinetic equation that describes the redistribution of photons in frequency through induced Compton scattering in a mildly relativistic thermal plasma. The terms responsible for the induced Compton process in Eq. (1), the generalized Kompaneets equation, can be derived in principle from this kernel. Unfortunately, the published expression contains an error (in the leading coefficient). As a result, the formula does not correspond to the stated accuracy (it is valid for $kT \lesssim 0.01mc^2$ instead of $kT \lesssim 0.1mc^2$). We use this opportunity to give the correct expression:

$$K^{\rm ind}(\nu, \mathbf{\Omega}; \nu', \mathbf{\Omega}') = \left(\frac{\nu'}{\nu}\right)^2 K(\nu', \mathbf{\Omega}' \longrightarrow \nu, \mathbf{\Omega})$$

$$- K(\nu, \mathbf{\Omega} \longrightarrow \nu', \mathbf{\Omega}') = \frac{3}{32\pi}\sqrt{\frac{2}{\pi}}\left(\frac{kT}{mc^2}\right)^{-3/2}$$

$$\times \frac{h\nu'(\nu' - \nu)}{mc^2 g\nu}\left[1 + \mu^2 + \left(\frac{1}{8} - \mu - \frac{63}{8}\mu^2 + 5\mu^3\right)\frac{kT}{mc^2}\right.$$

$$- \mu(1 - \mu^2)\left(\frac{\nu' - \nu}{g}\right)^2 - \frac{3(1 + \mu^2)mc^2}{8kT}$$

$$\times \left.\left(\frac{\nu' - \nu}{g}\right)^4\right]\exp\left[-\frac{(\nu' - \nu)^2 mc^2}{2g^2 kT}\right], \quad (38)$$

$$g = |\nu\mathbf{\Omega} - \nu'\mathbf{\Omega}'| = (\nu^2 - 2\nu\nu'\mu + \nu'^2)^{1/2}.$$

Here, ν and $\mathbf{\Omega}$ are the frequency and direction of propagation of a photon before the scattering, respectively; ν' and $\mathbf{\Omega}'$ are their values after the scattering; and $\mu = \mathbf{\Omega}\mathbf{\Omega}'$ is the cosine of the scattering angle.

An analogous correction should be made for the kernel averaged over the scattering angle (see Sazonov and Sunyaev 2000):

$$P^{\rm ind}(\nu, \nu') = \left(\frac{\nu'}{\nu}\right)^2 P(\nu' \longrightarrow \nu) - P(\nu \longrightarrow \nu')$$

$$= 2\sqrt{\frac{2}{\pi}}\left(\frac{kT}{mc^2}\right)^{-3/2}\frac{h\nu'(\nu' - \nu)}{mc^2\nu(\nu + \nu')}(p_0 + p_t),$$

$$p_0 = \left(\frac{11}{20} + \frac{4}{5}\delta^2 + \frac{2}{5}\delta^4\right)F + |\delta|\left(-\frac{3}{2} - 2\delta^2 - \frac{4}{5}\delta^4\right)G,$$

$$p_t = \left[\left(-\frac{1091}{1120} - \frac{507}{560}\delta^2 + \frac{57}{35}\delta^4 + \frac{68}{35}\delta^6\right)F\right.$$

$$\left. + |\delta|\left(\frac{9}{4} + \delta^2 - \frac{26}{5}\delta^4 - \frac{136}{35}\delta^6\right)G\right]\frac{kT}{mc^2}, \quad (39)$$

$$F = \exp(-\delta^2),$$

$$G = \int_{|\delta|}^{\infty}\exp(-t^2)dt = 0.5\pi^{1/2}Erfc(|\delta|),$$

$$\delta = \left(2\frac{kT}{mc^2}\right)^{-1/2}\frac{\nu' - \nu}{\nu' + \nu}.$$

Formulas (38) and (39) are applicable in the following ranges of parameters: $h\nu \ll kT \lesssim 0.1\ mc^2$, $nh\nu = kT_{\rm b} \gg kT$ (the latter condition means that the inverse Compton effect is small compared to the induced one).

REFERENCES

1. G. F. Bicknell, M. A. Dopita, and C. P. O. O'Dea, Astrophys. J. **485**, 112 (1997).
2. R. D. Blandford, Astron. Astrophys. **26**, 161 (1973).
3. R. D. Blandford and E. T. Scharlemann, Astrophys. Space Sci. **36**, 303 (1975).
4. A. Celotti, Z. Kuncic, M. J. Rees, and J. F. C. Wardle, Mon. Not. R. Astron. Soc. **293**, 288 (1998).
5. A. Challinor and A. Lasenby, Astrophys. J. **499**, 1 (1998).
6. R. J. Gould, Astron. Astrophys. **76**, 306 (1979).

7. A. F. Illarionov and D. A. Kompaneets, Zh. Éksp. Teor. Fiz. **71**, 1773 (1976) [Sov. Phys. JETP **44**, 930 (1976)].

8. N. Itoh, Y. Kohyama, and S. Nozawa, Astrophys. J. **502**, 7 (1998).

9. J. M. Jauch and F. Rohrlich, *The Theory of Photons and Electrons* (Springer-Verlag, New York, 1976, 2nd ed.).

10. A. S. Kompaneets, Zh. Éksp. Teor. Fiz. **31**, 876 (1956) [Sov. Phys. JETP **4**, 730 (1957)].

11. N. A. Krall and A. W. Trivelpiece, *Principles of Plasma Physics* (McGraw-Hill, New York, 1973; Mir, Moscow, 1975).

12. Z. Kuncic, G. V. Bicknell, and M. A. Dopita, Astrophys. J. Lett. **495**, L35 (1998).

13. L. D. Landau and E. M. Lifshitz, *The Classical Theory of Fields* (Nauka, Moscow, 1988; Pergamon, Oxford, 1975).

14. E. V. Levich and R. A. Sunyaev, Astron. Zh. **48**, 461 (1971) [Sov. Astron. **15**, 363 (1971)].

15. J. Peyraud, J. Phys. (Paris) **29**, 88 (1968).

16. L. A. Pozdnyakov, I. M. Sobol, and R. A. Sunyaev, Astrophys. Space Phys. Rev. **2**, 189 (1983).

17. S. Y. Sazonov and R. A. Sunyaev, Astrophys. J. **543**, 28 (2000).

18. A. I. Shestakov, D. S. Kershaw, and M. K. Prasad, J. Quant. Spectrosc. Radiat. Transf. **40**, 577 (1988).

19. M. W. Sincell and J. H. Krolik, Astrophys. J. **430**, 550 (1994).

20. L. Spitzer, *Physical Processes in the Interstellar Medium* (Wiley, New York, 1978; Mir, Moscow, 1981).

21. R. A. Sunyaev, Astron. Zh. **48**, 244 (1971) [Sov. Astron. **15**, 190 (1971)].

22. R. Vermeulen, in *Proceedings of the Astrophysical Jets Meeting, Baltimore, 1992,* Ed. by D. Burgarella, M. Livio, and Ch. O'Dea (Cambridge Univ. Press, Cambridge, 1992), p. 241.

23. A. V. Vinogradov and V. V. Pustovalov, Zh. Éksp. Teor. Fiz. **62**, 1702 (1972) [Sov. Phys. JETP **35**, 886 (1972)].

24. P. Woodward, Phys. Rev. D **1**, 2731 (1970).

25. Ya. B. Zel'dovich, Usp. Fiz. Nauk **115**, 162 (1975) [Sov. Phys. Usp. **18**, 79 (1975)].

26. Ya. B. Zel'dovich and E. V. Levich, Pis'ma Zh. Éksp. Teor. Fiz. **11**, 57 (1970) [JETP Lett. **11**, 35 (1970)].

Translated by S. Sazonov

Small-Scale Anisotropy of Cosmic Rays with Energies above 3×10^{18} eV Based on Data from the Yakutsk EAS Facility

A. V. Glushkov* and M. I. Pravdin

Institute of Cosmophysical Research and Aeronomy, Siberian Division, Russian Academy of Sciences,
pr. Lenina 31, Yakutsk, 677007 Russia

Abstract—We analyze the directions of the arrival of cosmic rays with energies $E_0 \geq 3 \times 10^{18}$ eV and zenith angles $\theta \leq 45°$ recorded by the Yakutsk extensive air shower (EAS) facility during 1974–2000. They are shown to have a small-scale structure with scale sizes of 5°–10°. Enhanced particle fluxes compared to the expected levels for random distributions at (4–5)σ are observed from the Galactic and Supergalactic planes. © 2001 MAIK "Nauka/Interperiodica".

INTRODUCTION

Of great importance in understanding the processes that take place in the Galaxy and in the Universe as a whole is the primary cosmic radiation (PCR) of extremely high energies ($E_0 > 10^{18}$ eV). It is recorded by extensive air shower (EAS) facilities. The PCR of these energies is generally believed to consist mostly of charged particles: protons and the nuclei of various chemical elements. They are strongly mixed by the Galactic magnetic field, and the PCR has an almost isotropic sky distribution. Under these conditions, local PCR sources are difficult to detect.

At the energies of giant EAS ($E_0 \geq 10^{19}$ eV), the PCR arrival directions correlate with the Galactic plane (see, e.g., Szabelsky *et al.* 1986; Afanasiev *et al.* 1995) and with the Supergalactic plane (Stanev *et al.* 1995; Ivanov *et al.* 1997; Glushkov and Sleptsov 2001). Mikhaĭlov (1999) and the AGASA group (Takeda *et al.* 1999) reported the detection of separate clusters in the directions of arrival of such particles. Mikhaĭlov (1999) pointed out that some clusters correlate with pulsars located at the entrance to the Local Arm of the Galaxy, while the AGASA group (Takeda *et al.* 1999) pointed to a correlation with the Supergalactic plane. There is also evidence (Glushkov 1988; Uryson 1999) that the sources of the primary particles of giant EASs can be galaxies with active nuclei.

Recently, the AGASA group (Hayashida *et al.* 1999) detected an enhanced PCR flux at $E_0 \approx (8\text{–}20) \times 10^{17}$ eV from a region near the Galactic center. This result was confirmed and refined by the Australian SUGAR group (Bellido *et al.* 2000). Unfortunately, the Yakutsk facility cannot "see" the Galactic center. Here, we provide experimental data that have shed more light on the origin of the ultrahigh-energy cosmic rays.

THE PARAMETERS STUDIED AND DISCUSSION

Below, we consider EASs with energies $E_0 \geq 3 \times 10^{18}$ eV and zenith angles $\theta \leq 45°$ recorded by the Yakutsk facility during 1974–2000. We analyzed the small-scale anisotropy, i.e., local PCR inhomogeneities on a scale of ~10°. Our analysis included EASs whose arrival directions were determined at about five stations and the axes were within the facility's central circle with a radius of ≤1700 m (i.e., they were never outside the facility's perimeter). These events give minimum errors in basic EAS parameters (the axis direction and coordinates, E_0, etc.). The energy of the primary particles E_0 was calculated from the relations

$$E_0 = (4.8 \pm 1.6) \times 10^{17} (\rho_{s,600}(0°))^{1.0 \pm 0.02} \text{ [eV]}, \quad (1)$$

$$\begin{aligned} \rho_{s,600}(0°) \\ = \rho_{s,600}(\theta) \exp((\sec\theta - 1)1020/\lambda_\rho) \text{ [m}^{-2}], \end{aligned} \quad (2)$$

$$\lambda_\rho = (450 \pm 44) + (32 \pm 15)\log(\rho_{s,600}(0°)) \text{ [g/cm}^2], \quad (3)$$

where $\rho_{s,600}(\theta)$ is the charged-particle density measured by ground-based scintillation detectors at the distance $R = 600$ m from the shower axis.

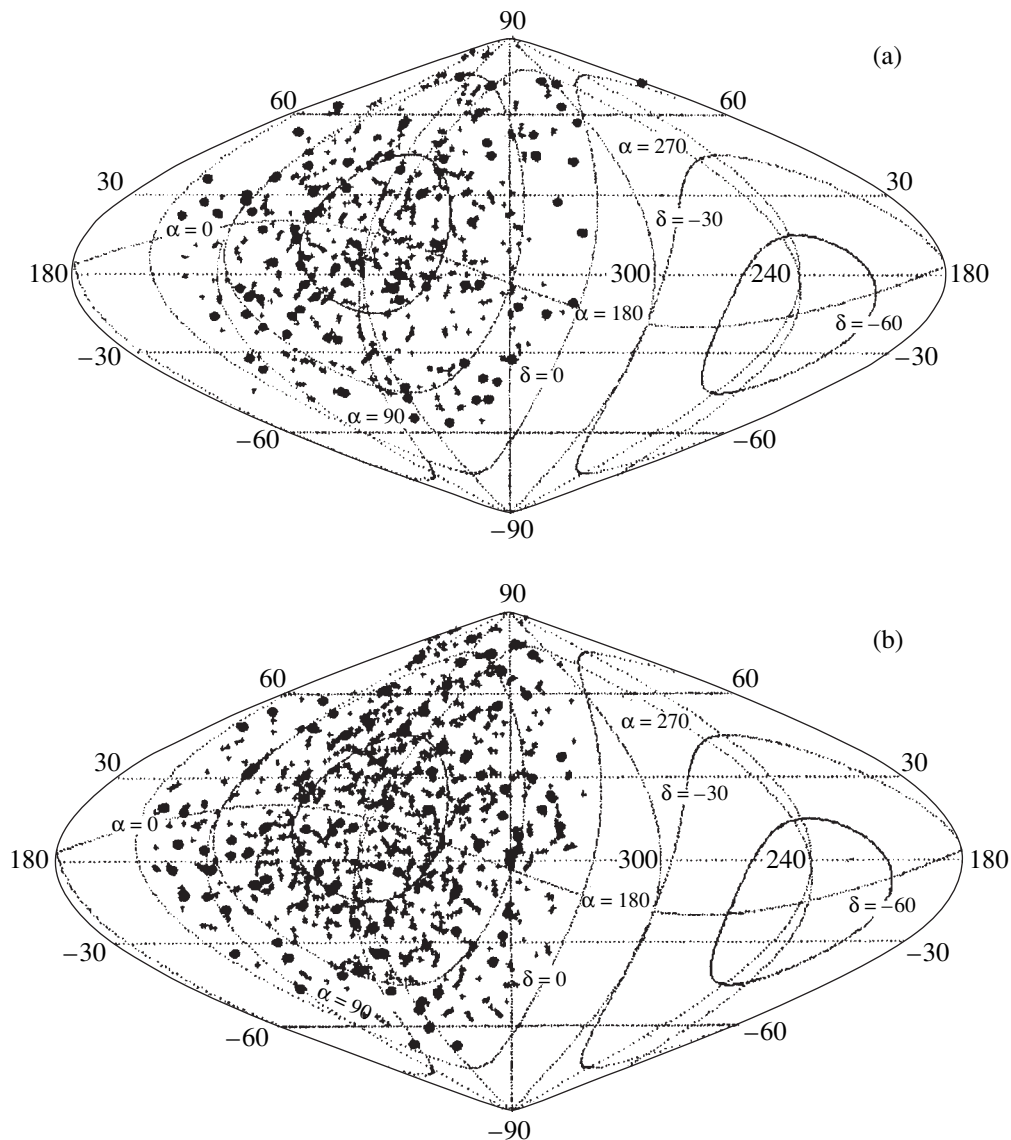* E-mail address for contacts: a.v.glushkov@ikfia.ysn.ru

Fig. 1. The centers of nodes with ≥ 2 showers within circles of radius $\leq 3°$ on the celestial sphere in Supergalactic coordinates inferred from the Yakutsk data: (a) $E_0 > 5 \times 10^{18}$ eV and (b) $E_0 = (3–5) \times 10^{18}$ eV. The circles represent clusters with a $\geq 3\sigma$ excess of events above the mean shower density for a given declination in right ascension (in equatorial coordinates).

Two samples with $E_0 = (3–5) \times 10^{18}$ eV (2033 showers) and $E_0 > 5 \times 10^{18}$ eV (1267 showers) were considered. We found all the neighbors within an angular distance $d \leq 3°$ from the arrival direction of each shower. If there were ≥ 2 showers within this circle, then their coordinates were averaged and subsequently used as new points (we call them nodes) in the search of clusters. In this procedure, any isolated (located at a distance $>d$) group of showers transforms to a single node. It can be treated as a point cluster. Series of closely related nodes (often also isolated spatially) form smeared clusters.

Figure 1 shows two maps of nodes on the developed celestial sphere (in Supergalactic coordinates) for the above EAS energies. The Supergalatic North Pole has

Galactic coordinates $b_G = 6.32°$ and $l_G = 47.37°$ (Hewitt and Burbidge 1987), and we measured its longitude from the direction of the Supergalactic center. For convenience, the equatorial coordinates are also shown on these maps. The nodes concentrate closer to the center of the figure, where the Earth's North Pole is located. Because of the geographical position of the Yakutsk facility (61.7° N), this region of the sky has the longest exposure. The filled circles represent nodes in which the excess of events above the mean shower density in right ascension (in equatorial coordinates) for a given declination is $\geq 3\sigma$. These nodes can be considered as the clusters that may primarily point to the positions of probable pointlike PCR sources.
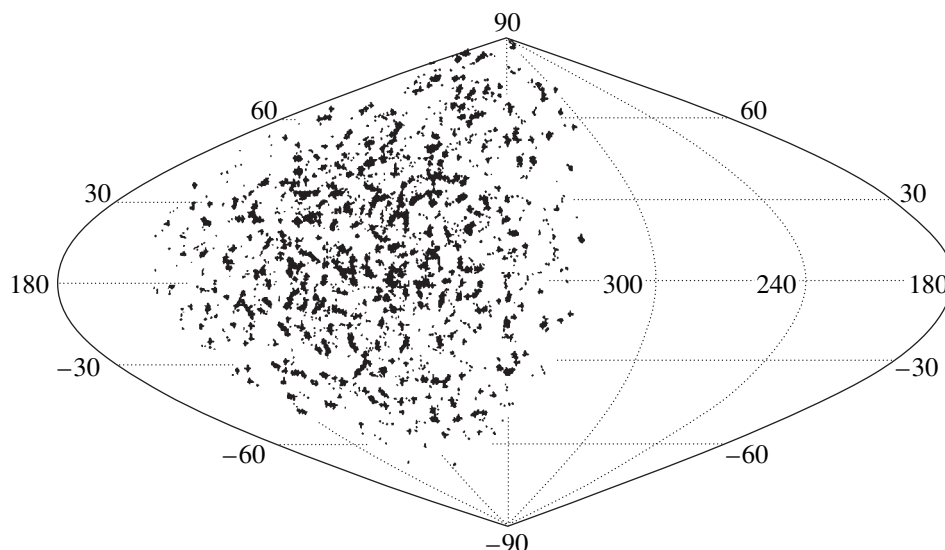
Fig. 2. The superimposed maps of Fig. 1 in Supergalactic coordinates: the pluses are for $E_0 > 5 \times 10^{18}$ eV and the dots are for $E_0 = (3–5) \times 10^{18}$ eV.

Let us consider the data of Fig. 1 in more detail. The showers with $E_0 > 5 \times 10^{18}$ eV (a) and $E_0 = (3–5) \times 10^{18}$ eV (b) form, respectively, 1071 and 1884 nodes with ≥ 2 events. They overlap with each other much more frequently than they do for a random isotropic distribution of PCR arrival directions. At distances $d \leq 1°$, 306 nodes of our samples (a) and (b) actually coincided, while Monte Carlo simulations yielded 261. The difference is $(306 − 261)/\sqrt{261} \approx 2.8\sigma$. It corresponds to the probability of a chance outcome $P \approx 8 \times 10^{-3}$.

Figure 1 draws attention to the fact that the locations of the clusters (filled circles) in these samples quite often overlap with each other or with individual nodes. In addition, the nodes often form close ($d \leq 3°–5°$) groups, which may suggest the existence of clusters with blurred images because of the errors in the EAS arrival directions or for other reasons. The nodes tend to be arranged in chains. When both maps are superimposed, the nodes frequently coincide (within 1°) or complement each other to form new chains. This is clearly seen in Fig. 2, where an ordered spatial structure of nodes also shows up more clearly.

The pattern of data distribution in Fig. 2 does not rule out the possible presence of a certain cellular structure in the PCR arrival directions. The distribution of individual minimum angular distances d_{min} (to the nearest neighbor) for each of the 583 showers with $E_0 \geq 10^{19}$ eV and $\theta \leq 60°$ (Fig. 3) gives grounds for this assumption. These events are recorded by the largest number of stations, and they can primarily point to the PCR sources. The experimental data and the expected distributions are indicated by filled and open circles, respectively. The latter was found by calculating random showers with an isotropic distribution by taking into account the peculiarities of the exposure of the sky region above the

Yakutsk facility. Both distributions were obtained as the sum of four independent (146 showers in each) distributions. This was done to reveal more clearly the structural features present in the experimental data.

We see from Fig. 3 that statistically significant peaks are observed in the intervals 5°–6° and 9°–10°. A comparison of the measured and expected distributions gives $\chi^2 = 52.8$ for $n = 25$ degrees of freedom. The probability of a chance outcome P is $\approx 10^{-3}$. Our analysis shows that the above peaks resulted neither from the shower selection procedure nor from the experimental errors, but are attributable to the tendency for the PCR to arrive from certain regions of the sky. They have an ordered structure with a typical angular size of $\approx 5°$.

Let us compare the data from different world facilities. In Fig. 4, the dots indicate (in Supergalactic coordinates) 67 clusters of two events, and the filled circles indicate 51 clusters of three or more events with angular distances $d \leq 3°$ from 583 showers with $E_0 \geq 10^{19}$ eV and $\theta \leq 60°$, as observed with the Yakutsk facility. As was noted above, their denser distribution toward the center is essentially attributable to the nonuniform exposure of the sky region surveyed. The closed curve indicates the motion of the zenith of the Yakutsk facility. The crosses represent individual showers with $E_0 \geq 4 \times 10^{19}$ eV from the Volcano Ranch (Linsley 1980), Haverah Park (Cunningham *et al.* 1980), SUGAR (Winn *et al.* 1986), and AGASA (Takeda *et al.* 1999) catalogs. The clusters found by Takeda *et al.* (1999) are indicated by open circles and designated as C1–C5. They consist of four doublets, while cluster C2 consists of a triplet.

Recently, Tinyakov and Tkachov (2001) analyzed the data of Takeda *et al.* (1999) together with the catalog (242 giant showers of the Yakutsk facility) of Efi-
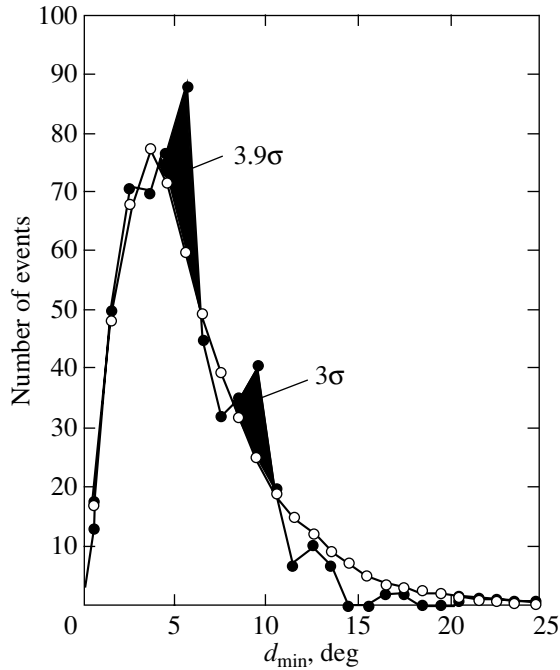
Fig. 3. The distributions of minimum angular distances for 583 showers with $E_0 \geq 10^{19}$ eV and $\theta \leq 60°$ constructed from the Yakutsk data: the filled and open circles represent the experimental distribution and the expected distribution for an isotropic flux, respectively.

mov *et al.* (1988) to check the significance of the above clusters. In their analysis, these authors used a two-dimensional angular correlation function. They confirmed the tendency for PCR with the energies considered to form isolated clusters. In particular, in the Yakutsk data, the most significant results were obtained for $d \approx 4°$. This is consistent with the peak in Fig. 3 at

$d \approx 5°$, although the data in Fig. 3 point to voids in the PCR arrival directions rather than to the presence of clusters.

We see from Fig. 4 that the clusters found at the Yakutsk facility and the showers of the above energies recorded by other world facilities quite often overlap each other or are located nearby and complement each other. An isolated group with cluster C1 stands out from them. Here, just as in Fig. 2, we see chains. Because of the small number of events, they are less pronounced.

The data in Figs. 2 and 4 have an appearance similar to the cellular distribution of galaxies in the Universe (see, e.g., Novikov 1968). There is an opinion that ultrahigh-energy cosmic rays can leave the Galaxy. A similar phenomenon appears to take place in other galaxies. If this is the case, then it may well be that the observed small-scale PCR anisotropy reflects the cellular distribution of galaxies in the Universe.

Let us assume that the nodes in Fig. 1 are related to local PCR sources. Consider the correlations of these nodes with the Galactic and Supergalactic planes. In Fig. 5, deviations $n_\sigma = (N_{exp} - N_{ran})/\sigma$ of the observed number of nodes (N_{exp}) with ≥ 7 events from their expected number (N_{ran}) (in units of standard $\sigma = \sqrt{N_{ran}}$) from the samples of Fig. 1 in Galactic (G) and Supergalactic (SG) coordinates is plotted versus latitude (at $\Delta b = 5°$ steps). The values of N_{ran} were determined from Monte Carlo simulations of isotropic PCR. This was done for each shower by replacing the measured arrival time (UT) and azimuth (in the facility's horizontal coordinate system) with random values.

In Galactic coordinates in Fig. 5a (G), we clearly see the north–south asymmetry in the arrival directions of EASs with $E_0 > 5 \times 10^{18}$ eV (with an excess from south
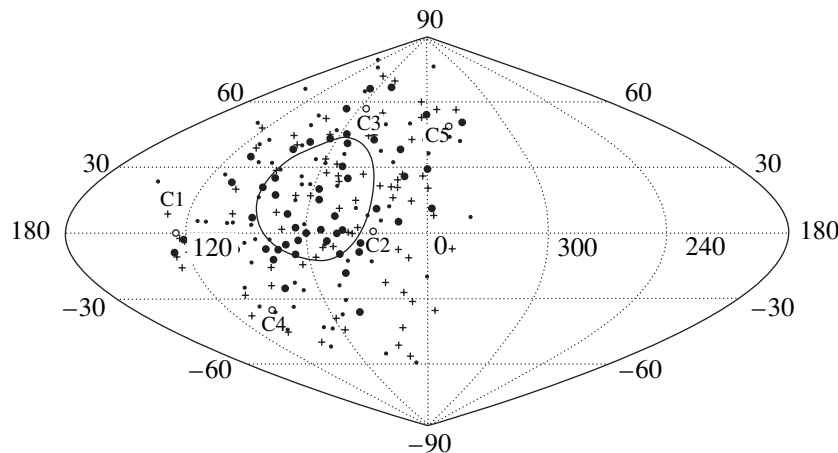
Fig. 4. The distribution of clusters with angular distances $\leq 3°$ for 583 showers with $E_0 \geq 10^{19}$ eV and $\theta \leq 60°$ constructed from the Yakutsk data: the dots mark clusters of two showers; the filled circles mark clusters of ≥ 3 showers; the closed curve represents the motion of the zenith of the Yakutsk facility; the open circles mark clusters (C1–C5) of Takeda *et al.* (1999); and the pluses mark individual showers with $E_0 \geq 4 \times 10^{19}$ eV from Volcano Ranch (Linsley 1980), Haverah Park (Cunningham *et al.* 1980), SURAR (Winn *et al.* 1986), and AGASA (Takeda *et al.* 1999) catalogs.

Fig. 5. The distributions of deviations $n_\sigma = (N_{exp} - N_{ran})/\sqrt{N_{ran}}$ of the observed number of nodes in Fig. 1 (N_{exp}) from the expected number of nodes (N_{ran}) with ≥ 7 showers in samples with (a) $E_0 > 5 \times 10^{18}$ eV and (b) $E_0 = (3–5) \times 10^{18}$ eV in the latitude of shower arrival in Galactic (G) and Supergalactic (SG) coordinates.
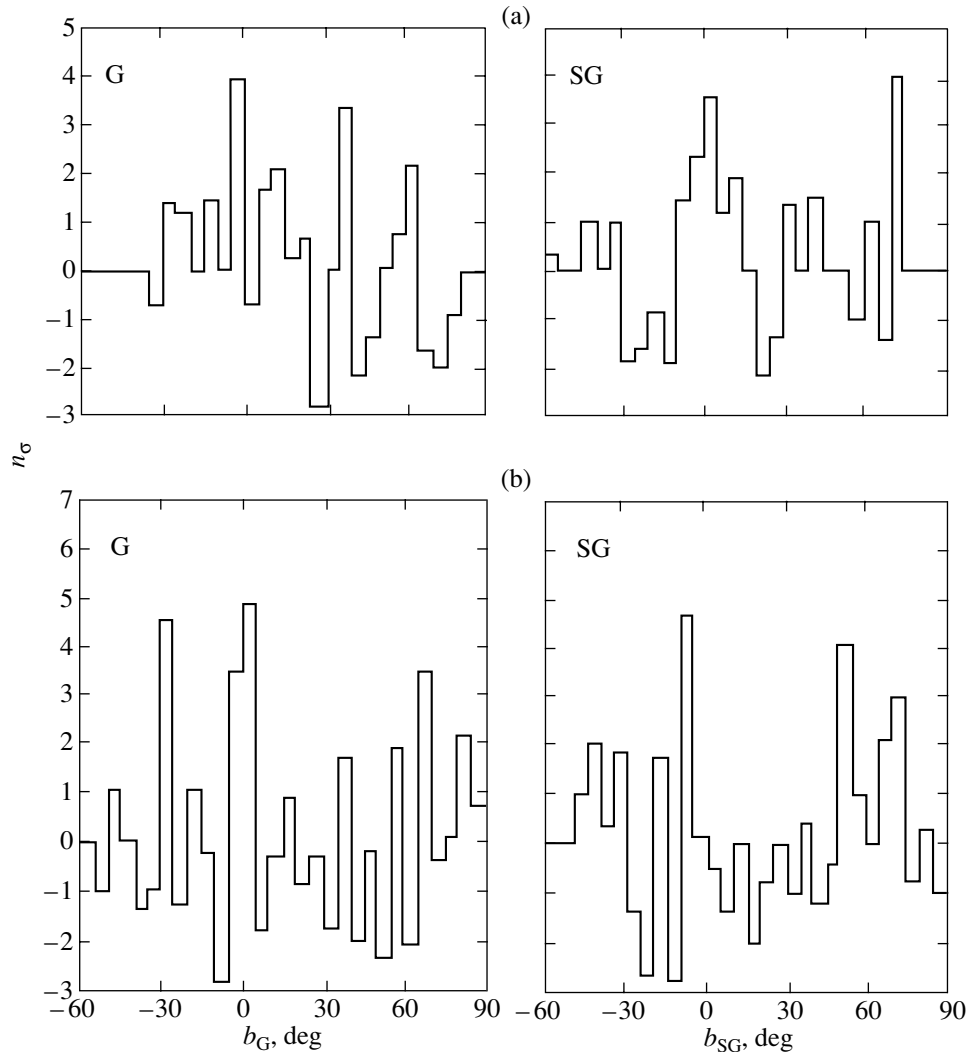
latitudes) found previously by Afanasiev *et al.* (1995) at the Yakutsk facility. The mean latitudes of the measured and calculated distributions are $\langle b_{exp} \rangle = 17.7 \pm 2.4$ and $\langle b_{ran} \rangle = 25.1$, respectively. There is a significant (4σ) excess of events near the Galactic plane ($b_G = -5°$ to $0°$). Statistically significant peaks are also observed at latitudes $b_G \approx 35°$ and $65°$.

By contrast, Fig. 5a (SG) exhibits no asymmetry with respect to the Supergalactic plane ($\langle b_{exp} \rangle = 12.8 \pm 2.4$ and $\langle b_{ran} \rangle = 12.0$). On the other hand, there is a large peak near it ($b_{SG} = -10°$ to $20°$). If its area is compared with the area of the peak near the Galactic plane mentioned above, they differ by a factor of ~6. This can be interpreted as an indication that the sources of PCR with $E_0 > 5 \times 10^{18}$ eV are located mostly outside the Galaxy.

At $E_0 = (3–5) \times 10^{18}$ eV, the role of the Galaxy in PCR generation increases. This is suggested by the excess of events in Fig. 5b (G) in the region of its disk ($b_G = -5°$ to $5°$), which increased appreciably compared to Fig. 5a (G). At the same time, the above north–south asymmetry vanished ($\langle b_{exp} \rangle = 23.2 \pm 1.5$ and $\langle b_{ran} \rangle = 24.2$). The role of the Supergalaxy in this energy range appears to decrease appreciably, although it cannot yet be completely ruled out. Near the Supergalactic plane ($b_{SG} = -10°$ to $-5°$) in Fig. 5b (SG), a smaller, but statistically significant excess of events is preserved.

The appreciable correlations of PCR arrival directions with the Galactic and Supergalactic plane were found because of the huge statistics of showers recorded by the Yakutsk facility (about 37 000 at $E_0 \geq 10^{18}$ eV) and their rigid selection for the analysis. As yet no analogous results have been obtained with the
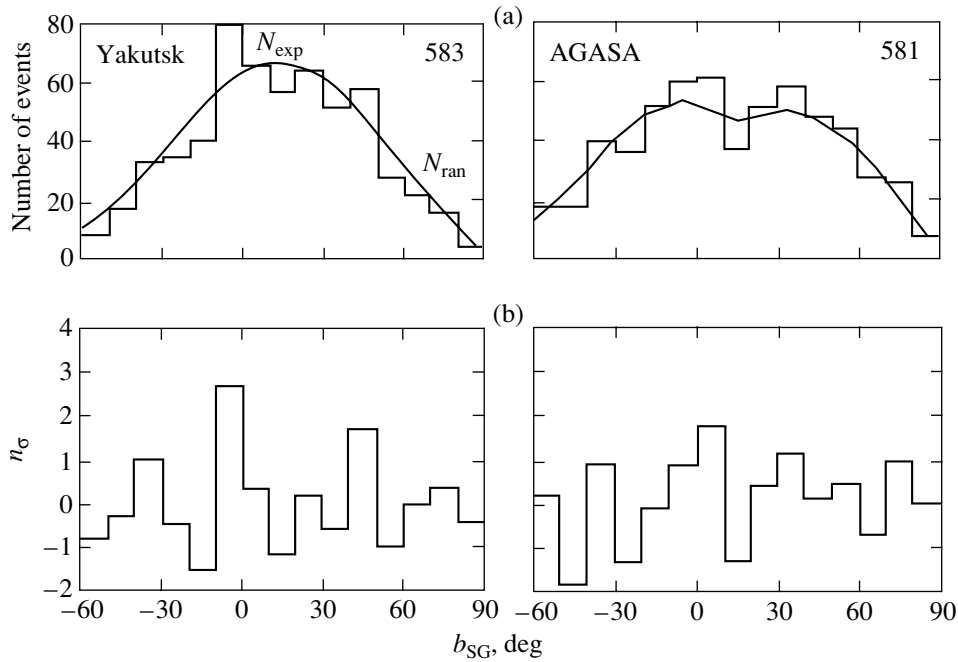
Fig. 6. (a) The distributions of showers with $E_0 \geq 10^{19}$ eV in the latitude of their arrival in Supergalactic coordinates, as constructed from the Yakutsk and AGASA data (Takeda *et al.* 1999); the numbers are the number of showers. (b) Deviations $n_\sigma = (N_{exp} - N_{ran})/\sqrt{N_{ran}}$.

AGASA facility, which is similar to our facility in detector type and in shower processing technique. Takeda *et al.* (1999) note that two clusters were found near the Supergalactic plane at $E_0 \geq 4 \times 10^{19}$ eV (see Fig. 4).

At first glance, the Yakutsk and AGASA results give different answers to the question of the possible role of the Supergalaxy in the origin of ultrahigh-energy cosmic rays. However, there is no contradiction here. This follows from Fig. 6, which shows the distribution of arrival directions of showers with $E_0 \geq 10^{19}$ eV in latitude (at $\Delta b_{SG} = 10°$ steps) in Supergalactic coordinates, as constructed from the data of both facilities. We obtained the AGASA distribution as the sum of three distributions from Takeda *et al.* (1999). Figure 6b shows deviations of the number of measured events from that expected for isotropic fluxes (similar to Fig. 5). The number of events considered is the same. In our case, we took showers with $\theta \leq 60°$ recorded by the entire area (even with the axes outside the facility perimeter).

We see that although the initial distributions in Fig. 6a are different, the distributions in Fig. 6b are similar. Note some important details. First, both distributions in Fig. 6b exhibit excesses of the recorded events above the expected ones by $(1.8–2.1)\sigma$ in the latitude band $|b_{SG}| \leq 10°$. Second, there are dips by $\approx -1.5\sigma$ at $|b_{SG}| \approx 10°–20°$, which are symmetric about the Supergalactic plane. The peaks of excess radiation from the Supergalactic plane become more significant against the background of these dips. Other features of the distributions

in Fig. 6b also coincide to some extent, suggesting that they are not random in nature.

A comparison of our data in Figs. 5 and 6 shows that there is no point in taking the step $\Delta b_{SG} = 10°$, because this causes the significance of the results to be underestimated. The actual accuracy of the experiment, especially for a rigid selection of events for the analysis, is not lower than $1°–2°$.

The correlation of the arrival directions of PCR with $E_0 > 5 \times 10^{18}$ eV with the Supergalactic disk suggests that this radiation is mainly extragalactic and, apparently, electrically neutral. Otherwise, primary particles with electric charge z must have moved in a magnetic field, depending on their energy E_0, along trajectories with the radius of curvature

$$R = E_0/300Hz. \qquad (4)$$

Even protons with energies $\sim 10^{19}$ eV would have in the Galactic magnetic field ($H \sim 3 \times 10^{-6}$ G) a radius of curvature of ~ 3 kpc, i.e., considerably smaller than the radius of the Galaxy disk (≈ 15 kpc). The intergalactic magnetic fields, although they are weak ($H \sim 9 \times 10^{-10}$ G), also give for protons with the above energies $R \sim 10$ Mpc, which is much smaller than the diameter of the Supergalaxy (≈ 60 Mpc). Under these conditions, charged particles would forget the places of their formation. They would lose the small-scale cellular structure and, most likely, the correlation of their directions with the Supergalactic plane, which is not observed.

According to Hayashida *et al.* (1999), the PCR at $E_0 \approx (8–20) \times 10^{17}$ eV is Galactic in nature and may consist mostly of neutrons. Since excess particle fluxes from the regions of the Galactic and Supergalactic disks are seen in Fig. 5b, we have to admit the possible existence of mixed PCR (Galactic and extragalactic) in the energy range $E_0 \approx (2–5) \times 10^{18}$ eV. The extragalactic radiation can hardly consist of neutrons. At $E_0 \sim 10^{19}$ eV, neutrons have a Lorentz factor of ~10^{10} and are able to traverse a distance of ~100 kpc, i.e., much smaller than the size of the Supergalaxy, before their decay.

Most likely, these must be some other stable neutral particles. First of all, these are gamma-ray photons, which can produce ultrahigh-energy air showers. Recently, Anchordoqui *et al.* (2000) have shown that neutrinos, under certain conditions for increase in the cross section of their interaction with nucleons (σ_{Nv}), can produce EASs at extremely high energies. The possibility of detecting new (exotic) particles in PCR cannot be ruled out. So far, it is difficult to be more specific on this subject. Further comprehensive (astrophysical and nuclear-physical) studies of this issue are required.

In addition to the above results, there is currently other evidence that the PCR composition must change at $E_0 \geq (3–5) \times 10^{18}$ eV. We also drew this conclusion from a comprehensive analysis of the spatial–temporal structure of EAS electrons and muons by using the Yakutsk data (Glushkov *et al.* 1998, 2000a, 2000b). In these papers, we showed that at $E_0 \leq (1–3) \times 10^{18}$ eV, the experimental data are consistent with the calculations of Kalmikov *et al.* (1995) based on the QGSJET model; it was assumed that the composition of the primary particles changed from a mixture enriched at $E_0 \sim 10^{17}$ eV with heavy nuclei ($z = 10–30$ account for $\approx 63 \pm 7\%$), according to Vishnevskaya *et al.* (1999), to a lighter mixture with the dominance of protons (or neutrons, in the opinion of Hayashida *et al.* 1999) at $E_0 \sim 10^{18}$ eV. At energies $E_0 \geq (3–5) \times 10^{18}$ eV, the showers develop differently. They significantly change their transverse structure. These changes cannot be explained in terms of the QGSJET model (for any PCR composition, from protons to iron nuclei) and require different ideas of the PCR composition and the EAS development at extremely high energies.

CONCLUSION

We see from the above data that cosmic rays with $E_0 \geq 3 \times 10^{18}$ eV tend to form multiple clusters, which are ordered somehow. It may well be that they reflect the small-scale (probably cellular) distribution of galaxies in the Universe. The arrival directions of cosmic rays with $E_0 \approx (3–5) \times 10^{18}$ eV correlate with the Galactic and Supergalactic planes, suggesting that the particles with such energies can be both Galactic and extragalactic in origin. At energies $E_0 > 5 \times 10^{18}$ eV, there is evidence that they are mostly extragalactic in origin.

The above facts and the results of Glushkov *et al.* (1998, 2000a, 2000b) argue for the hypothesis of the possible existence of ultrahigh-energy extragalactic neutral particles in the primary radiation. On their way to the Earth, they probe not only the large-scale structure of the Universe, but, probably, also its small-scale structure, spanning a volume much larger than the sizes of the Supergalaxy.

ACKNOWLEDGMENTS

REFERENCES

1. L. Anchordoqui, H. Coldberg, T. McCauley, *et al.*, arXiv:hep-ph/0011097 (2000).
2. B. N. Afanasiev, M. N. Dyakonov, T. A. Egorov, *et al.*, in *Proceedings of the 24th International Cosmic Ray Conference*, 1995, Vol. 2, p. 756.
3. J. A. Bellido, B. W. Clay, R. B. Dawson, and M. Johnston-Hollitt, astro-ph/0009039 (2000).
4. G. Cunningham, D. M. Edge, D. England, *et al.*, in *Catalogue of Highest Energy Cosmic Rays* (World Data Center C2 for Cosmic Rays Institute of Physical and Chemical Research, Tokyo, 1980), No. 1.
5. N. N. Efimov, T. A. Egorov, D. D. Krasilnikov, *et al.*, in *Catalogue of Highest Energy Cosmic Rays* (World Data Center C2 for Cosmic Rays Institute of Physical and Chemical Research, Tokyo, 1988), No. 3.
6. A. V. Glushkov, Pis'ma Zh. Éksp. Teor. Fiz. **48**, 513 (1988) [JETP Lett. **48**, 555 (1988)].
7. A. V. Glushkov and I. E. Sleptsov, Izv. Akad. Nauk, Ser. Fiz. **65**, 437 (2001).
8. A. V. Glushkov, V. B. Kosarev, I. T. Makarov, *et al.*, Pis'ma Zh. Éksp. Teor. Fiz. **67**, 361 (1998) [JETP Lett. **67**, 383 (1998)].
9. A. V. Glushkov, I. T. Makarov, M. I. Pravdin, *et al.*, Pis'ma Zh. Éksp. Teor. Fiz. **71**, 145 (2000a) [JETP Lett. **71**, 97 (2000a)].
10. A. V. Glushkov, M. I. Pravdin, I. E. Sleptsov, *et al.*, Yad. Fiz. **63**, 1557 (2000b) [Phys. At. Nucl. **63**, 1477 (2000b)].
11. N. Hayashida, M. Nagano, D. Nishikawa, *et al.*, Astropart. Phys. **10**, 303 (1999).
12. A. Hewitt and G. Burbidge, Astrophys. J., Suppl. Ser. **63**, 1 (1987).
13. A. A. Ivanov, A. D. Krasil'nikov, S. I. Nikl'skiĭ, and M. I. Pravdin, Izv. Akad. Nauk, Ser. Fiz. **61**, 520 (1997).
14. N. N. Kalmikov, G. B. Khristiansen, S. S. Ostapchenko, *et al.*, in *Proceedings of the 24th International Cosmic Ray Conference,* 1995, Vol. 1, p. 123.
15. J. Linsley, in *Catalogue of Highest Energy Cosmic Rays* (World Data Center C2 for Cosmic Rays Institute of Physical and Chemical Research, Tokyo, 1980), No. 1.
16. A. A. Mikhaĭlov, Izv. Akad. Nauk, Ser. Fiz. **63**, 557 (1999).

17. I. D. Novikov, *How Universe Was Exploded* (Nauka, Moscow, 1988).

18. T. Stanev, P. L. Biermann, J. Lloyd-Evans, *et al.*, Phys. Rev. Lett. **75**, 3056 (1995).

19. J. Szabelsky, J. Wdowczyk, and A. W. Wolfendale, J. Phys. G **12**, 1433 (1986).

20. M. Takeda, N. Havashida, K. Honda, *et al.*, Astrophys. J. **522**, 225 (1999).

21. P. G. Tinyakov and I. I. Tkachov, astro-ph/0102101 (2001).

22. A. V. Uryson, Zh. Éksp. Teor. Fiz. **116**, 1121 (1999) [JETP **89**, 597 (1999)].

23. E. A. Vishnevskaya, N. N. Kalmykov, G. V. Kulikov, *et al.*, Yad. Fiz. **62**, 300 (1999) [Phys. At. Nucl. **62**, 265 (1999)].

24. M. M. Winn, J. Ulrichs, L. S. Peak, *et al.*, in *Catalogue of Highest Energy Cosmic Rays* (World Data Center C2 for Cosmic Rays Institute of Physical and Chemical Research, Tokyo, 1986), No. 2.

Translated by G. Rudnitskiĭ

X-ray Bursts from the Source A1742–294 in the Galactic-Center Region

A. A. Lutovinov[1]*, S. A. Grebenev[1], M. N. Pavlinsky[1], and R. A. Sunyaev[1, 2]

[1] *Space Research Institute, Russian Academy of Sciences, Profsoyuznaya ul. 84/32, Moscow, 117810 Russia*
[2] *Max-Plank-Institute für Astrophysik, Karl Schwarzschild Strasse 1, 86740 Garching bei München, Germany*
Received March 3, 2001

Abstract—We present observations of the X-ray burster A1742–294 near the Galactic center with the ART-P telescope onboard the Granat observatory. The shape of its persistent spectra was described well by the model of bremsstrahlung from optically thin plasma, and it remained essentially unchanged over ~2.5 years of observations. We show that the mean interval between X-ray bursts from the source is several times shorter than assumed previously and that the burst profile itself depends on the flux during the burst. We analyze in detail the strong X-ray burst detected from this source on October 18, 1990, and construct the evolution curves of its luminosity and radiation temperature. © 2001 MAIK "Nauka/Interperiodica".

INTRODUCTION

Because of the high concentration of sources of different nature, the Galactic-center region is one of the most interesting and most commonly observed regions in X-rays. Although the first sources in this region were discovered back in the 1970s (Lewin *et al.* 1976; Proctor *et al.* 1978), its detailed map was first obtained by the EINSTEIN observatory in the soft X-ray band ($h\nu \leq 4.5$ keV). These observations revealed more than ten hitherto unknown X-ray sources and an extended diffuse source (Watson *et al.* 1981; Hertz and Grindlay 1984). Subsequently, soft X-ray observations of the Galactic center were carried out by the ROSAT (Predehl and Trümper 1994), ASCA (Maeda *et al.* 1996), and BeppoSAX (Sidoli *et al.* 1999) observatories. In the hard energy band ($h\nu \geq 10$ keV), this region was fragmentarily observed with the XRT telescope onboard the Spacelab-2 observatory (Skinner *et al.* 1987) and with instruments of the Spartan-1 mission (Kawai *et al.* 1988). A more detailed study of the hard X-ray emission from the center Galactic was carried out with the TTM telescope onboard the Kvant module (Sunyaev *et al.* 1991a) and, in particular, with the ART-P and SIGMA (in gamma-rays) telescopes onboard the Granat observatory (Pavlinsky *et al.* 1992a, 1992b, 1994; Sunyaev *et al.* 1991b).

Persistent X-ray sources of different nature, transients, the millisecond pulsar SAX J1808.4–3658, the bursting pulsar GRO J1744–28, and sources in globular clusters are observed in the Galactic-center region. X-ray bursters, i.e., neutron stars with weak magnetic fields in low-mass binary systems on whose surfaces thermonuclear explosions of the accreted matter occasionally occur, make up a sizeable proportion. The X-ray bursts produced by explosions are difficult to observe, because the burst source cannot always be accurately localized and identified with any persistent X-ray source due to the high concentration of sources in this field. The ART-P/Granat 2.5–30-keV observations of this sky region are unique not only because of their long duration (more than 8×10^5 s) but also because of the telescope's technical potentialities. ART-P can image the sky with a high angular resolution and can perform spectral and timing analyses of any sources in its field of view, irrespective of their number.

Here, we present our observations of the X-ray burster A1742–294 in the immediate vicinity (~1°) of the Galactic center. The emphasis is on the study of peculiarities of bursts from this source.

OBSERVATION

The ART-P X-ray telescope, which is part of the scientific payload of the Granat international astrophysical observatory, can image a selected region of the sky by using a coded-aperture technique. It consists of four coaxial, completely independent modules; each module includes a position-sensitive detector with a geometric area of 625 cm^2 and a coded mask based on URA sequences. The instrument can image the sky within a $3°4 \times 3°6$ field of view (FWHM) with a nominal resolution of ~5 arcmin (the angular size of the mask element). Because of the detector's higher spatial resolution (~1.25 arcmin), the accuracy of localizing discrete sources is several times higher. The telescope is sensitive to photons in the energy range 2.5–60 keV
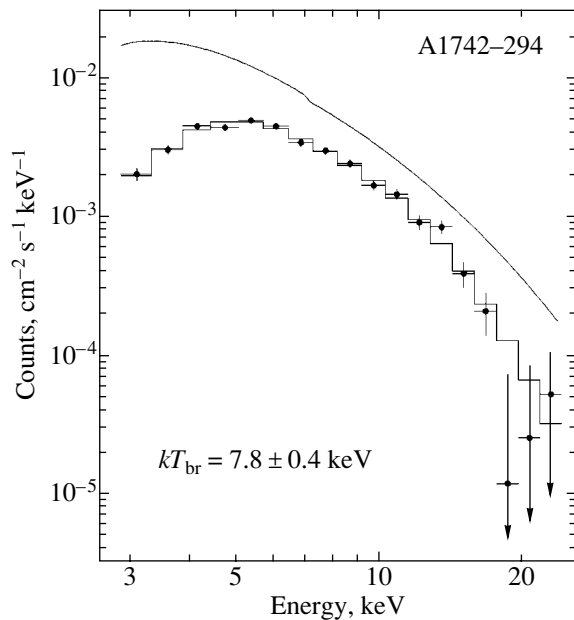
Fig. 1. The persistent spectrum of A1742–294 obtained with the ART-P telescope during the Galactic-center observation on September 9, 1990. The dots indicate the measured (pulse-height) spectrum, and the histogram represents its best fit by the bremsstrahlung model. The model (photon) spectrum is indicated by the solid line.

and has an energy resolution of ~22% in the 5.9-keV iron line. Readings of the star tracker, which determines the instantaneous spacecraft orientation with an accuracy of 1.5 arcmin, are used in imaging and spectral analysis. A more detailed description of the telescope is given in Sunyaev *et al.* (1990).

The observations were carried out in the photon-by-photon mode, in which, for each photon, its coordinates on the detector, energy (1024 channels), and arrival time (the photon arrival time is accurate to within 3.9 ms, and the dead time is 580 μs) were written into the ART-P buffer memory. This mode allows both the timing and spectral analyses of the emission from each X-ray source within the ART-P field of view. Data transfer to the main memory was made after the temporary buffer was filled (once in 150–200 s) during ~30 s, which resulted in breaks in the information; therefore, the data were in the form of individual exposures.

The Galactic center was observed by the Granat observatory in series twice a year, in spring and fall (this was caused by the restrictions imposed on the satellite in-orbit orientation with respect to the Sun). Five series of Galactic-center observations were carried out in 2.5 years of the ART-P operation, with the total observing time being ~830 000 s. This allowed us to analyze in detail the persistent emission from sources in this region, their spectra and variability on various time scales, to discover several new X-ray sources, and to detect more than 100 X-ray bursts (Pavlinsky *et al.* 1992a, 1992b, 1994; Grebenev *et al.* 2001).

It should be noted that the first and fourth ART-P modules were used during the first two series of observations (in the spring and the fall of 1990). The subsequent observations were performed by the third module with a lower sensitivity in the soft energy band (3–8 keV), which hampered and, in several cases, prevented the localization and spectral analysis of the X-ray bursts detected by this module [see Grebenev *et al.* (2001) for more details].

PERSISTENT EMISSION

The X-ray burster A1742–294 is the brightest persistent X-ray source among those located near (within ~1°) the Galactic center; it is responsible for ~1/3 of the total flux from this region in the standard X-ray band (2–20 keV). In this energy band, the source has been repeatedly observed from various satellites. Based on SIGMA/Granat data, Churazov *et al.* (1995) first showed that A1742–294 also radiates in the hard energy band ($h\nu \geq 35$ keV).

X-ray emission from the source was observed every time it fell within the ART-P field of view (Pavlinsky *et al.* 1994). Its 3–20-keV flux was 30–50 mCrab during the 1990 series of observations and slightly decreased to 20–30 mCrab by the spring of 1992. The shape of the burster's persistent spectrum, which is described well by the model of bremsstrahlung from optically thin plasma, remained essentially unchanged. The temperature kT_{br} of this model determined by fitting the spectra of the source in individual observing sessions was within the range 6.4–10.5 keV. When modeling the spectra, we took into account their distortion in the soft energy band by strong interstellar absorption, which is characterized by a hydrogen column density $N_H \simeq 6 \times 10^{22}$ cm^{-2}.

As an illustration, Fig. 1 shows the typical persistent spectrum of A1742–294 measured with the ART-P telescope on September 9, 1990. The dots indicate the pulse-height spectrum (in counts s^{-1} cm^{-2} keV^{-1}), and the solid line represents the corresponding model spectrum (in phot. s^{-1} cm^{-2} keV^{-1}); the temperature that was determined by fitting the spectrum with the model of bremsstrahlung from optically thin plasma is shown in the lower left corner.

X-RAY BURSTS

Lewin *et al.* (1976) discovered that most bursts detected by them from the Galactic-center region originated from three sources, A1742–294, A1742–289, and A1743–28; bursts from the first two sources were observed regularly. Our analysis of the ART-P data revealed no burst from A1742-289 and A1743-28 (in those cases where we managed to perform the localization).

Recurrence

Of more than 100 X-ray bursts detected over the entire period of ART-P observations of the Galactic-

The X-ray bursts detected by the ART-P telescope from A1742–294 during 1990–1992

Date	T_0,[a] UT	kT_{bb}, keV	L_{bb},[b] 10^{37} erg s^{-1}	Flux,[c] mCrab	Duration, s
Mar. 20, 1990	$18^h05^m00^s$	1.64 ± 0.35	2.20 ± 0.65	168 ± 50	26
	20 01 29	1.61 ± 0.53	1.38 ± 0.69	88 ± 44	18
Mar. 24, 1990	18 32 42	2.78 ± 0.73	3.32 ± 0.92	253 ± 70	24
	21 42 00	1.87 ± 0.61	2.35 ± 0.97	199 ± 74	17
Apr. 8, 1990	14 06 38	2.45 ± 0.34	4.26 ± 0.71	281 ± 47	24
Sept. 9, 1990	14 07 48	1.65 ± 0.41	1.81 ± 0.92	115 ± 67	18
	15 53 21	1.89 ± 0.30	3.43 ± 0.86	238 ± 58	17
Sept. 29, 1990	13 32 38	_[d]	_[d]	372 ± 90	30
Oct. 5, 1990	15 31 44	2.02 ± 0.54	1.60 ± 0.69	147 ± 55	32
	19 43 33	1.43 ± 0.48	3.36 ± 1.52	234 ± 125	21
Oct. 6, 1990	22 10 36	1.49 ± 0.23	4.91 ± 1.17	374 ± 89	22
Oct. 9, 1990	17 20 52	2.21 ± 0.59	2.21 ± 0.75	169 ± 57	11
	19 06 11	1.60 ± 0.28	2.59 ± 0.70	162 ± 49	15
Oct. 10, 1990	14 35 48	1.97 ± 0.42	2.39 ± 0.83	183 ± 64	12
	16 06 25	1.55 ± 0.24	2.48 ± 0.76	418 ± 96	9
Oct. 18, 1990	9 50 31	2.15 ± 0.19	7.97 ± 0.96	607 ± 73	17
Feb. 22, 1991	14 07 59	0.97 ± 0.17	8.26 ± 2.53	709 ± 179	13
Feb. 23, 1991	22 24 36	1.98 ± 0.27	7.21 ± 1.90	550 ± 145	16
Feb. 26, 1991	11 00 20	4.79 ± 2.67	2.97 ± 2.51	312 ± 181	15
Apr. 1, 1991	13 39 44	3.51 ± 1.39	3.30 ± 1.19	252 ± 91	28
	15 28 57	1.71 ± 0.84	4.46 ± 1.77	343 ± 136	19
Apr. 8, 1991	13 16 25	1.30 ± 0.25	2.29 ± 2.00	326 ± 152	22
Oct. 15, 1991	19 59 08	_[d]	_[d]	_[d]	14
Oct. 18, 1991	11 44 04	_[d]	_[d]	_[d]	15
Feb. 21, 1992	12 52 53	1.86 ± 0.43	4.51 ± 1.53	283 ± 115	21
Mar. 2, 1992	1 43 22	2.01 ± 0.33	10.06 ± 3.18	963 ± 239	15

[a] The burst peak time (UT).
[b] The source's mean 6–20-keV luminosity during the burst at a distance of 8.5 kpc.
[c] The source's mean 6–20-keV flux during the burst.
[d] The source's spectrum cannot be reconstructed for technical reasons.

center region, 26 bursts with a duration of ~15 s were identified with the burster A1742–294 (see the table). Criteria for the detection of bursts and their identification with persistent sources can be found in Grebenev et al. (2001), whence some of the data in this table were taken. At the same time, note that the burst parameters in the table were obtained from a spectral analysis of the emission observed during bursts; i.e., it is a continuation and expansion of the study of bursts initiated by Grebenev et al. (2001). Two successive bursts at a time were observed during several sessions, which allowed us to directly measure the characteristic burst recurrence time t_r. The measured values of t_r lie in the range 1.5 to 4.2 h with a mean of ~2.4 h, which is several-fold smaller than the value found by Lewin et al. (1976). The mean energy spectra of the detected bursts are satisfactorily described by a blackbody model whose temperature kT_{bb} changes from burst to burst in the range ~1–3 keV (see the table) with the mean $kT_{bb} = 1.81 \pm 0.39$ keV.

The characteristic burst recurrence time t_r can be estimated if the source's persistent and burst luminosities are known: $t_r \simeq \alpha \Delta t L_b / L_p$, where L_p is the persistent luminosity, L_b is the mean burst luminosity, Δt is the burst duration, and $\alpha \sim 100$ is the ratio of energy release during accretion to that during thermonuclear helium burning. The derived value, $t_r \sim 3$ h, is in satisfactory agreement with direct measurements.

Burst Profiles

When analyzing the time profiles of the X-ray bursts detected from A1742–294, we found them to depend on the mean 3–20-keV flux measured during the burst
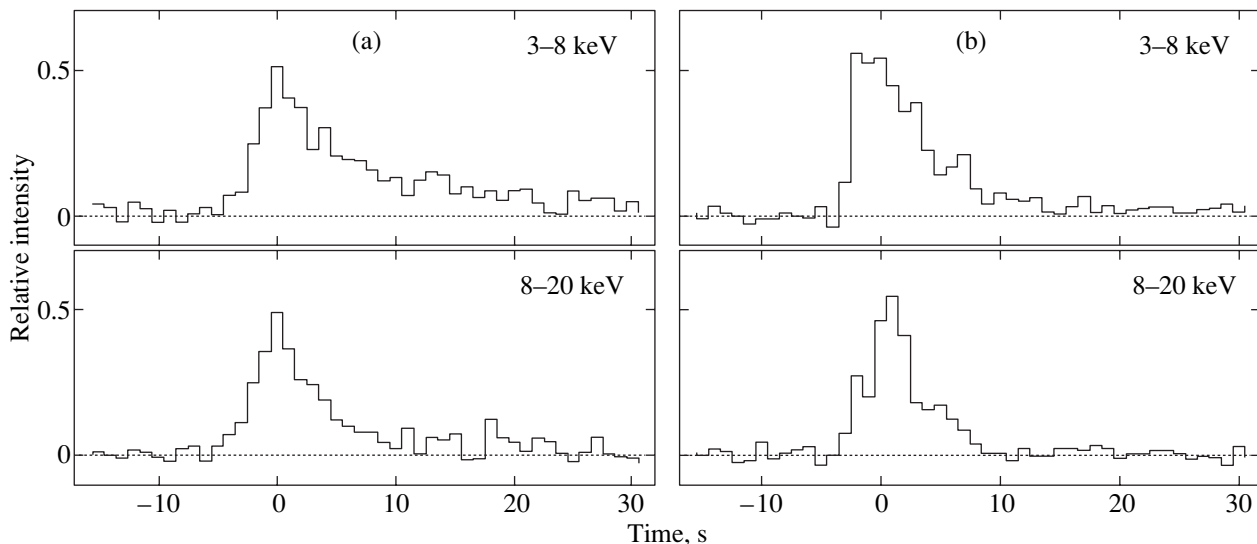
Fig. 2. The average profiles of bursts with different intensities observed from A1742–294 in various energy bands.

(Grebenev *et al.* 2001) at a mean flux of ~100–300 mCrab, the profile is nearly triangular; i.e., the rise time of the burst (~5 s) is close to its decay time, whereas the burst profile becomes classical; i.e., it is characterized by a sharp rise (~1–2 s) followed by a smooth decay, when the flux increases to ~600–1000 mCrab. Bursts of the second type occur much more rarely than bursts of the first type, so two such events in a row have never been observed during a single session. To analyze the above dependence in more detail, we constructed average profiles for the bursts of each type. Because of the spectral peculiarities of the third ART-P module, we used only data from the first and fourth modules. In our subsequent analysis, we rejected bursts that partially occurred at the beginning or at the end of the exposures. Each of the twelve remaining bursts was reduced to a dimensionless intensity scale in the band 3–20 keV by its normalization to the difference between the maximum burst count rate and the persistent count rate determined from the exposure that preceded the exposure during which the burst was detected. Subsequently, the dimensionless bursts were added by matching the peaks and averaged. The results of this averaging for triangular bursts in two energy bands are shown in Fig. 2a. For comparison, Fig. 2b shows the profile of the classical burst detected by ART-P on October 18, 1990, in the same energy bands. This was the only burst of this shape and intensity detected by the telescope's fourth module. Three more such events were observed by the third module.

The differences in the burst profiles are clear: whereas the burst in Fig. 2a has a triangular shape in the soft and hard energy bands similar to the shape of the burst in Fig. 2b at high energies, the profile of the latter in the 3–8-keV energy band is strictly classical in shape: a sharp (~1 s) rise and a smooth exponential decay. This fact leads us to conclude that low-energy

X-ray emission is responsible for the profile shape of the X-ray bursts observed from A1742–294. Note also that a softening of the source's spectrum during the burst clearly shows up in both figures: the decay time in the hard energy band is considerably shorter than that in the soft energy band, which is one of the characteristic features of type I bursts.

The Burst of October 18, 1990

On this day, the ART-P telescope detected the strongest and most interesting burst from A1742–294, during which the peak X-ray 3–20-keV flux was ~1.5 Crab. Figure 3 shows the source's measured light curves in various energy bands during this burst. The time profile of the burst suggests that it belongs to type I bursts, which are caused by thermonuclear explosions on the neutron-star surface. We see that the peak flux in the hard energy bands is reached later than that in the soft energy bands; i.e., the burst rise time in the 12–16-keV energy band (~5 s) is considerably longer than the rise time in the 4–8-keV energy band (1–2 s). Given that the *e*-folding exponential decay time of the burst t_{exp} decreases from 8.7 s in the 4–8-keV band to 3.9 s in the 8–12-keV band, to 2.3 s in the 12–16-keV band, and to 1.5 s in the 16–20-keV band, the total burst duration in the hardest energy band turns out to be several-fold shorter than that in the softest band (Fig. 3). The energy dependence of t_{exp} indicates that the source's spectrum had softened appreciably by the end of the burst, which is one of the characteristic features of type I X-ray bursts. Note that no statistically significant excess of the signal over the background was found during the burst in the harder energy band ($h\nu \geq 20$ keV).

To trace the evolution of the source's parameters during the burst, we divided it into seven time intervals, reconstructed the photon spectrum for each of them,
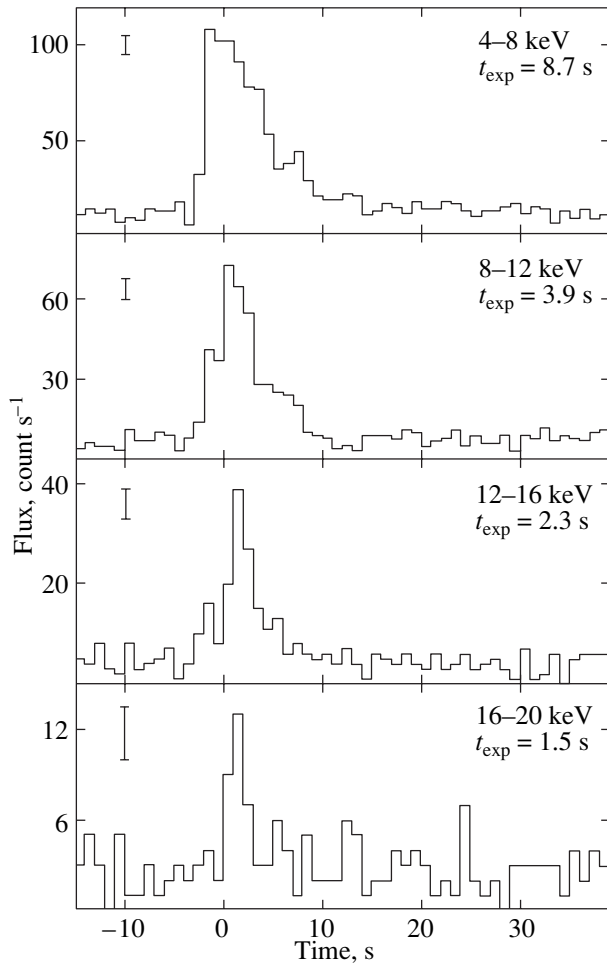
Fig. 3. The profiles of the X-ray burst detected on October 18, 1990, from A1742–294 in various energy bands with a time resolution of 1 s: t_{exp} is the source's *e*-folding decay time in each band. The errors correspond to one standard deviation.
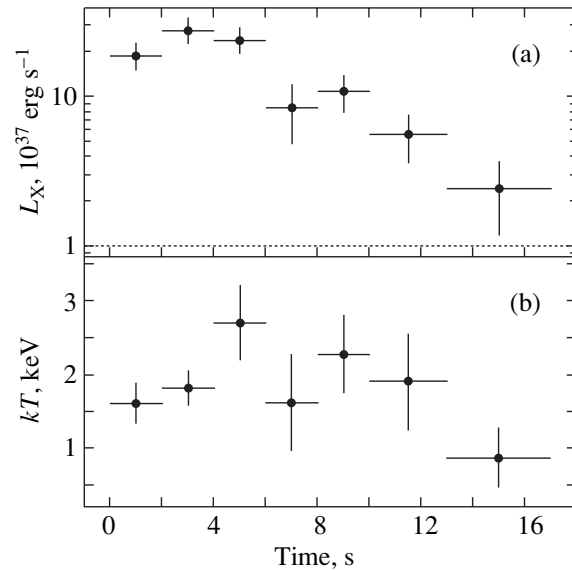

Fig. 4. Evolution of the source's luminosity (a) and temperature (b) determined by fitting the spectra of A1742–294 with a blackbody model during the strong burst detected on October 18, 1990. The dotted line indicates the source's persistent luminosity.

DISCUSSION

Long-term observations of the Galactic center with instruments of the Granat observatory have allowed us

and fitted it by a blackbody model. Variations of the source's temperature and luminosity in the 3–20-keV energy band during the burst determined in the above model are shown in Fig. 4. The source's burst-averaged spectrum is described well by the radiation law of a blackbody with a temperature $kT_{bb} \simeq 2.15 \pm 0.19$ keV, a radius $R_{bb} \simeq 6.4 \pm 1.4$ km, and a 3–20-keV flux $F_{bb} \simeq (1.35 \pm 0.13) \times 10^{-8}$ erg cm^{-2} s^{-1}, which corresponds to a luminosity $L_{bb} \simeq 1.2 \times 10^{38}$ erg s^{-1} at a distance of 8.5 kpc. In Fig. 5, this spectrum is compared with the persistent spectrum of A1742–294. The inferred temperature, which corresponds to the super-Eddington flux, and the small blackbody radius suggest that the spectrum is distorted by Comptonization, while the dip clearly seen in the burst profile at high energies apparently points to the photospheric expansion in the source that took place at the initial burst stage.

not only to analyze in detail the timing and spectral parameters of persistent sources in this region, but also to detect more than 100 X-ray bursts; we managed to identify 26 of these bursts with the X-ray burster A1742–294 in the immediate vicinity of Galactic-center region. Long continuous observing sessions (more than 10 h) made it possible to directly measure the burst recurrence time. The derived mean value, $t_r \sim 2.4$ h, proved to be several-fold shorter than assumed previously.

The X-ray bursts detected by ART-P from this source can be arbitrarily divided into ordinary (with a mean burst flux of 100–300 mCrab) and strong (a mean flux of 600–1000 mCrab). The burst profiles differ significantly: ordinary bursts are triangular (the rise time is comparable to the decay time), while strong bursts are classical in shape (a sharp rise followed by a smooth decay).

The mean energy release during the burst did not depend on the source's pre-burst luminosity and was $E \simeq 9 \times 10^{38}$ ergs for ordinary bursts and $E \simeq 2 \times 10^{39}$ ergs for strong bursts. To provide such energy yields, $M \simeq E/\epsilon_{He} \simeq 5.0 \times 10^{21}$ and 1.1×10^{20} g of matter, respectively, must be accreted onto the neutron-star surface (here, $\epsilon_{He} \simeq 0.002c^2$ is the helium burning efficiency). The rate of accretion onto the neutron star in quiescence can be represented as $\dot{M} = L_X R_{ns}/GM_{ns}$, where L_X, $M_{ns} \simeq 1.4M_\odot$, and $R_{ns} \simeq 10$ km are the luminosity, mass, and radius of the neutron star, respectively. Assuming that the burster's mean luminosity in quiescence is $L_X \simeq 8 \times 10^{36}$ erg s^{-1}, we can estimate the characteristic times τ in which the required amount of mat-
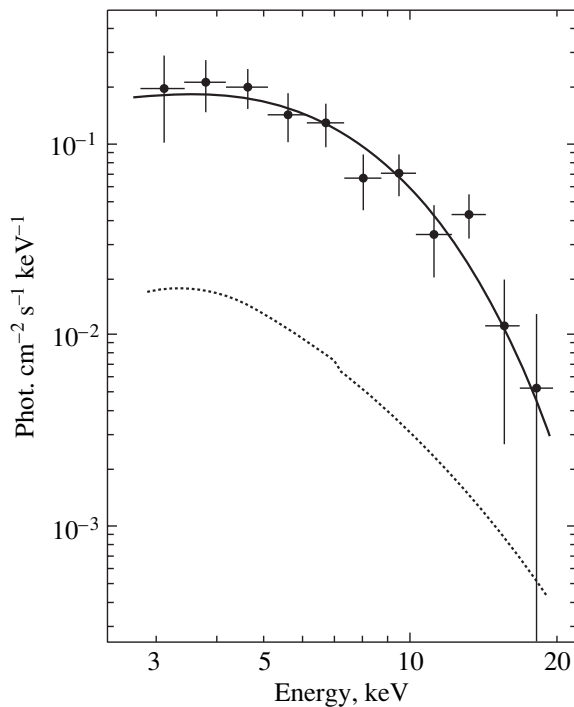
Fig. 5. The photon spectrum of A1742–294 averaged over the entire October 18, 1990 burst. The solid line represents the model blackbody spectrum that provides the best fit to the data. For comparison, the dotted line indicates the source's persistent spectrum.

ter will be accreted onto the neutron-star surface: $\tau \simeq 3.2$ and 7.2 h for ordinary and strong bursts, respectively.

The observation of both ordinary (weak) and strong X-ray bursts from A1742–294 and the fact that the latter are observed much more rarely can be naturally explained in terms of the above estimates. The difference in the burst time profiles may stem from the fact that the thermonuclear explosion responsible for the burst takes place not instantaneously over the entire neutron-star surface, but only in its region where local conditions for thermonuclear burning were created, and it subsequently spreads over the entire neutron-star surface. Depending on the amount and density of accumulated matter, the burning front propagates in subsonic mode, deflagration (weak bursts), or in supersonic mode, detonation (strong bursts). The criteria for realization of these modes were studied in detail by Fryxell and Woosley (1982). That is why the profiles of ordinary bursts have a longer rise compared to strong bursts.

ACKNOWLEDGMENTS

REFERENCES

1. E. Churazov, M. Gilfanov, R. Sunyaev, *et al.*, Astrophys. J. **443**, 341 (1995).
2. B. A. Fryxell and S. E. Woosley, Astrophys. J. **261**, 332 (1982).
3. S. A. Grebenev, A. A. Lutovinov, M. N. Pavlinsky, *et al.*, Pis'ma Astron. Zh. **27** (2001) (in press) [Astron. Lett. **27** (2001) (in press)].
4. P. Hertz and J. Grindlay, Astrophys. J. **278**, 137 (1984).
5. N. Kawai, E. Fenimore, J. Middleditch, *et al.*, Astrophys. J. **330**, 130 (1988).
6. W. H. G. Lewin, J. A. Hoffman, J. Doty, *et al.*, Mon. Not. R. Astron. Soc. **177**, 83P (1976).
7. Y. Maeda, K. Koyama, M. Sakano, *et al.*, Publ. Astron. Soc. Jpn. **48**, 417 (1996).
8. M. N. Pavlinsky, S. A. Grebenev, and R. A. Sunyaev, Pis'ma Astron. Zh. **18**, 217 (1992a) [Sov. Astron. Lett. **18**, 88 (1992a)].
9. M. N. Pavlinsky, S. A. Grebenev, and R. A. Sunyaev, Pis'ma Astron. Zh. **18**, 291 (1992b) [Sov. Astron. Lett. **18**, 116 (1992b)].
10. M. N. Pavlinsky, S. A. Grebenev, and R. A. Sunyaev, Astrophys. J. **425**, 110 (1994).
11. P. Predehl and J. Trümper, Astrophys. J. Lett. **290**, L29 (1994).
12. R. Proctor, G. Skinner, and A. Willmore, Mon. Not. R. Astron. Soc. **185**, 745 (1978).
13. L. Sidoli, S. Mereghetti, G. Israel, *et al.*, Astrophys. J. **525**, 215 (1999).
14. G. Skinner, A. Willmore, C. Eyles, *et al.*, Nature **330**, 544 (1987).
15. R. A. Sunyaev, S. I. Babichenko, D. A. Goganov, *et al.*, Adv. Space Res. **10** (2), 233 (1990).
16. R. A. Sunyaev, K. Borozdin, M. R. Gilfanov, *et al.*, Pis'ma Astron. Zh. **17**, 126 (1991a) [Sov. Astron. Lett. **17**, 54 (1991a)].
17. R. Sunyaev, E. Churazov, M. Gilfanov, *et al.*, Astrophys. J. Lett. **383**, L49 (1991).
18. M. Watson, R. Willingale, J. Grindlay, *et al.*, Astrophys. J. **250**, 142 (1981).

Translated by V. Astakhov

New Generation Mechanisms
for X-ray Quasi-Periodic Oscillations in Accreting Neutron Stars

Yu. N. Gnedin* and S. O. Kiĭkov

Pulkovo Astronomical Observatory, Russian Academy of Sciences, Pulkovskoe sh. 65, St. Petersburg, 196140 Russia
Received August 16, 2000; in final form, March 12, 2001

Abstract—We propose three mechanisms for the generation of quasi-periodic oscillations (QPOs) in X-ray binaries. Two of them are based on an analogy with nonlinear oscillations of gaseous cavities in a fluid. The first mechanism, called magnetocavitation, implies that X-ray QPOs are produced by radial oscillations of the neutron-star magnetosphere interacting with accreted plasma. The photon-cavitation mechanism is considered when studying X-ray QPOs in neutron stars with critical (Eddington) luminosities. In this case, X-ray QPOs are generated by radial oscillations of photon cavities in the fully ionized hydrogen plasma that settles in the accretion column of a compact object. The mechanism according to which X-ray QPOs result from nonlinear oscillations of current sheets originating in accretion disks is suggested to explain QPOs in X-ray binaries with black holes and in cataclysmic variables. The calculated values of basic physical parameters of QPOs, such as the characteristic frequency, the dependences of QPO frequency and amplitude on X-ray flux, photon energy, and QPO lag time between photons at different energies are in good agreement with observational data. © 2001 MAIK "Nauka/Interperiodica".

Key words: *plasma astrophysics, hydrodynamics, and shock waves; pulsars, neutron stars, and black holes*

INTRODUCTION

Quasi-periodic oscillations (QPOs) of high-frequency electromagnetic radiation is a phenomenon that is typical of many astrophysical objects, including X-ray binaries, gamma-ray sources, cataclysmic variables, flare stars, and galactic nuclei. These oscillations can be divided into three groups: short-period QPOs with frequencies in the range 100 Hz to $\gtrsim$1 kHz, QPOs with frequencies $\lesssim$100 Hz, and long-period QPOs with periods from several seconds to several minutes.

QPOs with frequencies of several tens of Hz were first discovered by the EXOSAT satellite in low-mass X-ray binaries, such as GX 5-1, Sco X-1, and others (van der Klis *et al.* 1985a, 1985b, 1985c, 1987; van der Klis and Jansen 1986; Hasinger *et al.* 1985, 1986; Lewin *et al.* 1987; van der Klis 1989). An example of the QPO power spectrum was given, for example, by van der Klis (1989). After the RXTE (Rossi X-ray Timing Explorer) satellite was launched, QPOs with frequencies in the range 100 Hz to $\gtrsim$1 kHz were discovered in eighteen low-mass X-ray binaries (Berger *et al.* 1996; Wijnands *et al.* 1996; van der Klis *et al.* 1996a, 1996b, 1996c; Smale *et al.* 1996; Strohmayer *et al.* 1996; Bradt 1999). QPOs with frequencies ~1 kHz are revealed, for example, by the power spectrum of Sco X-1 (Klein *et al.* 1996). As for QPOs with periods from several second

to hundreds of seconds, they were detected in both cataclysmic variables, novalike stars and dwarf novae (Patterson 1981; Warner 1987, 1995; Mauche 1996; Gnedin *et al.* 1999), and in low-mass X-ray binaries (Robinson and Nather 1979; Cordova and Mason 1983; Matsuoka 1985).

To explain the wide frequency range and the different characteristic properties of QPOs requires invoking various physical mechanisms. The following mechanisms have been proposed: (1) frequency beating, when oscillations occur with a frequency equal to the difference between the Keplerian orbital frequency of the accreted matter in an accretion disk and the rotation frequency of a compact star (a neutron star or a white dwarf) (Alpar and Shaham 1985a, 1985b); (2) instability of the marginally stable circular orbit, with the QPO frequency being determined by the Keplerian orbital frequency of the accreted matter in an accretion disk in this orbit (Kaaret *et al.* 1997); and (3) photon-bubble instability, with X-ray QPOs resulting from variations in the number of photon bubbles in the accretion column of a neutron star (Hsu *et al.* 1997). Recently, Titarchuk *et al.* (1998) have proposed a QPO model in which a hot blob is formed at the outer boundary of the transition layer in an accretion disk oscillating under the action of the Coriolis force. They called this blob a Keplerian oscillator, which shows double-mode oscillations under the action of the Coriolis force. However, the above mechanisms do not explain all the peculiarities of QPOs [for example, the correlation between

---

* E-mail address for contacts: gnedin@gao.spb.ru

QPO frequency and count rate (radiation intensity) in the X-ray band] and run into a number of fundamental difficulties. Thus, for example, the instability mechanism of the marginally stable circular orbit, as applied to X-ray binaries with accreting neutron stars (NSs), constrains the NS masses too severely by requiring that their values be ~$2M_\odot$ or even higher. At the same time, observations of most close X-ray binaries give the most probable NS masses of ~$1.4M_\odot$.

Here, we propose three possible mechanisms for the generation of nonlinear QPOs in the X-ray flux from NSs in close binaries. The first involves oscillations of the magnetosphere treated as a magnetized gaseous cavity. Below, this mechanism is called magnetocavitation. When describing the second mechanism, we consider oscillations of the photon cavities originating in the accretion column of a NS undergoing super-Eddington accretion (Hsu *et al.* 1997). We call this mechanism photon cavitation. The third mechanism is associated with nonlinear oscillations of current sheets in accreted plasma, for example, in accretion disks and in the columns of compact objects. This mechanism has already been successfully used to describe facular oscillations in the solar atmosphere (Sakai *et al.* 1987). Not only the observed characteristic QPO frequencies but also other recently discovered QPO properties, such as a correlation between QPO frequency and X-ray flux (Bradt 1999) and various complex forms of the time lag between QPOs in different spectral ranges (Vaughan *et al.* 1997; Wijnands *et al.* 1999; Kaaret *et al.* 1999; Ford *et al.* 1997, 1999; Yu *et al.* 1999), can be explained in terms of these mechanisms.

The relations of the cavitation theory that describe the dynamics of gas bubbles in a fluid (Knapp *et al.* 1974; Neppiras 1980; Krasil'nikov and Krylov 1984) underlie the magnetocavitation and photon-cavitation mechanisms. Therefore, before considering the generation mechanisms for X-ray QPOs in NSs, we briefly describe the cavitation process in a fluid.

BASIC CAVITATION EQUATIONS

The formation of bubbles (or cavities) filled with vapor, gas, or their mixture in a fluid is called cavitation (Knapp *et al.* 1974; Neppiras 1980). In the course of time, the bubbles oscillate and collapse, breaking up into smaller bubbles. Such collapse takes place under the pressure that can be produced by an external acoustic field. To study cavitation requires considering the problem of bubble interaction with a fluid. Solving this problem involves determining the location and shape of the bubble surface, as well as the parameters that characterize the bubble physical state and the surrounding fluid. When the bubble dynamics is investigated, it is commonly assumed that the bubble is spherical, all the quantities that characterize its state are functions of the time alone, and the gas contained in it obeys an adiabatic law. We assume that the fluid is a viscous incompressible medium; its motion around the bubble is

spherically symmetric; and the effects of heat conduction, diffusion, and surface tension are negligible. The equations and boundary conditions that describe the state of the fluid and the bubble interacting with it then take the form (Landau and Lifshitz 1987, 1980)

$$\frac{\partial v}{\partial t} + v\frac{\partial v}{\partial r} = -\frac{1}{\rho}\frac{\partial p}{\partial r} + \frac{\mu}{\rho}\left(\frac{1}{r^2}\frac{\partial}{\partial r}\left(r^2\frac{\partial v}{\partial r}\right) - \frac{2v}{r^2}\right), \quad (1)$$

$$\frac{\partial v}{\partial r} + \frac{2v}{r} = 0, \tag{2}$$

$$p_g = p_{g0}\left(\frac{R_0}{R}\right)^{3\gamma}, \tag{3}$$

$$p(R) - 2\mu\frac{\partial v}{\partial r}\bigg|_{r=R} = p_b(R), \tag{4}$$

$$v|_{r=R} = \frac{dR}{dt} = \dot{R}, \tag{5}$$

where v, ρ, p, and μ are the radial velocity, density, pressure, and dynamic viscosity of the fluid, respectively; R_0 and R are the bubble radii at equilibrium time t_0 and at arbitrary time t; $p_{g0} = p_g(R_0)$ and $p_g = p_g(R)$ are the bubble gas pressures at times t_0 and t, respectively; γ is the adiabatic index; and $p_b(R)$ is the total bubble pressure, which is the sum of the gas and vapor pressures.

Integrating the continuity equation (2) using (5) yields an expression for the fluid velocity field around the bubble:

$$v(r, t) = \frac{\dot{R}R^2}{r^2}. \tag{6}$$

Substituting (6) in (1) gives

$$\frac{2R\dot{R}^2 + R^2\ddot{R}}{r^2} - \frac{2R^4\dot{R}^2}{r^5} = -\frac{1}{\rho}\frac{\partial p}{\partial r}. \tag{7}$$

Assuming that the fluid motion in the region $R < r < L$, where L is some distance from the bubble center, is spherically symmetric and integrating Eq. (7) from R to L, we obtain

$$R\ddot{R} + \frac{3}{2}\dot{R}^2 - \frac{1}{L}(2R\dot{R}^2 + R^2\ddot{R}) + \frac{R^4\dot{R}^2}{2L^4}$$
$$= \frac{1}{\rho}(p(R) - p(L, t)). \tag{8}$$

Eq. (8), together with Eqs. (3) and (4), describes nonlinear changes in the bubble radius and is the basic equation that underlies the magnetocavitation and photon-cavitation mechanisms.

THE MAGNETOCAVITATION MECHANISM

As was said above, one of the mechanisms proposed to describe nonlinear X-ray QPOs in NSs is magneto-

cavitation. According to this mechanism, X-ray QPOs are caused by oscillations of the NS magnetosphere interacting with accreted plasma; the magnetosphere and the plasma are treated as a magnetized gaseous cavity and a viscous incompressible fluid, respectively. We assume that the magnetospheric gas obeys an adiabatic law and that the accreted-plasma motion is spherically symmetric. In this case, the equations and boundary conditions that describe the state of the magnetosphere and its surrounding plasma can be written as (Landau and Lifshitz 1987, 1984, 1980)

$$\frac{\partial v}{\partial t} + v\frac{\partial v}{\partial r}$$

$$= -\frac{1}{\rho}\frac{\partial p}{\partial r} + \frac{\mu}{\rho}\left(\frac{1}{r^2}\frac{\partial}{\partial r}\left(r^2\frac{\partial v}{\partial r}\right) - \frac{2v}{r}\right) - G\frac{M_s}{r^2}, \qquad (9)$$

$$\frac{\partial v}{\partial r} + \frac{2v}{r} = 0, \qquad (10)$$

$$p_g = p_{g0}\left(\frac{R_0}{R}\right)^{3\gamma}, \qquad (11)$$

$$p(R) - 2\mu\frac{\partial v}{\partial r}\Big|_{r=R} = p_g\big|_{r=R} + \frac{H^2}{8\pi}\Big|_{r=R}, \qquad (12)$$

$$v|_{r=R} = \frac{dR}{dt} = \dot{R}, \qquad (13)$$

where v, ρ, p, and μ are the radial velocity, density, pressure, and dynamic viscosity of the accreted plasma, respectively; G is the gravitational constant; M_s is the NS mass; R and R_0 are the magnetospheric radii at arbitrary and equilibrium times, respectively; p_g and p_{g0} are the magnetospheric gas pressures at arbitrary and equilibrium times; γ is the adiabatic index; and H is the magnetic field strength at the Alfvén surface.

Integrating Eqs. (9)–(13) yields

$$R\ddot{R} + \frac{3}{2}\dot{R}^2 - \frac{1}{L}(2R\dot{R}^2 + R^2\ddot{R}) + \frac{R^4\dot{R}^2}{2L^4}$$

$$= \frac{1}{\rho}\left(\left(p(L, t_0) - \frac{H_0^2}{8\pi}\right)\left(\frac{R_0}{R}\right)^{3\gamma}\right. \qquad (14)$$

$$\left. + \frac{H^2}{8\pi} - 4\mu\frac{\dot{R}}{R} - p(L, t)\right) + GM_s\left(\frac{1}{L} - \frac{1}{R}\right),$$

where L is some distance from the magnetospheric center, $L > R$. According to the relation (Lipunov 1987)

$$R_c = R_s\sqrt{\frac{R_s}{R}}, \qquad (15)$$

where R_c is the linear radius of the accretion column, R_s is the NS radius, and R is the radius of the Alfvén surface, oscillations of the magnetospheric radius R cause variations in R_c and, consequently, variations in

the area of the X-ray-emitting surface. Thus, in view of Eq. (15), Eq. (14) describes nonlinear variations in the NS X-ray flux.

When the radius of the Alfvén surface changes only slightly, Eq. (14) can be linearized. The square of the (cyclic) frequency of free oscillations is then given by

$$\omega^2 = \frac{1}{\rho R_0^2}\left(1 - \frac{R_0}{L}\right)^{-1}\left(3\gamma p(L, t_0)\right.$$

$$\left. - \frac{3\gamma H_0^2}{8\pi} - \frac{H_0 R_0}{4\pi}\frac{dH}{dR}\Big|_{R=R_0} - \frac{GM_s\rho}{R_0}\right). \qquad (16)$$

Below, we assume that $\dfrac{R_0}{L} \ll 1$.

Let us consider the cases where $HR^2 = $ const and $HR^3 = H_s R_s^3 = $ const, where H_s is the NS surface magnetic field strength. The first condition is applicable to problems with conserved magnetic flux, while the second condition holds for a dipole magnetic field. Below, we analyze the latter case in more detail.

For $HR^2 = $ const, Eq. (16), in view of the condition $\dfrac{R_0}{L} \ll 1$, takes the form

$$\omega^2 = \frac{1}{\rho R_0^2}\left(3\gamma p_0 - \frac{H_0^2}{2\pi}\left(1 - \frac{3}{4}\gamma\right) - \frac{GM_s\rho}{R_0}\right), \qquad (17)$$

and the oscillation period is

$$T = \frac{2\pi}{\omega} = 2\pi R_0\sqrt{\frac{\rho}{3\gamma p_0 + \dfrac{H_0^2}{2\pi}\left(1 - \dfrac{3}{4}\gamma\right) - \dfrac{GM_s\rho}{R_0}}}, \qquad (18)$$

where $p_0 = p(L, t_0)$.

For a dipole magnetic field, $HR^3 = $ const and Eq. (16) at $\dfrac{R_0}{L} \ll 1$ can be written as

$$\omega^2 = \frac{1}{\rho R_0^2}\left(3\gamma p_0 + \frac{3H_0^2}{4\pi}\left(1 - \frac{1}{2}\gamma\right) - \frac{GM_s\rho}{R_0}\right), \qquad (19)$$

and the oscillation period is

$$T = 2\pi R_0\sqrt{\frac{\rho}{3\gamma p_0 + \dfrac{3H_0^2}{4\pi}\left(1 - \dfrac{1}{2}\gamma\right) - \dfrac{GM_s\rho}{R_0}}}. \qquad (20)$$

Using Eqs. (19) and (20) and taking into account Eq. (15), let us estimate the frequency $f = \omega/2\pi$ and period of QPOs in the X-ray flux from a NS. If the NS polar magnetic field strength is $H_s = 10^{12}$ Oe, the NS radius is $R_s = 10^6$ cm, and the equilibrium radius of the Alfvén surface is $R_0 = 10^8$ cm, we then find from the

relation $H_0 R_0^3 = H_s R_s^3$ that the magnetic field strength at the magnetospheric boundary is $H_0 = 10^6$ Oe. For $R_0 = 10^8$ cm, $H_0 = 10^6$ Oe, $\gamma = 0$, $\rho = 2 \times 10^{-8}$ g cm^{-3}, $p_0 = 4 \times 10^{10}$ dynes cm^{-2}, $M_s \approx 2.8 \times 10^{33}$ g, and $G = 6.67 \times 10^{-8}$ dynes cm^2 g^{-2}, we obtain from Eqs. (19) and (20) $f = \omega/2\pi \approx 5$ Hz and $T \approx 0.2$ s. This value falls within the observed QPO frequency range 10–100 Hz. Note that the density ρ corresponds to an accretion rate $\dot{M} \approx 5 \times 10^{18}$ g s^{-1}. If we ignore the gravitational field in Eqs. (19) and (20), the derived QPO frequency and period are $f = \omega/2\pi \approx 5.5$ Hz and $T \approx 0.18$ s, respectively. Thus, gravitation has a marginal effect on the QPO frequency and period. By varying the parameters in Eq. (19), we can obtain frequencies from 10 Hz to 1 kHz.

Let us analyze nonlinear oscillations of the Alfvén surface. Disregarding the viscosity and gravitation and assuming that $\dfrac{R_0}{L} \ll 1$, we integrated Eq. (14). As a result, we obtained the period of free nonlinear magnetospheric oscillations and, hence, according to Eq. (15), the period of NS X-ray QPOs:

$$T = 1.135 \rho^{1/2} (p(L, t_0))^{-5/6}$$
$$\times \left(\frac{4\pi R_m^3}{3} \left(p(L, t_0) + \frac{p_m}{\gamma - 1} + \frac{H_m^2}{8\pi} \right) \right)^{1/3}, \quad (21)$$

where R_m is the maximum magnetospheric radius and H_m and p_m are the corresponding magnetic field strength and gas pressure in the magnetosphere. The estimates given by Eq. (21) are in good agreement with observational data. The corresponding frequencies lie in the range 10 Hz to 1 kHz.

Note that if we ignore the magnetic field in Eq. (21), we will derive the standard relation for the period of free nonlinear oscillations of a gaseous bubble in a fluid (Neppiras 1980).

Thus, the magnetocavitation mechanism can describe X-ray QPOs in NSs at frequencies from 10 Hz to 1 kHz.

The following circumstance is noteworthy. Of course, the model of a spherical magnetized gaseous bubble is only the first approximation for describing the actual NS magnetosphere. The QPO frequency calculated in this approximation can be considered as the frequency of the fundamental mode. Let us now analyze the dependence of QPO frequency on the X-ray luminosity of a NS. Assuming a dipole magnetic field and disregarding the gravitation and gas pressure, we rewrite Eq. (19) as

$$\omega = \frac{H_0}{R_0} \sqrt{\frac{3}{4\pi\rho}} = \frac{v_a \sqrt{3}}{R_0}, \quad (22)$$

where v_a is the Alfvén velocity. Using Eq. (22), we can easily express the QPO frequency in terms of basic parameters of the accreted plasma and the accreting NS

itself. For this purpose, we use the formulas of accretion theory (Lipunov 1987). The magnetic field at the magnetospheric boundary is

$$H_0 = \frac{\mu_s}{R_0^3}, \quad (23)$$

where $\mu_s = H_s R_s^3$ is the dipole moment. In the theory of spherically symmetric accretion, the Alfvén radius is defined as

$$R_0 = \left(\frac{\mu_s^2}{\dot{M} \sqrt{2GM_s}} \right)^{2/7}, \quad (24)$$

where $\dot{M}$ is the accretion rate given by

$$\dot{M} = \frac{L_X R_s}{GM_s}, \quad (25)$$

L_X is the NS X-ray luminosity. Since $v_{ff} = \sqrt{\dfrac{2GM_s}{R_0}}$ at the Alfvén surface, we have

$$\omega \approx \frac{\sqrt{6GM_s}}{R_0^{3/2}} \sim \frac{\dot{M}^{3/7} M_s^{5/7}}{\mu_s^{6/7}} \sim \frac{\dot{M}^{3/7} M_s^{5/7}}{H_s^{6/7}} \sim \frac{L_X^{3/7} M_s^{5/7}}{H_s^{6/7}}. \quad (26)$$

Eq. (26) shows that, all things being equal, the QPO frequency increases with X-ray luminosity and decreases with growing NS magnetic field. Ghosh and Lamb (1992) (see also Campana et al. 1998) calculated the magnetospheric radius by using the theory of disk accretion:

$$R_0 = 5 \times 10^6 \dot{M}^{-46/187} H_s^{108/187} M_s^{-41/187} R_s^{324/187} \text{ cm}. \quad (27)$$

If we assume that the accreted-matter density in the disk is $\rho \sim \dot{M}$ and depends only slightly on distance, then the following dependence of QPO frequency on X-ray luminosity L_X and NS surface magnetic field H_s can be derived from Eq. (27):

$$\omega \sim \frac{\dot{M}^{1/2}}{H_s^{245/187}} \sim \frac{L_X^{1/2}}{H_s^{13/10}}. \quad (28)$$

Thus, in this case, the QPO frequency also increases with X-ray luminosity of an accreting NS and decreases with its growing surface magnetic field.

THE PHOTON-CAVITATION MECHANISM

In the fully ionized hydrogen plasma settling in the accretion column of a strongly magnetized NS with a critical Eddington X-ray luminosity, regions with a lower plasma density and a higher radiation pressure than in the ambient medium are known (Arons 1992) to be formed under a radiation-dominated shock wave at heights of several kilometers above the stellar surface. These regions were called photon bubbles or photon

cavities. The formation of photon cavities is shown in diagrams from Hsu *et al.* (1997). According to calculations (Klein *et al.* 1996a) based on the laws of radiation gas-dynamics (Arons and Klein 1987), the number of these cavities changes with time, causing X-ray QPOs in NSs. These oscillations, called photon-bubble oscillations, have been experimentally confirmed. Thus, for example, Klein *et al.* (1996b) showed that the X-ray QPOs revealed by RXTE observations in GRO J1744-28 and Sco X-1 fall within the frequency range predicted by theory. However, this theory does not take into account the peculiarities of the evolution of photon cavities. These peculiarities include oscillations of the cavities themselves, which will contribute to the quasi-periodic X-ray flux variations in NSs.

Here, we propose the photon-cavitation mechanism according to which nonlinear X-ray QPOs in NSs are generated by oscillations of the photon cavities interacting with accreted plasma. The photon cavity is assumed to be roughly spherically symmetric; the parameters of its state are functions of the time alone, and the photon gas in the cavity obeys an adiabatic law. In addition, the accreted plasma is treated as a viscous incompressible fluid whose motion around the cavity is spherically symmetric. The effects of heat conduction and diffusion are assumed to be negligible. The equations and boundary conditions that describe the state of the photon cavity and plasma can then be written as

$$\frac{\partial v}{\partial t} + v\frac{\partial v}{\partial r} = -\frac{1}{\rho}\frac{\partial p}{\partial r} + \frac{\mu}{\rho}\left(\frac{1}{r^2}\frac{\partial}{\partial r}\left(r^2\frac{\partial v}{\partial r}\right) - \frac{2v}{r^2}\right), \quad (29)$$

$$\frac{\partial v}{\partial r} + \frac{2v}{r} = 0, \quad (30)$$

$$p_g = \frac{L_{u0}}{\pi R_s^2 \varepsilon_p^2 c}\left(\frac{R_0}{R}\right)^4, \quad (31)$$

$$p(R) - 2\mu\frac{\partial v}{\partial r}\bigg|_{r=R} = p_g\big|_{r=R}, \quad (32)$$

$$v\big|_{r=R} = \frac{dR}{dt} = \dot{R}, \quad (33)$$

where v, ρ, p, and μ are the radial velocity, density, pressure, and dynamic viscosity of the plasma, respectively; R and R_0 are the radii of the photon cavity at equilibrium and arbitrary times, respectively; p_g is the photon gas pressure in the cavity; L_{u0} is the stellar X-ray luminosity at equilibrium time; R_s is the NS radius; ε_p is the opening angle of the accretion column; and c is the speed of light.

Integrating Eqs. (29)–(33) yields

$$RR\ddot{} + \frac{3}{2}\dot{R}^2 - \frac{1}{L}(2R\dot{R}^2 + R^2\ddot{R}) + \frac{R^4\dot{R}^2}{2L^4}$$
$$= \frac{1}{\rho}\left(\frac{L_{u0}}{\pi R_s^2 \varepsilon_p^2 c}\left(\frac{R_0}{R}\right)^4 - 4\mu\frac{\dot{R}}{R} - p(L, t)\right), \quad (34)$$

where L is some distance from the cavity center, $L > R$.

Let us investigate the behavior of the photon cavity in the case of small oscillations in its radius. Assuming that $p(L, t) = p(L, t_0) = \text{const}$ and linearizing Eq. (34), we derive an expression for the square of the (cyclic) frequency of free linear oscillations:

$$\omega^2 = \frac{4L_{u0}}{\pi\rho R_0^2 R_s^2 \varepsilon_p^2 c}\left(1 - \frac{R_0}{L}\right)^{-1}. \quad (35)$$

Assuming that $\frac{R_0}{L} \ll 1$ and using Eq. (35), we can write the following relation for the oscillation period of the photon cavity:

$$T = \frac{2\pi}{\omega} = \pi R_0 R_s \varepsilon_p \sqrt{\frac{\pi\rho c}{L_{u0}}}. \quad (36)$$

Let us estimate the period and frequency of the linear oscillations. Substituting $R_s = 10^6$ cm, $R_0 = 10^4$ cm, $\varepsilon_p = 0.1$, $c = 3 \times 10^{10}$ cm s^{-1}, $L_{u0} = 10^{36}$ erg s^{-1}, and $\rho = 0.5$ g cm^{-3} in Eq. (36) yields $T = 6.8 \times 10^{-4}$ s and $f = 1/T \approx 1470$ Hz = 1.47 kHz. This value is in good agreement with the observations.

Next, let us analyze nonlinear oscillations of the photon cavity when $p(L, t) = p(L, t_0)$. Assuming that $\frac{R_0}{L} \ll 1$, disregarding the viscosity, and integrating Eq. (34), we derive an expression for the period of nonlinear free oscillations:

$$T = 1.135\rho^{1/2}\left(\frac{L_{u0}}{\pi R_s^2 \varepsilon_p^2 c}\right)^{-5/6}$$
$$\times\left(\frac{4L_{u0}R_m^3}{3R_s^2\varepsilon_p^2 c}\left(1 + 3\left(\frac{R_0}{R_m}\right)^4\right)\right)^{1/3}, \quad (37)$$

where R_m is the maximum cavity radius. If $R_m = 2R_0 = 2 \times 10^4$ cm in Eq. (37) and if we take the remaining parameters to be the same as those in the linear case, we obtain $T \approx 8.8 \times 10^{-4}$ s and $f = 1/T \approx 1100$ Hz = 1.1 kHz, in agreement with observations.

By varying the quantities in Eqs. (36) and (37) within the admissible range, we can easily determine the period of the QPOs observed in NSs with critical (Eddington) or nearly critical X-ray luminosities. Frequencies in the range 100 Hz to 1 kHz correspond to these periods.

Thus, the photon-cavitation mechanism can describe the nonlinear X-ray QPOs in neutron stars with frequencies from 100 Hz to $\gtrsim 1$ kHz.

NONLINEAR OSCILLATIONS OF CURRENT SHEETS IN ACCRETED PLASMA

Nonlinear oscillations of the current sheets that form in plasma with a magnetic field are another possible mechanism for the generation of QPOs. As applied to the solar plasma, this mechanism was considered in detail by Sakai *et al.* (1987). The formation of current sheets in plasma has been studied extensively; these studies were pioneered by Syrovatskiĭ (1976, 1977, 1978). Litvinenko (1999) considered the formation of a current sheet by taking into account the plasma flow speed in its formation region.

Apart from the solar plasma, astrophysical objects for the application of the current-sheet formation theory can be accretion disks around compact stars: white dwarfs, neutron stars, and black holes. Gnedin *et al.* (1999) proposed the mechanism of nonlinear oscillations of the current sheet that forms in a magnetic driven disk (Armitage *et al.* 1996) as an explanation of the QPOs observed in cataclysmic variables.

The equation for the oscillations of a current sheet is (Sakai *et al.* 1987)

$$\ddot{a} = \frac{c_s^2}{la^\gamma} - \frac{v_a^2}{l^2 a^2}, \qquad (38)$$

where $a = a(t)$ is the current-sheet thickness; c_s is the speed of sound; l is the scale length of the current sheet; $v_a = \dfrac{B}{\sqrt{4\pi\rho}}$ is the Alfvén velocity; and B and ρ are the magnetic induction and density in the accretion disk or column, respectively. The formula for the oscillation period can be written as

$$P = \frac{2\pi v_a^2}{E_0^{3/2} l^2}, \qquad (39)$$

where $E = \dot{a}_0^2 - \dfrac{2 v_a^2}{la_0} + \dfrac{c_s^2}{l^2 a_0^2}$. The minimum oscillation period is defined as

$$P_{min} = 2\pi\beta^{3/2}\tau_a, \qquad (40)$$

where $\tau_a = \dfrac{l}{v_a}$, $\beta = \dfrac{c_s^2}{v_a^2}$.

Transforming Eq. (40) and assuming that $c_s^2 = \dfrac{nkT}{\rho}$, where n, T, and ρ are, respectively, the particle number density, temperature, and density of the plasma in the accretion disk or column and k is the Boltzmann con-

stant, we derive an expression for the minimum oscillation period:

$$P_{min} \approx 7.44 \times 10^{14} \frac{lT^{3/2}\rho^2}{B^4}. \qquad (41)$$

Let us estimate the oscillation period using Eq. (41) for an accretion disk around a white dwarf in a close binary. We take the accretion-disk thickness as the scale length of the current sheet. Substituting $l = 10^9$ cm, $T = 10^4$ K, $\rho = 10^{-6}$ g cm^{-3}, and $B = 10^4$ G in Eq. (41) yields $P_{min} \approx 74.7$ s, which is in agreement with the observations. By varying the parameters in Eq. (41) within the admissible range, we find that the oscillation periods change from several seconds to hundreds of seconds or more. Consequently, the nonlinear oscillations of current sheets in the accretion disk closely correspond to the QPOs with periods of seconds-hundreds of seconds or more observed in cataclysmic variables and low-mass X-ray binaries.

THE BEHAVIOR OF MAGNETIZED AND LIGHT CAVITIES IN AN EXTERNAL OSCILLATION FIELD. THE DEPENDENCE OF QPO PERIOD AND AMPLITUDE ON RADIATION ENERGY

Under an externally applied acoustic pressure, a bubble of gas (for example, air) in a fluid can make forced oscillations and even collapse. The bubble collapse is caused by the shock waves that are generated in the gas through surface-oscillation instability. This instability can grow because the amplitude of the external pressure P_a can exceed a stability limit and because there is a resonance between the frequencies of the natural oscillations of the bubble and the external acoustic pressure. The resonance amplitude is given by (Krasil'nikov and Krylov 1984)

$$A = \frac{P_a/\rho\omega^2 R_0}{\omega_0^2/\omega^2 - 1 - i\delta}, \qquad (42)$$

where ω_0 is the frequency of the natural oscillations ($\omega_0 \approx \omega_{QPO}$), ω is the frequency of the external force, and δ is the parameter that describes the oscillation damping.

Two important special cases follow from Eq. (42): $\omega \gg \omega_0$ and $\omega \ll \omega_0$. In the former case, the amplitude of the forced oscillations is $A = -P_a/\rho\omega^2 R_0$; i.e., it depends only on the frequency of the external acoustic pressure. In the latter case, $A = P_a/\rho\omega^2 R_0$; i.e., it depends only of the frequency of the natural oscillations.

In the theory of spherically symmetric accretion, $\rho \sim \dot{M}^{10/7}/H_s^{3/7}$. According to Eq. (26), $\omega_0 \equiv \omega_{QPO} \sim \dot{M}^{3/7} M_s^{5/7}/H_s^{6/7} \sim L_X^{3/7} M_s^{5/7}/H_s^{6/7}$. Therefore, the amplitude of the forced oscillations depends on X-ray luminosity and NS surface magnetic field strength as follows:

$$A \sim \frac{P_a}{\omega^2 L_X^{8/7} H_s^{1/7}}, \quad \omega \gg \omega_0, \qquad (43)$$

$$A \sim \frac{H_s^{11/7} P_a}{L_X^2}, \quad \omega \ll \omega_0. \qquad (44)$$

Let us now compare the derived dependences of QPO frequency ω_{QPO} and amplitude A with the observations. Observations reveal a complex pattern of the dependence of QPO frequency and amplitude on X-ray flux. Yu *et al.* (1999) showed that the characteristic QPO frequencies correlate with the X-ray photon count rate (Ford *et al.* 1997). Thus, for example, during an outburst of the X-ray binary Aquila X-1, the QPO frequency in the spectral range 2–10 keV actually decreased from 813 ± 3 to 776 ± 4 Hz, while the X-ray flux decreased by 10%. On the other hand, Mendez *et al.* (2000) showed that for some sources, this correlation is preserved only for a relatively short time interval, no more than one day. If, however, QPOs are observed on a longer time scale (for example, several days), then this correlation with the photon count rate virtually disappears. At the same time, the QPO frequencies turn out to correlate more strongly with the spectral behavior of the X-ray source. For short intervals, Ford *et al.* (1997) deduced the following slope of the correlation between QPO frequency and blackbody flux: $d\log\omega/d\log F_{BB} = 0.27$–$0.37$. The last value (0.37) is in reasonable agreement with the theoretical value of 3/7, which follows from Eq. (26). The agreement can be further improved by using the results of Toropin *et al.* (1998), who solved the self-consistent problem of spherically symmetric accretion by taking into account a change in the magnetospheric configuration under the effect of the accreted flow. As a result, they obtained the following relation between X-ray luminosity and accretion rate: $\dot{M} \sim L_X^{2/3}$. Instead of Eqs. (26) and (28), we then have

$$\omega_{QPO} \sim L_X^{0.3}, \qquad (45)$$

$$\omega_{QPO} \sim L_X^{0.33}, \qquad (46)$$

respectively.

Thus, the natural oscillations actually correlate with the X-ray flux. The lack of correlation on long time scales could be explained by such a change of the magnetospheric oscillation modes for which forced oscillations would take place in the magnetosphere under the external acoustic pressure P_a; the frequency of the latter ω may not be directly related to the accretion rate $\dot{M}$ and, hence, to the X-ray flux. In any case, this situation deserves a more detailed analysis.

Let us now discuss the dependence of QPO amplitude on photon energy. Eqs. (43) and (44) can be used to obtain a rough estimate. The pattern of this dependence is difficult to determine unambiguously, because

we do not know *a priori* the dependence of the oscillation amplitude of external pressure P_a on accretion parameters, in particular, on luminosity L_X. Therefore, more likely, the inverse problem of determining the dependence of the amplitude of external pressure on these parameters can be solved by comparing the theoretical relations (43) and (44) with observational data. Observations of the low-mass X-ray binary 4U 1820-30 (Wijnands *et al.* 1999) revealed that the QPO amplitude increased with photon energy. This dependence does not follow directly from Eqs. (42)–(46), because, according to these formulas, the frequency of the natural magnetospheric oscillations and the QPO amplitude depend on the total X-ray luminosity rather than on the differential (in energy) X-ray flux. These formulas describe oscillations of the Alfvén surface itself. The amplitude of the oscillations can decrease due to their damping through heat conduction and accreted-plasma viscosity, as well as through acoustic losses and other dissipative processes. In general, the dependence of damping parameter δ on the transport coefficients is complex. This parameter can be estimated by using Eqs. (2.15)–(2.23) from Krasil'nikov and Krylov (1984). When the effect of viscosity is strongest compared to other dissipative factors, $\delta \sim \nu$, where ν is the coefficient of kinematical viscosity. As the NS surface is approached, the accreted-plasma temperature increases (Lipunov 1987). The viscosity of plasma moving along magnetic field lines, as, for example, in an accretion column, is known (Spitzer 1965) to increase with temperature, and, hence, the damping will be stronger. This is also characteristic of plasma with a dominant radiation pressure. Thus, the smaller the distance to the NS is, the larger the plasma viscosity is and, hence, the larger is the damping parameter and the smaller is the oscillation amplitude. Since soft and hard photons are generated mostly in the upper part of the column and near its base, respectively, the oscillation amplitude of the magnetospheric region where the hard photons are produced is smaller than that of the region where the soft photons are produced. Of course, all this reasoning is qualitative in nature. The actual situation is more complex and requires a further quantitative analysis.

In conclusion, let us briefly discuss the situation with a QPO lag in the soft and hard X-ray bands. Ford *et al.* (1999) detected a lag between 9–33 and 2–9 keV photons. This lag is in good agreement with the magnetocavitation mechanism of QPOs. According to this mechanism, the oscillatory process initially develops in the NS magnetosphere and in the upper part of its accretion column and then at the column base, where the hardest photons are generated. Ford *et al.* (1997) also showed that the rms amplitude of the high-frequency QPOs for 4U 0614 + 091 increased with energy from $6.8 \pm 1.5\%$ (3–5 keV) to $21.3 \pm 4\%$ (10–12 keV). This increase can be explained by angular divergence of the accretion column, as implied by Eq. (15).

According to the photon-cavitation mechanism, more likely, one might expect a QPO lag of the soft

X-ray flux relative to the harder photons. The point is that photon bubbles are more efficiently formed at the very base of the accretion column where the harder NS X-ray component originates. Soft X-ray QPOs are produced either through the direct Compton scattering of hard photons by electrons in the upper part of the column or during the rise of photon bubbles followed by their adiabatic cooling.

Of great interest is the situation with a QPO lag between photons at different energies when QPOs are generated by nonlinear oscillations of current sheets in accreted plasma. This lag depends significantly on the speed of plasma inflow into the neutral sheet between the magnetic fields of opposite polarity, where the currents are produced (Litvinenko 1999):

$$v = c\sqrt{\frac{v_a}{4\pi\Lambda\sigma}}\left(1 + \frac{B^2}{8\pi kNT}\right)^{1/4}, \qquad (47)$$

where σ is the plasma conductivity and N is the plasma ion density. Depending on the accretion-disk model, the plasma flow speed changes significantly with distance from the compact star; this change is not monotonic (Litvinenko 1999) and can easily produce the observed QPO lag for photons at different energies. A more detailed analysis of the QPO mechanism attributable to the formation of current sheets in accretion disks around black holes is planned in a special paper.

CONCLUSION

The diversity of physical parameters and peculiarities of QPOs in close binaries with accretion suggests that there can be various physical mechanisms of the QPOs, so different physical mechanisms can operate in different close binaries. At present, none of the numerous QPO mechanisms considered in the literature can account for the entire set of observational data.

We have considered three new QPO mechanisms, which we called magnetocavitation, photon-cavitation, and the mechanism of nonlinear current-sheet oscillations. The first two mechanisms are based on the standard cavitation process: the formation of gaseous bubbles (or cavities) in a fluid and oscillations of their surfaces. The oscillations of the bubble surfaces are both linear and nonlinear. For the magnetocavitation mechanism, an analog of a gaseous bubble in a fluid is the NS magnetosphere, while the photon-cavitation mechanism considers photon-gas-filled bubbles, which are formed in the accretion column during super-Eddington accretion (Arons 1992). We solved the equations for nonlinear oscillations of the surfaces of magnetized gaseous (Alfvén surface) and photon cavities. The calculated characteristic oscillation frequencies of the magnetosphere and the photon cavities, as well as the dependences of oscillation frequency and amplitude on X-ray photon energy and on QPO time lag between photons at different energies are in good agreement with observational data.

REFERENCES

1. M. A. Alpar and J. Shaham, IAU Circ., No. 4046 (1985a).
2. M. A. Alpar and J. Shaham, Nature **316**, 239 (1985b).
3. P. J. Armitage, M. Livio, and J. E. Pringle, Astrophys. J. **457**, 332 (1996).
4. J. Arons, Astrophys. J. **388**, 561 (1992).
5. J. Arons and R. Klein, Astrophys. J. **312**, 666 (1987).
6. M. Berger, M. van der Klis, W. H. G. Lewin, *et al.*, Astrophys. J. Lett. **469**, L13 (1996).
7. H. V. Bradt, astro-ph/9901174 (1999).
8. S. Campana, M. Colpi, S. Mereghetti, *et al.*, Astron. Astrophys. Rev. **8**, 279 (1998).
9. F. A. Cordova and K. O. Mason, in *Accretion Driven Stellar X-ray Sources,* Ed. by W. H. G. Lewin and E. P. J. van den Heuvel (Cambridge Univ. Press, Cambridge, 1983), p. 147.
10. E. Ford, P. Kaaret, K. Chen, *et al.*, Astrophys. J. Lett. **486**, L47 (1997).
11. E. C. Ford, M. van der Klis, M. Mendez, *et al.*, Astrophys. J. Lett. **512**, L31 (1999).
12. P. Ghosh and F. K. Lamb, in *X-ray Binaries and Recycled Pulsars,* Ed. by E. P. J. van den Heuvel and S. A. Rappaport (Kluwer, Dordrecht, 1992), p. 487.
13. Yu. N. Gnedin, Yu. A. Nagovitsyn, and T. M. Natsvlishvili, Astron. Zh. **76**, 532 (1999) [Astron. Rep. **43**, 462 (1999)].
14. G. Hasinger, A. Langmeier, W. Pietsch, *et al.*, Space Sci. Rev. **40**, 233 (1985).
15. G. Hasinger, A. Langmeier, M. Sztajno, *et al.*, Nature **319**, 469 (1986).
16. J. J. L. Hsu, J. Arons, and R. I. Klein, Astrophys. J. **478**, 663 (1997).
17. P. Kaaret, E. C. Ford, and K. Chen, Astrophys. J. Lett. **480**, L27 (1997).
18. P. Kaaret, S. Piraino, E. C. Ford, *et al.*, Astrophys. J. Lett. **514**, L31 (1999).
19. R. I. Klein, J. Arons, G. Jernigan, *et al.*, Astrophys. J. Lett. **457**, L85 (1996a).
20. R. I. Klein, G. Jernigan, J. Arons, *et al.*, Astrophys. J. Lett. **469**, L119 (1996b).
21. M. van der Klis, Preprint No. 105, EXOSAT (1989).
22. M. van der Klis and F. Jansen, in *The Evolution of Galactic X-ray Binaries*, Ed. by J. Trumper, W. H. G. Lewin, and W. Brinkmann; NATO ASI Ser. **167**, 129 (1986).
23. M. van der Klis, F. Jansen, J. van Paradijs, *et al.*, IAU Circ., No. 4043 (1985a).
24. M. van der Klis, F. Jansen, J. van Paradijs, *et al.*, Nature **316**, 225 (1985b).
25. M. van der Klis, F. Jansen, N. E. White, *et al.*, IAU Circ., No. 4068 (1985c).

26. M. van der Klis, L. Stella, N. E. White, *et al.*, Astrophys. J. **316**, 411 (1987).

27. M. van der Klis, J. H. Swank, W. Zhang, *et al.*, Astrophys. J. Lett. **469**, L1 (1996a).

28. M. van der Klis, J. van Paradijs, W. H. G. Lewin, *et al.*, IAU Circ., No. 6428 (1996b).

29. M. van der Klis, A. D. Wijnands, K. Horne, *et al.*, IAU Circ., No. 6511 (1996c).

30. R. T. Knapp, J. W. Daily, and F. G. Hammitt, *Cavitation* (McGraw-Hill, New York, 1970; Mir, Moscow, 1974).

31. V. A. Krasil'nikov and V. V. Krylov, *Introduction to Physical Acoustics* (Nauka, Moscow, 1984).

32. L. D. Landau and E. M. Lifshitz, *Course of Theoretical Physics*, Vol. 6: *Fluid Mechanics* (Nauka, Moscow, 1988; Pergamon, New York, 1987).

33. L. D. Landau and E. M. Lifshitz, *Course of Theoretical Physics*, Vol. 8: *Electrodynamics of Continuous Media* (Nauka, Moscow, 1992; Pergamon, New York, 1984).

34. L. D. Landau and E. M. Lifshitz, *Statistical Physics* (Nauka, Moscow, 1995; Pergamon, Oxford, 1980), Vol. 1.

35. W. H. G. Lewin, J. van Paradijs, G. Hasinger, *et al.*, Mon. Not. R. Astron. Soc. **226**, 383 (1987).

36. V. M. Lipunov, *Astrophysics of Neutron Stars* (Nauka, Moscow, 1987).

37. Yu. E. Litvinenko, Astrophys. J. **515**, 435 (1999).

38. M. Matsuoka, in *Cataclysmic Variables and Low-Mass X-ray Binaries*, Ed. by D. Q. Lamb and J. Patterson (Reidel, Dordrecht, 1985), p. 139.

39. C. W. Mauche, in *Astrophysics in the Extreme Ultraviolet*, Ed. by S. Bowyer and R. F. Malina (Kluwer, Dordrecht, 1996), p. 317.

40. M. Mendez, M. van der Klis, and E. C. Ford, astro-ph/0006245 (2000).

41. E. A. Neppiras, Phys. Rep. **61**, 159 (1980).

42. J. Patterson, Astrophys. J., Suppl. Ser. **45**, 517 (1981).

43. E. L. Robinson and R. E. Nather, Astrophys. J., Suppl. Ser. **39**, 461 (1979).

44. J. Sakai, A. Colin, and E. Priest, Sol. Phys. **114**, 253 (1987).

45. A. P. Smale, W. Zhang, and N. E. White, IAU Circ., No. 6507 (1996).

46. L. Spitzer, *Physics of Fully Ionized Gases* (Interscience, New York, 1962; Mir, Moscow, 1965).

47. T. E. Strohmayer, W. Zhang, J. H. Swank, *et al.*, Astrophys. J. Lett. **469**, L5 (1996).

48. S. I. Syrovatskiĭ, Pis'ma Astron. Zh. **2**, 35 (1976) [Sov. Astron. Lett. **2**, 13 (1976)].

49. S. I. Syrovatskiĭ, Pis'ma Astron. Zh. **3**, 133 (1977) [Sov. Astron. Lett. **3**, 69 (1977)].

50. S. I. Syrovatskiĭ, Astrophys. Space Sci. **56**, 3 (1978).

51. L. Titarchuk, I. Lapidus, and A. Muslimov, Astrophys. J. **499**, 315 (1998).

52. Yu. M. Toropin, O. D. Toropina, V. V. Savelyev, *et al.*, astro-ph/9811272 (1998).

53. B. A. Vaughan, M. van der Klis, M. Mendez, *et al.*, Astrophys. J. Lett. **483**, L115 (1997).

54. B. Warner, *Cataclysmic Variable Stars* (Cambridge Univ. Press, Cambridge, 1995).

55. B. Warner, Mon. Not. R. Astron. Soc. **227**, 23 (1987).

56. R. Wijnands, M. van der Klis, J. van Paradijs, *et al.*, IAU Circ., No. 6447 (1996).

57. R. Wijnands, M. van der Klis, and E.-J. Rijkhost, Astrophys. J. Lett. **512**, L39 (1999).

58. W. Yu, T. P. Li, W. Zhang, *et al.*, Astrophys. J. Lett. **512**, L35 (1999).

Translated by V. Astakhov

A Photometric Study of BQ Camelopardalis, an Optical Counterpart of the X-ray Source V0332+53

V. P. Goranskiĭ*

Sternberg Astronomical Institute, Universitetskiĭ pr. 13, Moscow, 119899 Russia
Received January 15, 2001

Abstract—Eighteen-year-long photometric *B, V,* and *R* observations (1983–2000) have revealed variability of the light from BQ Cam with a $0\overset{m}{.}6$ amplitude. During the first half of this time interval, we observed two brightening cycles with cycle duration of 1600 days. Such brightenings usually occur in Be stars and are attributable to shell episodes. The shorter X-ray outbursts in 1983 and 1989 coincide with the maxima of these cycles. During the second half of the observing interval, the object was faint; its brightness gradually increased, and no X-ray outbursts were observed. In quiescence, variability was detected on a time scale of several days with an amplitude no larger than $0\overset{m}{.}15V$, which does not depend on orbital phase. © *2001 MAIK "Nauka/Interperiodica".*

Key words: *X-ray and gamma-ray sources; pulsars, neutron stars, and black holes*

INTRODUCTION

The X-ray transient V0332+53 was discovered by the Vela 5B satellite during its strong outburst that began on June 1, 1973 (Heintz *et al.* 1973). It had been seen for three months and reached 1.6 Crab in the range 3–12 keV at maximum brightness (Terrell and Predhorsky 1985; Whitlock 1989). At that time, the source was not identified with any optical object. Its spectrum was unusually hard, with the index $\alpha = 1.0 \pm 0.2$. Rapid fluctuations in X-ray flux were observed. The 1973 outburst exhibited a slow rise and a symmetric slow decline. During the second X-ray outburst detected by the Tenma satellite (Tanaka 1983), which began on November 14, 1983, the object was identified with a faint ($m_{pg} = 16\overset{m}{.}5$) star with the H_α emission line in its spectrum with a blue continuum and a large interstellar reddening (Argyle 1983; Bernacca *et al.* 1983; Kodaira 1983). In the USNO A1.0 Catalog, the star has the coordinates $3^h34^m59\overset{s}{.}929$ and $+53°10'23''.89$ (2000). The X-ray outburst of 1983–1984 was a series of four short outbursts during three months; at the peak of its brightest outburst, the object was considerably fainter than during the 1973 outburst, a mere 0.06 Crab. During the second outburst, pulsations were detected from the X-ray source with a 4.4-s period; the pulsation period varied, suggesting the pulsar's motion in an elliptical orbit with a period of 34.2 days. The results of the Tenma study of the object are presented in Makeshima *et al.* (1990). The third known outburst occurred in September 1989 and was detected by the Ginga satellite

(Takeshima *et al.* 1994). Observations confirmed the pulsation period and its variations.

Thus, X-ray observations have revealed that the object is a binary system consisting of a Be star and a neutron star, a pulsar. Analogs of V0332+53 are the systems 4U 0115+63, A 0535+26, A 0538-66, or X 1538-522; the latter is known as an eclipsing system (Corbet *et al.* 1993). The orbital period of V0332+53 was determined from the Doppler shift of pulses in the source. Based on the EXOSAT observations from November 20, 1983, until January 23, 1984, White *et al.* (1984) and Stella *et al.* (1985) gave the following orbital elements of the pulsar: $P_{orb} = 34\overset{d}{.}25$, $e = 0.31 \pm 0.03$, $\omega = 313° \pm 10°$ (periastron longitude), $a_x \sin i = 48 \pm 4$ light seconds, and $f(M) \approx 0.1 M_\odot$. The time of periastron passage is JD $2\,445\,652 \pm 1^d$. All outbursts occurred near the periastron passage. In addition to X-ray pulsations, quasi-periodic oscillations (QPOs) with the frequency $f = (5.1 \pm 0.5) \times 10^{-2}$ Hz and an amplitude of $4.8 \pm 1.2\%$ were detected (Takeshima *et al.* 1994). The distance to the object is estimated to be 2.2–5.8 kpc.

A reanalysis of the 1973 observations of Vela 5B also revealed pulsations with a period of $4\overset{s}{.}3753$ and a modulation of the X-ray flux with possible periods of 34.38 ± 0.02 or 34.07 ± 0.02 days (Whitlock 1989), which confirms the identification of the source of the 1973 outburst and the source of the subsequent outbursts in 1983 and 1989. These observations yielded another time of periastron passage, JD $2\,441\,870.0 \pm 1.0$.

Pulsations with a period half that in X rays, $2\overset{s}{.}198$, were detected in the optical range (Bernacca *et al.* 1984). Within three years after the outburst, the H_α

* E-mail address for contacts: goray@sai.msu.ru

Table 1. A log of observations

Observatory	Observing season	Instrumentation, photographic emulsions, filters	Telescopes
Crimean Station of SAI	1983–1990	*V*: Kodak 103aD, A-600 + ZhS-17	50-cm Maksutov (AZT-5)
SAI, Moscow		*B*: Kodak 103aO, ORWO ZU-21 + BS-8	70-cm Cassegrain (AZT-2)
Tien Shan Observatory	1993–1996	*WBVR* photometers with filters	100-cm Cassegrain (Zeiss)
Crimean Station of SAI	1998–2000	SBIG ST-6	120-cm Cassegrain (ZTE)
SAI, Moscow		SBIG ST-7 CCDs (with *BVRI* filters)	70-cm Cassegrain (AZT-2)
			60-cm Cassegrain (Zeiss)
Crimean Astrophysical Observatory		SBIG ST-7 CCD (with *VRI* filters)	38-cm Cassegrain*

* The Cassegrain telescope produced by G. Borisov (Crimean Station of SAI).

emission weakened, which was accompanied by a fading in the infrared *JHKL* bands by several tenths of a magnitude (Coe *et al.* 1987). The infrared data contain a spectral component that belongs to the circumstellar gas envelope; this component can be separated from the light of the B star and shows slow variations on a time scale of years. According to Iye and Kodaira (1985), the October 1984 and March 1985 observations revealed a weakening of the hydrogen emission by a factor of 4 compared to November 1983 near the peak of the X-ray outburst. Eventually, manifestations of infrared photometric variability and optical pulsations became the reason why the object was included in the General Catalog of Variable Stars under the name BQ Cam, though the study by Fuhrman (1985) based on 55 Sonneberg plates of 1939–1984 showed that the star was constant ($16^m.6 \pm 0^m.2$ pg).

We began our photographic observations of BQ Cam in 1983 before the object was identified optically using its approximate X-ray coordinates kindly provided by R.A. Sunyaev and V. M. Lyuty. Subsequently, we had continued the observations for the following 17 years by all the available methods: photography, photoelectric photometry, and CCD photometry.

OBSERVATIONS

The observations were carried out at several observatories with different telescopes and equipment and with filters that approximated Morgan–Johnson's photometric *B*, *V*, and *R* bands. Information about the photographic, photoelectric, and CCD observations is presented in Table 1. The main problem was to allow for systematic differences between the three different kinds of observations. During the first years of observations, there was no photometric standard in the region of BQ Cam to calibrate the photographic observations. We first obtained a primary photographic standard near the star by transferring a photoelectric standard located at a distance of 10°. This method is inaccurate and subject to systematic errors, but, nevertheless, it allows a nearly linear magnitude scale to be constructed. All photographic measurements were made with the iris photometer of the Sternberg Astronomical Institute rel-

ative to the primary standard. Subsequently, when we had an opportunity, we measured the primary standard stars with the *WBVR* photometer designed by Kornilov and Krylov (1990) using the 1-m Zeiss reflector of the Tien Shan Astronomical Observatory. Given the photoelectric magnitudes of the primary standard stars, it was easy to reduce the photographic observations to the photoelectric scale. Subsequently, the photoelectric magnitudes were used during our CCD observations.

Table 2 contains the photoelectric magnitudes of six primary standard stars, their coordinates, and magnitudes from the USNO 1.0 Catalog. The last two rows of Table 2 give data on the comparison star *c* = GSC 3716.460 and the check star *k* = GSC 3716.166, which were used in the photoelectric photometry. The stability of the comparison and check stars was firmly established during the observations. A comparison of our photoelectric magnitudes and the USNO magnitudes is of interest not only in that it gives an idea of the systematic errors of the USNO photometry, but also in that it allows us to calibrate the measurement of BQ Cam at the old epoch of the POSS *R* and *B* plates:

September 27/28, 1954, 17.0*B* 14.2*R*.

The photographic *B* observations with the 70-cm AZT-2 reflector have the lowest accuracy, $0^m.2$. This is because the star is faint and the sky background is bright in Moscow. Other photographic observations

Table 2. Accurate coordinates and photometric magnitudes of the comparison stars

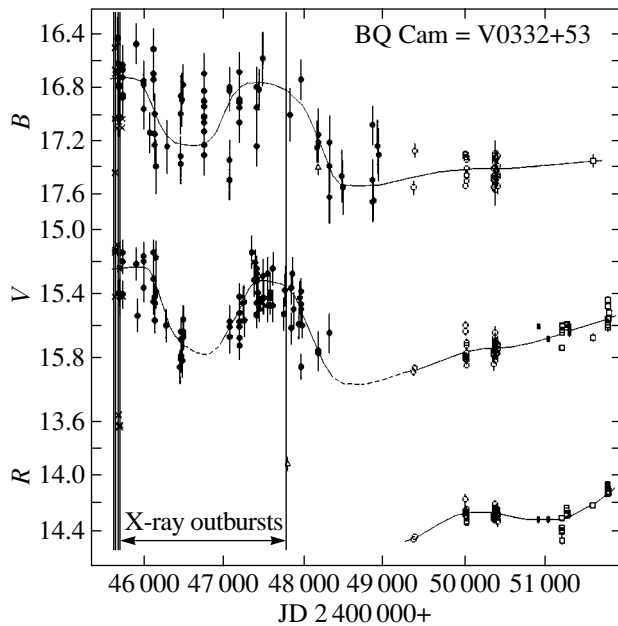| *	α (2000)	δ (2000)	US-NO *B*	US-NO *R*	*B*	*V*	*R*
1	3ʰ35ᵐ03ˢ.7	+53°12′09″	15.3	13.1	–	–	–
2	3 34 52.9	+53 11 54	16.7	13.8	16.32	14.81	13.80
3	3 34 40.9	+53 08 36	17.0	13.9	16.80	15.16	13.80
4	3 34 48.8	+53 09 33	17.7	15.1	17.17	15.79	14.82
5	3 34 36.6	+53 10 24	17.2	14.7	17.01	15.60	14.44
6	3 34 29.9	+53 09 11	16.8	14.4	16.70	15.37	14.38
c	3 35 34.9	+53 12 56	13.4	11.5	13.16	12.07	11.17
k	3 35 29.8	+53 14 55	12.8	11.4	12.70	11.74	10.94

Fig. 1. *B*, *V*, and *R* light curves for the slow variability of BQ Cam. The solid line indicates variations in mean brightness level. The crosses are the data from the cited literature, and the triangles are our measurements based on the Digital Sky Survey DSS-II; the other symbols represent our photographic, photoelectric, and CCD observations. The vertical lines mark the times of the X-ray outbursts.

have a mean accuracy in the range $0\overset{m}{.}08 - 0\overset{m}{.}10$. The photoelectric *V* observations and the CCD observations have an accuracy of $0\overset{m}{.}05$ and $0\overset{m}{.}02$, respectively. The accuracy of the *R* observations is higher, about $0\overset{m}{.}01$, because the object is brighter by $1\overset{m}{.}4$ in this band; our CCD arrays are most sensitive in the red.

Based on our photoelectric observations, we determined the following color indices: $B–V = 1\overset{m}{.}67 \pm 0\overset{m}{.}02$ and $V–R = 1\overset{m}{.}48 \pm 0\overset{m}{.}02$. The ultraviolet color index is less reliable: $W–B = -0.05 \pm 0.20$. The color excess $E(B–V) = 1\overset{m}{.}8$ suggests a large interstellar absorption, $A_V \approx 5\overset{m}{.}5$. The star lies exactly on the $(B–V)–(V–R)$ sequence for normal stars and exhibits no excess in the *R* band, suggesting a small contribution of the H_α emission in this band in quiescence. The lower limit for the distance to the star (of spectral type B) is 2.9 kpc.

LIGHT CURVES

The *B*, *V*, and *R* light curves of BQ Cam are shown in Fig. 1. The times of the X-ray outbursts are also marked. The amplitude of the optical brightness variations was, on average, a mere $0\overset{m}{.}6$, which is the same as that in the infrared.

The brightness of BQ Cam during the X-ray outburst of 1983 (JD Max.X $= 2\,445\,658$) was at a maxi-

mum, on average, 15.2*V*, and then remained the same for 400 days; subsequently, it decreased to a minimum of about 15.8*V* (JD 2 446 450) in 400 days. The fading may have not been monotonic and was accompanied by brightness fluctuations with an amplitude comparable to that of the outburst. However, this conclusion is drawn from photographic observations alone, and the fluctuation amplitude only slightly exceeds the accuracy of photographic photometry. At this time, the fading was accompanied by a weakening of the H_α emission and by a fading in the infrared (Coe *et al.* 1987; Iye and Kodaira 1985). When the observations resumed after a short break, the brightness was already rising to another maximum; the maximum was reached 200 days before the X-ray outburst of 1989 (JD Max.X $=$ 2 447 788). After the outburst, the object's brightness again decreased to a minimum, and again within approximately 500 days after the outburst. The time interval between the two successive optical brightenings was 1600 days (4.4 years); the interval between the successive X-ray outbursts was 2100 days (5.8 years).

The optical brightenings are longer than the X-ray ones. Whereas the former last for several years, the latter last for several months. Note that one of the X-ray outbursts (1989) coincided with the maximum of optical brightening. To be more precise, it occurred approximately 100 days after the middle of the optical outburst. This may also be true for the X-ray outburst of 1983, because the time from the X-ray outburst until the fading to a low level was about half the duration of the next brightening cycle. It can be concluded that the X-ray outbursts took place at maximum, enhanced optical brightness of BQ Cam. However, within the error limits, the photographic observations reveal no local brightenings during the periastron passages of the neutron star with a 34^d period predicted from X-ray data.

The object has been in quiescence for the last nine years. In these years, its brightness has not been constant, but it gradually increased with an amplitude of $0\overset{m}{.}30$ in *V* and *R* (i.e., half the optical variability amplitude). No new X-ray outbursts were observed. The described brightenings were also observed in *B*; they are clearly seen in Fig. 1, despite the large scatter of our *B* observations. The behavior of BQ Cam is much the same as that of another similar system, V725 Tau (A0535+26). The latest published data on V725 Tau (Lyuty and Zaĭtseva 2000) also show a transition of the system to quiescence and no optical brightenings and X-ray outbursts. The light curves of these two objects essentially coincide.

RAPID LOW-AMPLITUDE VARIABILITY

Our analysis of the accurate photoelectric and CCD observations reveals a distinct rapid variability of BQ Cam on a time scale of several days (Fig. 2a–2d). The most accurate *R* observations are indicated here. The *V* observations show similar variations whose
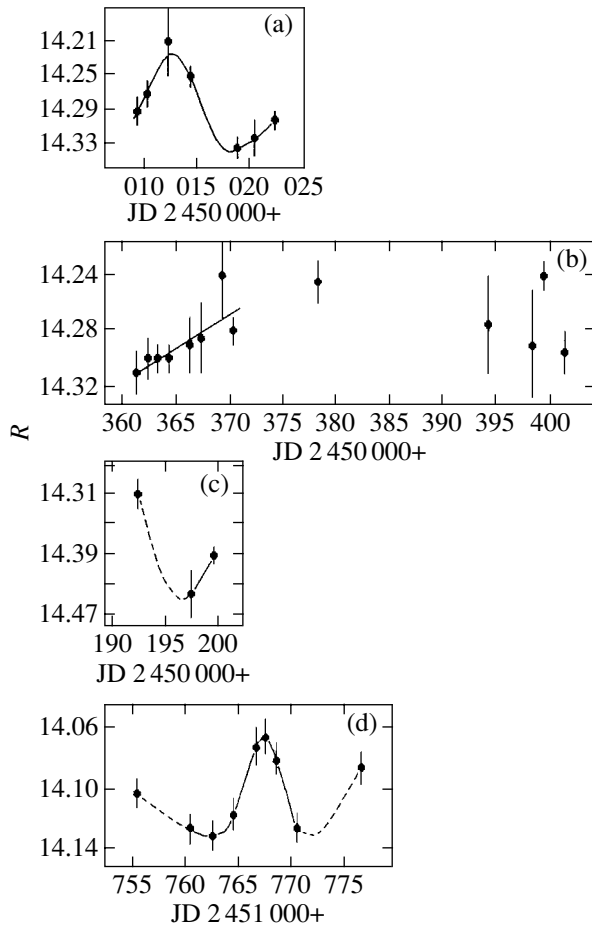
Fig. 2. R light curves for the rapid variability of BQ Cam, for several observing seasons: (a), (b) photoelectric observations and (c), (d) CCD observations. The vertical scale is different, depending on the variability amplitude.

amplitude is occasionally twice as large. The measurements in these two bands correlate. The vertical bars in Fig. 2 indicate the scatter of observations during the night (if two or more observations were made on this night) or the typical error of a single measurement.

During JD 2 450 009–2 450 022, a complete cycle of brightness variations with an amplitude of $0\overset{m}{.}13R$ and a cycle length of $\approx 13^\mathrm{d}$ (Fig. 2a) took place in BQ Cam. The same brightness variations with a factor of 2 lower amplitude are seen in Fig. 2d in the interval JD 2 451 760–2 451 771. However, during JD 2 450 361–2 450 371, a gradual brightening occurred in approximately the same time (Fig. 2b). Such modest brightness variations resemble the ellipticity effect in classical binary systems. Since the orbit of BQ Cam is highly eccentric, the wave of tidal distortion can differ greatly in shape from the classical one. However, these brightness variations show no phase dependence on the well-known orbital period of $34\overset{d}{.}25$ (Stella *et al.* 1985).

To test the hypothesis that the brightness variations on a time scale of several days correlate with orbital motion, we computed periodograms by the methods of Deeming (1975) and Lafler and Kinman (1965) using 31 nightly averaged observations. The observations were chosen by the minimum scatter and the maximum accuracy. We took into account the slow trends in the season-to-season brightness variations. The computations were performed both near the well-known orbital period of 34^d and in a wider range (5–1000^d). The best period was $10\overset{d}{.}44$, which was in conflict with the X-ray data. Near the well-known period, the preferred value was found to be $36\overset{d}{.}83$. The two periods are represented by a single wave in the light curve. However, the significance levels of these light curves are very low because of the small number of observations, and the light curves exhibit a considerable scatter. Thus, the hypothesis of the 34-day (or close) orbital period is not confirmed photometrically.

CONCLUSION

Based on the 18-year-long optical observations of BQ Cam (V0332+53), we have determined the variability amplitude in B, V, and R, $0\overset{m}{.}6$, which is the same as the infrared variability amplitude. Two brightenings 3 years in duration following with an interval of 4.4 year dominate in the light curves. The X-ray outbursts coincided with the maximum optical brightness, but they were considerably shorter in duration. The X-ray flux is known to be modulated with the orbital period; it increases when the neutron star passes through the periastron of its elliptical orbit. At the same time, the brightenings of Be stars are known to be related to the ejection of circumstellar shells whose emergence causes the hydrogen emission to strengthen. Precisely this shell episode was observed in BQ Cam. It is unclear, however, why the emergence of a circumstellar shell does not immediately leads to an X-ray outburst, and it occurs with a delay of several hundred days.

It may well be that the formation of an accretion disk near the neutron star and the accumulation of matter in the disk, which is enhanced when the circumstellar shell appears, is responsible for this delay, while the X-ray outburst is the result of disk instability. During an X-ray outburst, the disk is destroyed, as in other transient sources, for example, CI Cam or V4641 Sgr, and the new disk is accumulated more slowly. Thus, the periodicity of X-ray outbursts roughly coincides with the periodicity of shell episodes, but the duration of the former is shorter than that of the latter. The accretion disk instability may also be due to the periastron passage by the neutron star, which causes the X-ray flux to be modulated during outbursts. We have also detected more rapid brightness variations on a time scale of several days whose correlation with the orbital motion is not confirmed.

ACKNOWLEDGMENTS

REFERENCES

1. R. W. Argyle, IAU Circ., No. 3897 (1983).
2. P. L. Bernacca, T. Iijima, and R. Stagni, IAU Circ., No. 3897 (1983).
3. P. L. Bernacca, T. Iijima, and R. Stagni, Astron. Astrophys. **132**, L8 (1984).
4. P. W. J. L. Brand, T. R. Geballe, and M. P. Toner, IAU Circ., No. 3893 (1983).
5. M. J. Coe, A. J. Longmore, B. J. Paygne, and C. G. Hanson, Mon. Not. R. Astron. Soc. **226**, 455 (1987).
6. R. H. D. Corbet, J. W. Woo, and F. Nagase, Astron. Astrophys. **276**, 52 (1993).
7. T. J. Deeming, Astrophys. Space Sci. **36**, 137 (1975).
8. C. Heintz, H. Bradt, G. Clark, *et al.,* IAU Circ., No. 2540 (1973).
9. M. Iye and K. Kodaira, Publ. Astron. Soc. Pac. **97**, 1186 (1985).
10. K. Kodaira, IAU Circ., No. 3897 (1983).
11. V. G. Kornilov and A. V. Krylov, Astron. Zh. **67**, 173 (1990) [Sov. Astron. **34**, 90 (1990)].
12. J. Lafler and T. D. Kinman, Astrophys. J., Suppl. Ser. **11**, 216 (1965).
13. V. M. Lyuty and G. V. Zaĭtseva, Pis'ma Astron. Zh. **26**, 13 (2000) [Astron. Lett. **26**, 9 (2000)].
14. K. Makeshima, T. Ohashi, N. Kawai, *et al.*, Publ. Astron. Soc. Jpn. **42**, 295 (1990).
15. J. Terrell and W.C. Predhorsky, Astrophys. J. Lett. **285**, L15 (1985).

Translated by N. Samus'

Periodic Pattern in the Residual-Velocity Field of OB Associations

A. M. Mel'nik*, A. K. Dambis, and A. S. Rastorguev

Sternberg Astronomical Institute, Universitetskiĭ pr. 13, Moscow, 119899 Russia
Received October 23, 2000; in final form, January 25, 2001

Abstract—An analysis of the residual-velocity field of OB associations within 3 kpc of the Sun has revealed periodic variations in the radial residual velocities along the Galactic radius vector with a typical scale length of $\lambda = 2.0 \pm 0.2$ kpc and a mean amplitude of $f_R = 7 \pm 1$ km s^{-1}. The fact that the radial residual velocities of almost all OB associations in rich stellar-gas complexes are directed toward the Galactic center suggests that the solar neighborhood under consideration is within the corotation radius. The azimuthal-velocity field exhibits a distinct periodic pattern in the $0° < l < 180°$ region, where the mean azimuthal-velocity amplitude is $f_\theta = 6 \pm 2$ km s^{-1}. There is no periodic pattern of the azimuthal-velocity field in the $180° < l < 360°$ region. The locations of the Cygnus arm, as well as the Perseus arm, inferred from an analysis of the radial- and azimuthal-velocity fields coincide. The periodic patterns of the residual-velocity fields of Cepheids and OB associations share many common features. © *2001 MAIK "Nauka/Interperiodica"*.

Key words: *star clusters and associations, stellar dynamics, kinematics; Galaxy (Milky Way), spiral pattern*

1. INTRODUCTION

The location of the spiral arms in our Galaxy and their influence on the kinematics of gas and young stars is undoubtedly of great importance for understanding the large-scale hydrodynamic processes and the evolution of stellar groupings and that of the Galaxy as a whole. Only in our own Galaxy it is possible to derive the space velocity field of young stars and analyze the radial and azimuthal velocity components simultaneously. However, even now the location of spiral arms in the Galaxy remains a subject of discussion. There are two main approaches to the problem. The first one consists in identifying spiral arms from regions of enhanced density of young objects in the galactic disk (Morgan *et al.* 1952; Fenkart and Binggeli 1979; Humphreys 1979; Efremov 1998; Berdnikov and Chernin 1999, and others). The main idea of the second approach is to look for telltale kinematical signatures of spiral arms (Burton 1971; Burton and Bania 1974; Creze and Mennessier 1973; Gerasimenko 1993; Mishurov *et al.* 1979, 1997; Mel'nik *et al.* 1998, 1999; Sitnik and Mel'nik 1999; Sitnik *et al.* 2001, and others). We consider the latter approach to be more promising, because kinematical analyses can be performed on incomplete samples, whereas when comparing stellar space densities in different regions of the Galaxy, it is necessary to allow for observational selection, which is a very difficult problem.

However, when performing kinematical analyses, one is up against another problem. Almost all stars with known line-of-sight velocities and proper motions are located within 3 kpc of the Sun, with the kinematical data becoming extremely scarce at greater heliocentric distances. As a result, it is impossible to infer the pitch angle of spiral arms directly from observations, because such a determination would require kinematic data for a solar neighborhood comparable in size with the distance to the Galactic center. The basic idea of our approach to analyzing the velocity field is to determine the wavelength λ of periodic velocity variations along the galactic radius-vector ignoring the nonzero spiral-arm pitch angle and assuming spiral-arm fragments to have the shapes of circular segments. The wavelength in question is to a first approximation equal to the inter-arm distance. We first applied this technique to the Cepheid velocity field and found $\lambda = 1.9 \pm 0.2$ kpc (Mel'nik *et al.* 1999). It is this parameter and not the spiral-arm pitch angle that we determine directly from an analysis of stellar kinematics. To estimate the pitch angle, we must also know the number or arms m. We can then determine the mean pitch angle i of spiral arms in terms of a model of regular spiral pattern using the simple relation $\tan i = \dfrac{\lambda m}{2\pi R_0}$ of the density wave theory (Lin *et al.* 1969). The number of spiral arms is very difficult to establish even from radio observations, because no reliable distance estimates are usually available for gas clouds and other spiral-arm indicators observed at radio frequencies at large heliocentric dis-

tances. For a two-armed spiral pattern a wavelength of $\lambda = 1.9$ kpc corresponds to a mean pitch angle of $i = 5°$.

In the density-wave theory there is a fixed phase shift of $\pi/2$ between the oscillations of radial and azimuthal components of velocity perturbations for tightly wound arms (Lin *et al.* 1969). However, simulations of the kinematics of spiral arms with allowance for gas-dynamic effects (Roberts 1969) showed both components to exhibit maximum variations at the shock front. Therefore, one would expect that the oscillations of the radial and azimuthal components of residual velocity must be synchronized, and their phases should not be shifted relative to each other. The allowance for shock effects, even in a coarse approximation, requires an independent determination of the phases of oscillations of the radial and azimuthal components of residual velocity. It is the dropping of the requirement of the fixed phase shift between the oscillations of the two components that allowed considerable perturbations in the azimuthal residual velocities to be found in the $0° < l < 180°$ region.

Unfortunately, our method allows us to determine the arm location only up to $\lambda/2$, i.e., up to shifting arms into the interarm space. Moreover, it is impossible to choose between the two solutions for the location of the spiral pattern based on kinematical data alone. For the final choice, we invoke the additional information about the location of starburst regions with respect to the periodic pattern found in the velocity field studied. This information allows us not only to choose the right spiral-pattern solution, but also to determine the position of the region considered (within 3 kpc from the Sun) with respect to the corotation radius.

It is impossible to analyze the spiral pattern of our Galaxy without the knowledge of reliable distances to the objects studied. The use of OB associations instead of individual stars allows, due to averaging, a more reliable distance scale to be constructed and more reliable velocities to be derived. OB associations are sparse groupings of young stars (Ambartsumyan 1949). A comparison of virial mass estimates of OB associations with the masses estimated by modeling their stellar content suggests that these groupings are gravitationally unbound. Presently, there are several partitions of galactic OB-stars into associations, those of Blaha and Humphreys (1989), Garmany and Stencel (1992), and Mel'nik and Efremov (1995). All these partitions are based on the catalog of luminous stars by Blaha and Humphreys (1989). However, Garmany and Stencel (1992) identified their OB associations only in the $50° < l < 155°$ region. Mel'nik and Efremov (1995) used the cluster analysis technique to identify the densest and most compact groups, the cores of OB associations. However, these groupings contain twice as few stars than the associations of Blaha and Humphreys and, moreover, in dense regions, kinematical data are available for a smaller fraction of stars. We therefore consider the partition of OB-stars into associations sug-

gested by Blaha and Humphreys (1989) to be more suitable for kinematical analyses. The sky-plane sizes of most of the OB associations of Blaha and Humphreys (1989) do not exceed 300 pc (except Cep OB1 and NGC 2439), and the use of these objects for identifying periodic patterns with typical scale lengths greater than 1 kpc is a quite correct procedure. The inclusion of a list OB-stars in the HIPPARCOS (1997) program allowed their space motions to be analyzed for the first time (de Zeeuw *et al.* 1999).

2. OBSERVATIONAL DATA

To construct the velocity field of OB associations, we used the following data:

(1) The catalog of stars in OB associations by Blaha and Humphreys (1989) and heliocentric distances r_{BH} of these associations;

(2) The catalog of classical Cepheids (Berdnikov 1987; Berdnikov *et al.* 2000) with distances on the so-called short distance scale (Berdnikov and Efremov 1985);

(3) The solar Galactocentric distance $R_0 = 7.1 \pm 0.5$ kpc (Rastorguev *et al.* 1994; Dambis *et al.* 1995; Glushkova *et al.* 1998);

(4) The short distance scale for OB associations, $r = 0.8 r_{BH}$, which is consistent with the short distance scale for Cepheids (Sitnik and Mel'nik 1996; Dambis *et al.* 2001);

(5) Stellar line-of sight velocities from the catalog by Barbier-Brossat and Figon (2000);

(6) Proper motions of stars adopted from the HIPPARCOS (1997) catalog.

The distances to OB associations that we use here and the solar Galactocentric distance were obtained on the same distance scale, which agrees with the short distance scale for Cepheids.

The catalog of Blaha and Humphreys (1989) includes a number of extended open clusters, such as Collinder 121 and Trumpler 16, because it is very difficult to distinguish unambiguously between OB associations and young clusters. However, we did not use in our analysis other young clusters that were not included in the catalog of Blaha and Humphreys (1989), because of a considerable overlap between the lists of OB association and young-cluster stars with known kinematical parameters (Glushkova 2000, private communication).

We determined median line-of-sight velocities for a total of 70 OB associations containing at least two stars with known line-of-sight velocities, and median tangential velocities, for 62 associations containing at least two stars with known proper motions. The velocity of each OB association is based, on the average, on 12 line-of-sight velocities and 11 proper motions of individual stars. We excluded the distant association

Ara OB1B ($r = 2.8$ kpc) from our sample because of its large V_z velocity component, which exceeds 20 km s^{-1}.

3. AN APPROACH TO THE SOLUTION

In the case of tightly wound spiral arms, the velocity field must exhibit variations of the magnitude and direction of residual stellar velocities (i.e., velocities corrected for the Solar apex motion and galactic rotation) on Galactocentric distance.

We now write the expressions for the perturbation of radial (V_R) and azimuthal (V_θ) components of residual velocities in the form of periodic functions of the logarithm of Galactocentric distance R:

$$V_R = f_R \sin\left(\frac{2\pi R_0}{\lambda}\ln(R/R_0) + \varphi_R\right), \qquad (1)$$

$$V_\theta = f_\theta \sin\left(\frac{2\pi R_0}{\lambda}\ln(R/R_0) + \varphi_\theta\right), \qquad (2)$$

where f_R and f_θ are the amplitudes of variations of velocity components V_R and V_θ at the solar galactocentric distance. Parameter λ (in kpc) characterizes the wavelength of the periodic velocity variations along the galactic radius-vector. Assuming that galactic arms have the shape of logarithmic spirals, we adopted a logarithmic dependence of the wave phase on Galactocentric distance, which degenerates into a linear function $R_0\ln(R/R_0) \approx R - R_0$ if $(R - R_0)/R_0$ is small.

To demonstrate that the periodic pattern in the field of residual velocities is independent of the adopted model of circular rotation, we found the parameters of the periodic pattern jointly with those of differential circular galactic rotation and the components of solar velocity. We inferred all these quantities from a joint solution of Bottlinger equations (Kulikovskiĭ 1985) for line-of-sight velocities V_r and velocity components V_l ($V_l = 4.738$ [km s^{-1} kpc^{-1} (arcsec yr^{-1})$^{-1}$]$\mu_l r$ and μ_l is the proper-motion component along the galactic longitude) along the galactic longitude with allowance for perturbations induced by the density wave:

$$V_r = -(-u_0^* \cos l \cos b + v_0 \sin l \cos b + w_0 \sin b)$$

$$+ R_0\Omega_0'(R - R_0)\sin l \cos b$$

$$+ 0.5R_0\Omega_0''(R - R_0)\sin l \cos b \qquad (3)$$

$$- f_R \sin\left(\frac{2\pi R_0}{\lambda}\ln(R/R_0) + \varphi_R\right)\cos(l + \theta)\cos b$$

$$+ f_\theta\left(\frac{2\pi R_0}{\lambda}\ln(R/R_0) + \varphi_R\right)\sin(l + \theta)\cos b,$$

$$V_l = -(u_0^* \sin l + v_0 \cos l)$$

$$+ \Omega_0'(R - R_0)(R_0\cos l - r\cos b)$$

$$+ 0.5\Omega_0''(R - R_0)^2(R_0\cos l - r\cos b) - \Omega_0 r\cos b \qquad (4)$$

$$+ f_R \sin\left(\frac{2\pi R_0}{\lambda}\ln(R/R_0) + \varphi_R\right)\sin(l + \theta)$$

$$+ f_\theta\left(\frac{2\pi R_0}{\lambda}\ln(R/R_0) + \varphi_\theta\right)\cos(l + \theta).$$

Here, θ is the azimuthal Galactocentric angle between the directions toward the star and the Sun; Ω_0 is the angular velocity of galactic rotation at the solar Galactocentric distance; Ω_0' and Ω_0'' are the first and second derivatives with respect to Galactocentric distance taken at a distance of R_0; u_0^*, v_0, and w_0 are the solar velocity components relative to the centroid of OB associations in the directions of X, Y, and Z axes, respectively. The X-axis is directed away from the Galactic center, the Y-axis is in the direction of galactic rotation, and the Z-axis points toward the North Galactic Pole. Velocity components u_0^* and v_0 include the solar-velocity perturbation due to the spiral density wave. (In galactic astronomy X axis is traditionally directed toward the Galactic center and one should therefore compare $-u_0^*$ and not u_0^* with the standard solar apex.) We adopted $w_0 = 7$ km s^{-1} for the solar velocity component along the z-coordinate (Kulikovskiĭ 1985; Rastorguev et $al.$ 1999).

To linearize equations (3) and (4) with respect to the oscillation phases φ_R and φ_θ, we rewrite the formulas for perturbations of velocity components V_R and V_θ as follows:

$$V_R = A_R \sin\left(\frac{2\pi R_0}{\lambda}\ln(R/R_0)\right)$$
$$+ B_R \cos\left(\frac{2\pi R_0}{\lambda}\ln(R/R_0)\right), \qquad (5)$$

$$V_\theta = A_\theta \sin\left(\frac{2\pi R_0}{\lambda}\ln(R/R_0)\right)$$
$$+ B_\theta \sin\left(\frac{2\pi R_0}{\lambda}\ln(R/R_0)\right). \qquad (6)$$

The parameters f_R, f_θ, φ_R, and φ_θ can then be found from the relations:

$$f_R^2 = A_R^2 + B_R^2; \quad f_\theta^2 = A_\theta^2 + B_\theta^2; \qquad (7)$$

$$\tan\varphi_R = B_R/A_R; \quad \tan\varphi_\theta = B_\theta/A_\theta. \qquad (8)$$

We computed the weight factors p in the equations for V_r and V_l as follows:

$$p_{Vr} = (\sigma_0^2 + \varepsilon_{Vr}^2)^{-1/2}, \qquad (9)$$

$$p_{Vl} = (\sigma_0^2 + (4738\varepsilon_{\mu l}r)^2)^{-1/2}. \qquad (10)$$
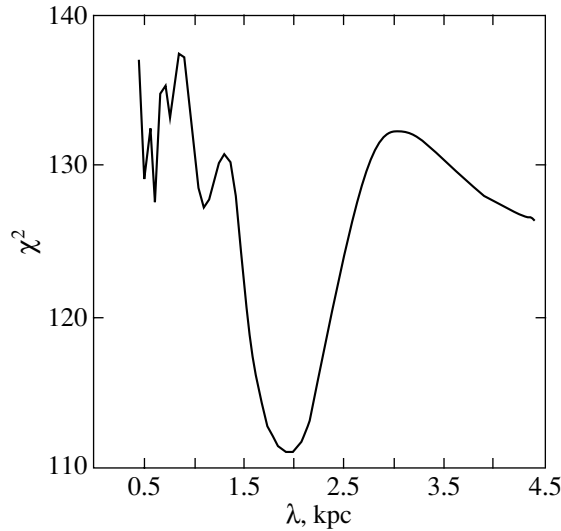
Fig. 1. The function $\chi^2(\lambda)$ for the joint solution of the system of equations (3) and (4) for the entire sample of OB associations.

Here, σ_0 is the dispersion of residual velocities of OB associations with respect to the adopted model of motion (without allowance for the triaxial shape of the velocity distribution); ε_{Vr} and $\varepsilon_{\mu l}$ are the standard errors of measured stellar line-of-sight velocities and proper motions, respectively. We determined the dispersion using iterations technique, which yielded $\sigma_0 = 6.6\,\mathrm{km\,s^{-1}}$.

We then applied the least-squares technique to find a joint solution of the system of equations (3) and (4), which are linear with respect to the parameters u_0^*, v_0, Ω_0', Ω_0'', Ω_0, A_R, B_R, A_θ, and B_θ, with weight factors (9) and (10) and fixed λ [see p. 499 in the book by Press *et al.* (1987)]. We estimate the wavelength λ by minimizing function $\chi^2(\lambda)$, which is equal to the sum of squares of the normalized velocity residuals.

4. RESULTS

4.1. Parameters of the Rotation Curve and Periodic Pattern Inferred from the Entire Sample of OB Associations

Figure 1 shows χ^2 as a function of λ, based on a joint solution of the system of equations (3) and (4) for line-of-sight and tangential velocities of OB associations located within 3 kpc from the Sun. χ^2 takes its minimum value at $\lambda = 2.0$ kpc. The resulting amplitudes of radial and azimuthal velocity perturbations are equal to $f_R = 6.6 \pm 1.4\,\mathrm{km\,s^{-1}}$ and $f_\theta = 1.8 \pm 1.4\,\mathrm{km\,s^{-1}}$, respectively. Table 1 gives the inferred values of all determined parameters: u_0^*, v_0, Ω_0', Ω_0'', Ω_0, λ, A_R, B_R, A_θ, and B_θ, as well as f_R, f_θ, φ_R, and φ_θ computed using formulas (7) and (8). The table also gives the standard errors of the above parameters, the number N of equations used, and the rms residual σ_0.

We then performed numerical simulations in order to estimate the standard error of the resulting λ. To this end, we fixed the actual galactic coordinates of OB associations and simulated normally distributed random errors in the heliocentric distances of OB associations with standard deviations equal to 10% of the true distance, and then used formulas (3) and (4) to compute a theoretical velocity field with allowance for the perturbations due to the density wave (we took all parameter values from Table 1). We then added to the theoretical velocities simulated normally distributed random errors with a standard deviation of σ, which includes the contribution of observational errors [$\sigma = 1/p_{Vr}$ and $\sigma = 1/p_{Vl}$, see formulas (9) and (10)]. The value of σ_0 was taken to be 7 km s^{-1}. We determined the wavelength λ for each simulated velocity field and found the inferred λ values to be unbiased and to have a standard error of 0.2 kpc.

We also explored the possibility of periodic patterns emerging accidentally in the velocity field of OB associations due to chance deviations of individual velocities from the circular rotation law. To this end, we simulated random errors in the velocities and heliocentric distances of OB associations and determined λ, f_R, and f_θ for each simulated field. Numerical simulations showed that 30% of all λ values fall within the wavelength interval $1 < \lambda < 3$ kpc that is of interest for us. It is in this λ interval that random fluctuations of the field of circular velocities can be attributed to density-wave effects. The mean amplitudes f_R and f_θ are equal to ~3 km s^{-1}, i.e., about twice the standard errors of the corresponding parameters inferred for the actual sample of OB associations (Table 1). However, the probability of a periodic pattern with an amplitude of $f_R \ge$

Table 1. Parameters of the circular rotation law, periodic pattern and solar-motion components inferred from an analysis of the line-of-sight velocities and proper motions of OB associations

N	u_0^*, km s^{-1}	v_0, km s^{-1}	Ω_0', km s^{-1} kpc^{-2}	Ω_0'', km s^{-1} kpc^{-3}	Ω_0, km s^{-1} kpc^{-1}	λ, kpc	A_R, km s^{-1}	B_R, km s^{-1}	A_θ, km s^{-1}	B_θ, km s^{-1}	f_R, km s^{-1}	f_θ, km s^{-1}	φ_R, deg	φ_θ, deg	σ_0, km s^{-1}
132	−7.5	11.2	−5.0	1.5	30.2	2.0	5.2	4.0	1.5	−1.0	6.6	1.8	38	−33	6.6
	± 0.9	± 1.3	± 0.2	± 0.2	± 0.8	± 0.2	± 1.4	± 1.3	± 1.4	± 1.4	± 1.4	± 1.4	± 12	± 48	

6.6 km s^{-1} and λ in the $1 < \lambda < 3$ kpc interval emerging accidentally is extremely low $P < 1\%$. Therefore, the hypothesis about the periodic pattern with an amplitude equal to $f_R = 6.6$ km s^{-1} emerging as a result of chance fluctuations in the velocities and heliocentric distances of OB associations can be rejected at a confidence level of $1 - P > 99\%$. However, chance oscillations in the field of azimuthal velocities with amplitudes $f_\theta \geq 1.8$ km s^{-1} and wavelengths λ in the $1 < \lambda < 3$ kpc interval appear rather frequently, in 25% of the cases, and, therefore, the periodic pattern found in the field of azimuthal velocities with $f_\theta = 1.8$ km s^{-1} can be interpreted in terms of random fluctuations.

4.2. Location of Spiral Arms in the Galactic Plane

A gravitational potential perturbation that propagates in a rotating disk at a supersonic speed produces a shock front, which affects the kinematics of gas and young stars born in this gas (Roberts 1969). The ages of OB associations do not exceed 5×10^7 years and, therefore, the motions of OB associations must be determined mainly by the velocities of their parent molecular clouds (Sitnik *et al.* 2001). Inside the corotation radius the shock front must coincide with the maximum radial velocity of streaming motions toward the Galactic center and maximum azimuthal velocity in the direction opposite that of galactic rotation. Velocities vary in magnitude value and reverse their direction as one recedes from the perturbation front. A sinusoidal law gives a first, coarse approximation to this pattern. According to the adopted model, in the interarm space, the radial and azimuthal components of streaming motions must be directed away from the Galactic center and along the galactic rotation, respectively (see Fig. 2 in Mel'nik *et al.* 1999).

Figure 2 shows the distribution of OB associations with known space velocities and the full vectors of residual velocities projected on the Galactic plane. We determined residual velocities as the differences between heliocentric velocities and circular rotation velocities, which also includes the motion of the Sun toward the apex, computed with parameters u_0^*, v_0, Ω_0', Ω_0'', and Ω_0 adopted from Table 1. Also shown are circular arcs corresponding to the maximum mean radial velocity V_R toward the Galactic center as defined by formula (1) and f_R and φ_R adopted from Table 1. Table 2 gives the following parameters for 59 associations with known space velocities: radial (V_R) and azimuthal (V_θ) components of residual velocities; components V_z of residual velocities along the z-coordinate; Galactocentric R and heliocentric r distances, and galactic coordinates l and b. To characterize the reliability of velocities and distances listed in Table 2, we also give the numbers n_r and n_l of association stars with known line-of-sight velocities and proper motions,
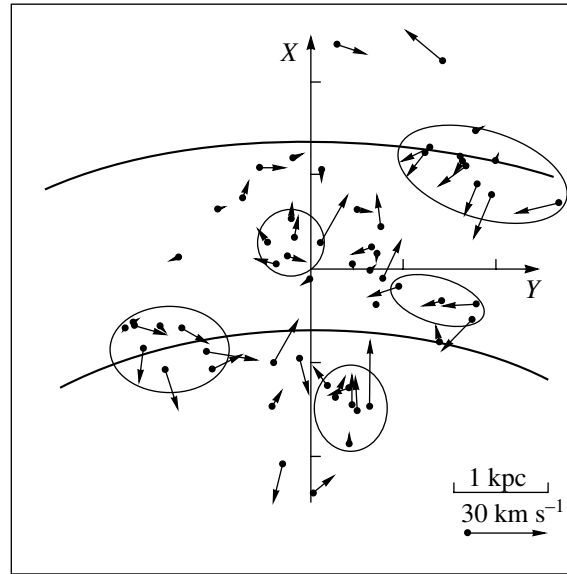

Fig. 2. The field of space velocities of OB associations projected onto the galactic plane. The *X*-axis is directed away from the Galactic center, and the *Y*-axis is in the direction of galactic rotation. The Sun is at the origin. The circular arcs correspond to the maximum radial component V_R of residual velocity toward the galactic center (solid line). One can see five star-forming regions where almost all OB associations have the same direction of radial velocity V_R.

respectively, and also the number N of members of the OB associations used to determine distance r.

Let us assume that the region studied is inside the corotation radius. It then follows, in view of the small value of the pitch angle, that the arcs shown in Fig. 2 should coincide with the shock front and must be located near the minima of gravitational potential minimum (Roberts 1969). Given a partition of young galactic objects into stellar-gas complexes (Efremov and Sitnik 1988), one can identify the star-forming regions through which the arms drawn in Fig. 2 pass. The arm located closer to the Galactic center passes in quadrant I near the OB associations of the Cygnus stellar-gas complex (Cyg OB3, OB1, OB8, and OB9) and in quadrant IV, through the OB associations and young clusters of the stellar-gas complex in the constellations of Carina, Crux, and Centaurus (Car OB1, OB2, Cru OB1, Cen OB1, Coll 228, Tr 16, Hogg 16, NGC 3766, and NGC 5606). Hereafter, we refer to this arc as the Cygnus–Carina arm. Another arm, which is farther from the Galactic center, passes in quadrant II near the OB associations of the stellar-gas complexes located in the constellations of Perseus, Casiopeia, and Cepheus (Per OB1, NGC 457, Cas OB8, OB7, OB6, OB5, OB4, OB2, OB1, and Cep OB1). In quadrant III, neither stellar-gas complexes nor even simply rich OB associations can be found to lie along the extension of this arc, which we refer to as the Perseus arm (Fig. 2). Note that Perseus–Cassiopeia and Carina–Centaurus stellar-gas complexes are the richest ones in the sense of the number of luminous stars their associations contain (see, e.g., Table 2).

Table 2. Residual velocities of OB associations

Association	l	b	r, kpc	R, kpc	V_R, km s^{-1}	V_θ, km s^{-1}	V_z, km s^{-1}	n_r	n_l	N
Sgr OB5	0.0°	−1.2°	2.4	4.7	7.5	9.0	8.0	2	3	31
Sgr OB1	7.6	−0.8	1.3	5.8	7.3	−5.4	1.0	37	29	66
Sgr OB7	10.7	−1.6	1.4	5.7	9.2	3.9	−14.4	3	2	4
Sgr OB4	12.1	−1.0	1.9	5.2	4.8	−0.0	−0.1	9	3	15
Ser OB1	16.7	0.1	1.5	5.7	13.0	−0.9	1.4	17	12	43
Sct OB3	17.3	−0.7	1.3	5.8	2.7	1.7	3.0	8	3	10
Ser OB2	18.2	1.6	1.6	5.6	13.7	−1.9	−3.7	7	5	18
Sct OB2	23.2	−0.5	1.6	5.7	26.3	−2.3	4.9	6	6	13
Vul OB1	60.4	0.0	1.6	6.5	6.4	−3.3	6.1	9	8	28
Vul OB4	60.6	−1.2	0.8	6.7	2.7	−0.1	−0.1	3	3	9
Cyg OB3	72.8	2.0	1.8	6.8	−14.5	−7.8	−4.0	30	18	42
Cyg OB1	75.8	1.1	1.5	6.9	−3.9	−8.3	1.2	34	14	71
Cyg OB9	77.8	1.8	1.0	7.0	−5.8	−12.2	0.2	10	8	32
Cyg OB8	77.9	3.4	1.8	7.0	−3.9	−13.9	12.8	9	10	21
Cyg OB4	82.7	−7.5	0.8	7.0	15.5	4.8	2.7	2	2	2
Cyg OB7	89.0	0.0	0.6	7.1	2.5	2.4	3.7	21	28	29
Lac OB1	96.7	−17.7	0.5	7.2	−3.6	−2.8	1.6	2	2	2
Cep OB2	102.1	4.6	0.7	7.3	−3.2	−0.1	2.8	37	47	59
Cep OB1	104.2	−1.0	2.8	8.2	−8.7	−14.3	3.1	17	24	58
Cas OB2	112.0	0.0	2.1	8.1	−19.0	−3.3	6.2	7	5	41
Cep OB3	110.4	2.6	0.7	7.4	−3.9	−4.9	0.5	18	15	26
Cas OB5	116.1	−0.5	2.0	8.2	−12.7	−2.7	−11.2	16	13	52
Cas OB4	120.1	−0.3	2.3	8.5	3.4	0.8	−6.4	7	7	27
Cas OB14	120.4	0.7	0.9	7.6	11.6	−2.7	2.3	4	3	8
Cas OB7	123.0	1.2	2.0	8.4	−10.3	−9.2	−2.7	4	8	39
Cas OB1	124.7	−1.7	2.0	8.4	−6.8	−2.5	−7.0	5	3	11
NGC 457	126.7	−4.4	2.0	8.4	−1.7	1.0	−6.7	4	2	4
Cas OB8	129.2	−1.1	2.3	8.7	2.3	2.5	−3.7	14	9	43
Per OB1	134.7	−3.2	1.8	8.5	−7.8	−12.2	−5.5	81	63	167
Cas OB6	135.0	0.8	1.8	8.4	−11.2	−6.8	−3.8	12	13	46
Cam OB1	141.1	0.9	0.8	7.7	−0.4	6.2	0.3	30	33	50
Cam OB3	147.0	2.8	2.6	9.4	9.5	−17.6	16.5	3	3	8
Per OB2	160.3	−16.5	0.3	7.4	16.0	9.6	−0.9	7	7	7
Aur OB1	173.9	0.1	1.1	8.2	−4.9	0.8	−2.7	26	20	36
Ori OB1	206.9	−17.7	0.4	7.4	8.2	0.5	0.3	62	59	70
Aur OB2	173.3	−0.2	2.4	9.5	−3.5	12.0	−2.8	4	2	20
Gem OB1	189.0	2.2	1.2	8.3	2.2	5.2	3.9	18	17	40
Mon OB1	202.1	1.1	0.6	7.6	6.3	0.5	1.8	7	7	7
Mon OB2	207.5	−1.6	1.2	8.2	−0.4	10.9	−0.5	26	18	32
CMa OB1	224.6	−1.6	1.1	7.9	7.2	3.5	−7.0	8	10	17
Coll 121	238.5	−8.4	0.6	7.4	5.9	−4.1	0.1	10	13	13
NGC 2362	237.9	−5.9	1.2	7.8	0.5	3.8	4.5	6	3	9
Coll 140	244.5	−7.3	0.3	7.2	−2.7	7.6	−1.5	5	6	6
Vela OB2	262.1	−8.5	0.4	7.2	2.2	−8.7	0.8	13	12	13
Vela OB1	264.9	−1.4	1.5	7.4	−0.5	−1.9	−2.5	18	18	46
Car OB1	286.5	−0.5	2.0	6.8	0.8	3.4	−2.2	39	18	126
Tr 16	287.3	−0.3	2.1	6.8	−2.3	−1.8	−2.6	5	2	18
Coll 228	287.6	−1.0	2.0	6.8	−6.6	10.0	−2.7	9	2	15
Car OB2	290.4	0.1	1.8	6.7	−4.3	2.2	0.3	22	12	59
Cru OB1	294.9	−1.1	2.0	6.5	−13.5	−6.1	−0.2	33	19	76
NGC 3766	294.1	−0.0	1.5	6.6	−7.3	7.9	0.5	2	2	12
Cen OB1	304.2	1.4	1.9	6.2	−16.8	0.6	−2.4	32	32	103
Hogg 16	307.5	1.4	1.5	6.3	−7.4	19.9	−11.7	3	3	5
NGC 5606	314.9	1.0	1.5	6.1	3.2	12.4	−6.6	3	2	5
Ara OB1A	337.7	−0.9	1.1	6.1	15.4	10.0	−3.8	8	10	53
Sco OB1	343.7	1.4	1.5	5.6	6.0	4.2	1.1	28	16	76
Sco OB2	351.3	19.0	0.1	7.0	−3.3	−3.1	0.7	10	10	10
HD 156154	351.3	1.4	2.1	5.0	−15.6	−5.1	−2.1	3	2	4
Sco OB4	352.7	3.2	1.0	6.2	−15.0	2.7	−3.2	7	4	11

If we assume that the solar neighborhood considered is located outside the corotation radius, the shock front and the minimum of potential should coincide with the maximum velocity of streaming motions directed away from the Galactic center and maximum velocity of azimuthal streaming motions in the direction of galactic rotation. The arms should then be shifted by $\sim\lambda/2$ relative to the lines drawn in Fig. 2, putting the rich stellar-gas complexes of the Cygnus-Carina and Perseus arms into the interarm space. Such a pattern would be inconsistent with modern concepts of star formation and the results of observations of other galaxies, which indicate that starburst regions concentrate toward spiral arms (Elmegreen 1979; Efremov 1989).

The fact that radial residual velocities of almost all OB associations in rich stellar-gas complexes are directed toward the Galactic center indicates that the region studied is located inside the corotation radius.

4.3. Kinematically Distinct Star-Forming Regions

However, things are not all that straightforward. An analysis of the data in Table 2 showed that about 30% of rich OB associations (containing more than 30 members with known photometric parameters, $N > 30$), exhibit kinematic signatures characteristic of the interarm space. In particular, they have their radial residual velocity components V_R directed away from the Galactic center. This is not a surprise, because star formation can also proceed in the interarm space (Elmegreen and Wang 1987). In the solar neighborhood (Fig. 2), two regions can be identified where most of OB associations have radial velocities V_R directed away from the Galactic center. These are the associations of the Local system located in quadrants II and III (Vela OB2, Mon OB1, Coll 121, Ori OB1, and Per OB2) and the stellar-gas complex projected onto the constellations of Sagittarius, Scutum, and Serpens (Sgr OB1, OB7, OB4, Ser OB1, OB2, Sct OB2, and OB3) (Efremov and Sitnik 1988). These regions are located in the interarm space of the pattern shown in Fig. 2. It is the alternation of star-forming regions with positive and negative radial residual velocities V_R that determines the periodic pattern of the field of radial velocities of OB associations.
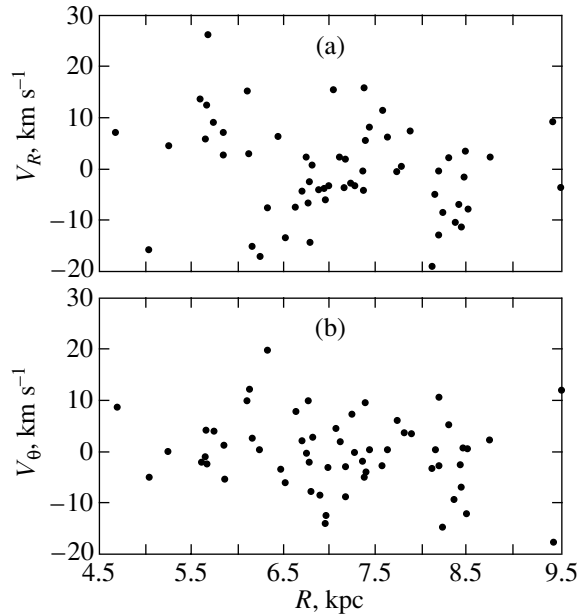

Fig. 3. The (a) radial (V_R) and (b) azimuthal (V_θ) component of residual velocities of OB associations of the entire sample as a function of Galactocentric distance.

Within 3 kpc from the Sun, a total of five star-forming regions can be identified where almost all associations have the same direction of the radial component V_R of residual velocity. The contours of these regions are shown in Fig. 2. Table 3 gives for each such region its mean Galactocentric distance R, mean residual velocities of associations V_R and V_θ; the interval of coordinates l and r, and the names of OB associations with known space velocities it contains.

Table 3 shows a well-defined alternation of the directions of the mean radial velocity V_R of OB associations as a function of increasing Galactocentric distance R. The periodic pattern is especially conspicuous in Fig. 3a, which shows the variation of the radial component of residual velocity of OB associations along the Galactocentric distance. Radial velocities of OB associations in the Carina–Centaurus ($R = 6.5$ kpc), Cygnus ($R = 6.9$ kpc), and Perseus–Cassiopeia ($R = 8.4$ kpc) complexes are directed mainly toward the Galactic center,

Table 3. Kinematically distinct regions of OB associations within 3 kpc from the Sun

Region	R, kpc	V_R, km s^{-1}	V_θ, km s^{-1}	l, deg	r, kpc	Associations
Sagittarius–Scutum complex	5.6	$+11 \pm 3$	-1 ± 1	8–23	1.3–1.9	Sgr OB1, OB7, OB4, Ser OB1, OB2, Sct OB2, OB3
Carina–Centaurus complex	6.5	-6 ± 2	$+5 \pm 3$	286–315	1.5–2.1	Car OB1, OB2, Cru OB1, Cen OB1, Coll 228, Tr 16, Hogg 16, NGC 3766, 5606
Cygnus complex	6.9	-7 ± 3	-11 ± 2	73–78	1.0–1.8	Cyg OB1, OB3, OB8, OB9
Part of the Local System	7.4	$+6 \pm 3$	$+1 \pm 3$	160–262	0.3–0.6	Per OB2, Mon OB1, Ori OB1, Vela OB2, Coll 121, 140
Perseus–Cassiopeia complex	8.4	-7 ± 2	-5 ± 2	104–135	1.8–2.8	Per OB1, NGC 457, Cas OB8, OB7, OB6, OB5, OB4, OB2, OB1, Cep OB1

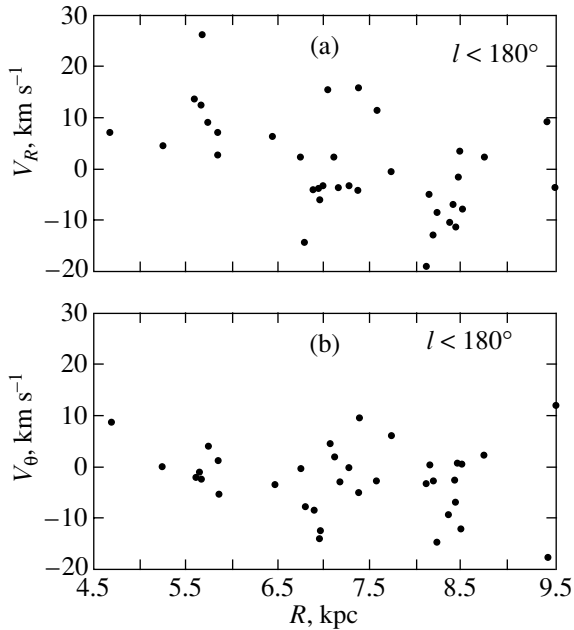**Fig. 4.** The (a) radial (V_R) and (b) azimuthal (V_θ) components of residual velocities of OB associations in the region $0° < l < 180°$ as functions of Galactocentric distance.
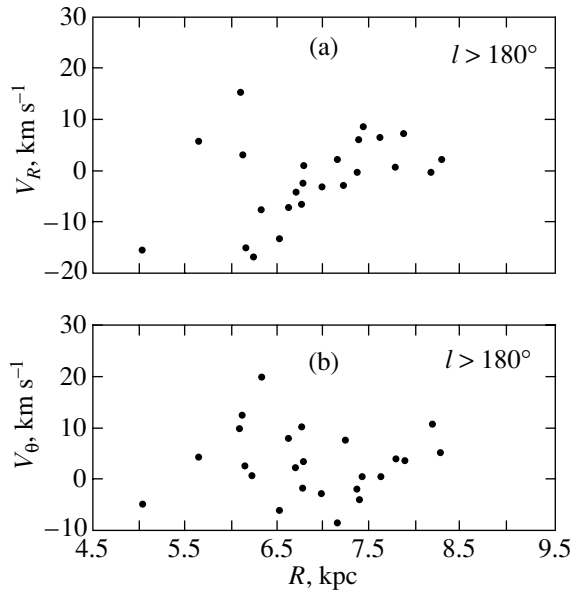

Fig. 5. The (a) radial (V_R) and (b) azimuthal (V_θ) components of residual velocities of OB associations in the region $180° < l < 360°$ as functions of Galactocentric distance.

whereas those in the Sagittarius–Scutum complex ($R = 5.6$ kpc) and in a part of the Local system ($R = 7.4$ kpc) are directed away from the Galactic center. The velocities V_R of other OB associations located outside the above complexes are, on the average, smaller in magnitude, also in agreement with the periodic pattern inferred.

4.4. Specific Features of the Periodic Pattern in the Velocity Field of OB Associations in the $l < 180°$ and $l > 180°$ Regions

To study the specific features of the velocity field of OB associations, we analyzed residual velocities of these objects as a function of Galactocentric distance separately for the two regions $l < 180°$ and $l > 180°$ (Fig. 4 and 5, respectively). Figure 4b shows the azimuthal velocity field of OB associations to exhibit a well-defined periodic pattern in the region $l < 180°$, whereas no such pattern can be seen in the field of velocity components V_θ of the entire sample of OB associations (Fig. 3b and Table 1). The mean amplitude of azimuthal velocity variations in the region considered is as high as $f_\theta = 5.1 \pm 1.7$ km s^{-1}, i.e., almost triple the value of $f_\theta = 1.8 \pm 1.4$ km s^{-1} inferred from the entire sample of OB associations. One can see two well-defined minima at Galactocentric distances $R = 7.0$ and 8.4 kpc. It is evident from a comparison of Figs. 4a and 4b that the minima in the distributions of radial and azimuthal residual velocities are located at the same Galactocentric distances.

In the density-wave theory including shock effects, the minima in the distributions of the radial and azimuthal components of residual velocities must coincide with the shock front and should be located in the vicinity of the line of minimum potential (Roberts 1969). The striking agreement between the positions of minima as inferred from the distributions of radial and azimuthal residual velocities of OB associations of quadrants I and II (Figs. 4a, 4b) can be explained by the shock front. The positions of these minima determine the kinematical positions of the Cygnus and Perseus–Cassiopeia arms putting them at Galactocentric distances of $R = 6.8$–7.0 kpc and $R = 8.2$–8.5 kpc, respectively.

In the region $l > 180°$, the periodic pattern is represented by a single minimum and two maxima in the distribution of radial velocities V_R (Fig. 5a). The minimum at the Galactocentric distance $R = 6.2$–6.5 kpc determines the kinematic position of the Carina arm, whereas another minimum is absent, which would correspond to the extension of the Perseus arm toward quadrant III. The maximum at $R = 7.5$ kpc (Fig. 5a) is associated with the positive radial velocities of the Local system OB associations in quadrant III. No periodic pattern in the field of azimuthal velocities can be seen in the region $l > 180°$ (Fig. 5b). That is why merging the association samples from the two regions ($l < 180°$ and $l > 180°$) washes out the periodic pattern (Fig. 3b), although the latter is clearly outlined by the associations of quadrants I and II (Fig. 4b).

For a quantitative analysis, we inferred the parameters of the periodic pattern in the velocity field of OB associations in two regions: $0° < l < 180°$ and $180° < l < 360°$ by solving the system of equations (3) and (4) with weight factors (9) and (10) and the parameters of circular rotation and solar-motion components adopted

from Table 1. Table 4 gives the following parameters of the periodic pattern inferred for the two regions: λ, f_R, f_θ, φ_R, and φ_θ, their standard errors, the number N of equations used, and the mean residual σ_0.

It is evident from Table 4 that in the region $0° < l < 180°$ radial and azimuthal residual velocities have similar variation amplitudes equal to $f_R = 6.7 \pm 1.7$ km s^{-1} and $f_\theta = 5.1 \pm 1.7$ km s^{-1}, respectively. The phases of the variations of the radial and azimuthal velocity components ($\varphi_R = 52° \pm 15°$ and $\varphi_\theta = -15° \pm 20°$) differ significantly from each other, although, as is evident from Figs. 4a, 4b, the minima of the radial and azimuthal velocities are located at the same Galactocentric distances. The discrepancy is primarily due to the simple sinusoidal law adopted for our analysis of the periodic pattern. Large radial velocities of the OB associations in the Sagittarius–Scutum region ($0° < l < 30°$) break the almost ideal periodic pattern outlined by the objects located in the Cygnus and Perseus–Cassiopeia arms and in the adjoining interarm space. Excluding from our sample the OB associations located in the region $0° < l < 30°$ changes phase φ_R significantly. The parameters of the periodic pattern inferred in the $30° < l < 180°$ sector for the objects located in the Cygnus and Perseus–Cassiopeia arms and in the adjoining interarm space are also listed in Table 4. It is evident from this table that in the sector considered the phases of radial and azimuthal velocity oscillations agree with each other within the errors ($\varphi_R = -7° \pm 15°$ and $\varphi_\theta = -26° \pm 18°$, respectively). The reliably determined wavelength $\lambda = 1.4 \pm 0.2$ kpc for the region $30° < l < 180°$ is equal to the distance between the Cygnus and Perseus–Cassiopeia arms, or rather to that between the minima in the distributions of both radial and azimuthal residual velocities (Figs. 4a, 4b).

In the region $180° < l < 360°$, the mean amplitude of radial velocity oscillations is equal to $f_R = 8.1 \pm 2.0$ km s^{-1}. Here the wavelength is determined as the distance between the maxima in the distribution of radial velocities; i.e., λ proves to be equal to the distance between the interarm-space objects (Fig. 5a). The wavelength inferred for this region, $\lambda = 2.4 \pm 0.4$ kpc, is rather uncertain, because the Galactocentric dependence of residual velocity differs appreciably from the sinusoidal law.

Numerical simulations of the velocity field allow the hypothesis that the variations of either radial or azimuthal velocities in the region $30° < l < 180°$, with amplitudes equal to $f_R = 6.9$ km s^{-1} and $f_\theta = 6.1$ km s^{-1}, respectively, are due to accidental errors in the velocities and distances, to be rejected at a confidence level of $1 - P \geq 95\%$. On the other hand, the only statistically significant periodic pattern in the region $180° < l < 360°$ is that of radial velocities ($1 - P \geq 99\%$), whereas azimuthal velocity variations can well ($P = 15\%$) be interpreted in terms of random fluctuations.

Figure 6a illustrates the specific features of the periodic pattern found in this work. It also shows the field of residual velocities of OB associations and the circu-

Table 4. Parameters of the periodic pattern in the velocity field of OB associations located in different regions

Region	N	λ, kpc	f_R, km s^{-1}	f_θ, km s^{-1}	φ_R, deg	φ_θ, deg	σ_0, km s^{-1}
$0° < l < 180°$	73	1.7	6.7	5.1	52	–15	6.2
		± 0.2	± 1.7	± 1.7	± 15	± 20	
$30° < l < 180°$	56	1.4	6.9	6.1	–7	–26	6.0
		± 0.2	± 1.8	± 1.9	± 15	± 18	
$180° < l < 360°$	59	2.4	8.1	4.4	7	251	6.2
		± 0.4	± 2.0	± 1.8	± 12	± 24	

lar arcs corresponding to the minima of residual radial (V_R) (solid line) and azimuthal (V_θ) (dashed line) velocities based on parameters f_R, f_θ, φ_R, and φ_θ for regions $180° < l < 360°$ and $30° < l < 180°$ (Table 4). The arcs must be located in the vicinity of the lines of minimum gravitational potential. In the region $30° < l < 180°$, these lines determine the loci of the Cygnus and Perseus–Cassiopeia arms and in the region $180° < l < 360°$, that of the Carina–Centaurus arm. Numerical simulations showed the inferred Galactocentric distances of arms and, correspondingly, the radii of arcs in Fig. 6a, to have standard errors of 0.1–0.2 kpc.

Figure 6a illustrates all three specific features of the velocity field of OB associations. First, the periodic pattern of azimuthal velocities in the region $0° < l < 180°$ and the absence of such pattern in the region $180° < l < 360°$. Second, the agreement of Galactocentric distances of the Cygnus and Perseus–Cassiopeia arms as inferred from analyses of the fields of radial and azimuthal velocities in the region $30° < l < 180°$. Third, a 0.3 kpc shift of the kinematical positions of the Carina arm ($R = 6.5 \pm 0.1$ kpc) relative to that of the Cygnus arm ($R = 6.8 \pm 0.1$ kpc). Whether this shift is statistically significant remains an open question.

5. COMPARISON OF PERIODIC PATTERNS IN THE VELOCITY FIELDS OF CEPHEIDS AND OB ASSOCIATIONS

An analysis of the velocity field of Cepheids (Mel'nik *et al.* 1999) revealed a periodic pattern along the galactic radius-vector with a scale length of $\lambda = 1.9 \pm 0.2$ kpc and mean oscillation amplitudes of $f_R = 6.2 \pm 1.2$ km s^{-1} and $f_\theta = 2.1 \pm 1.2$ km s^{-1}. It would be interesting to see whether the periodic pattern of the Cepheid velocity field exhibits the same specific features as that of OB associations.

To answer this question, we inferred the parameters of the periodic pattern of the Cepheid velocity field in three regions $0° < l < 180°$, $30° < l < 180°$, and $180° < l < 360°$ in the same way as we did it for OB associations (Table 5). Note that the exclusion of the region $0° < l < 30°$ has no effect on the inferred parameters of the periodic pattern in the Cepheid velocity field. We used the parameters of circular motion and solar-motion components that we inferred from the analysis
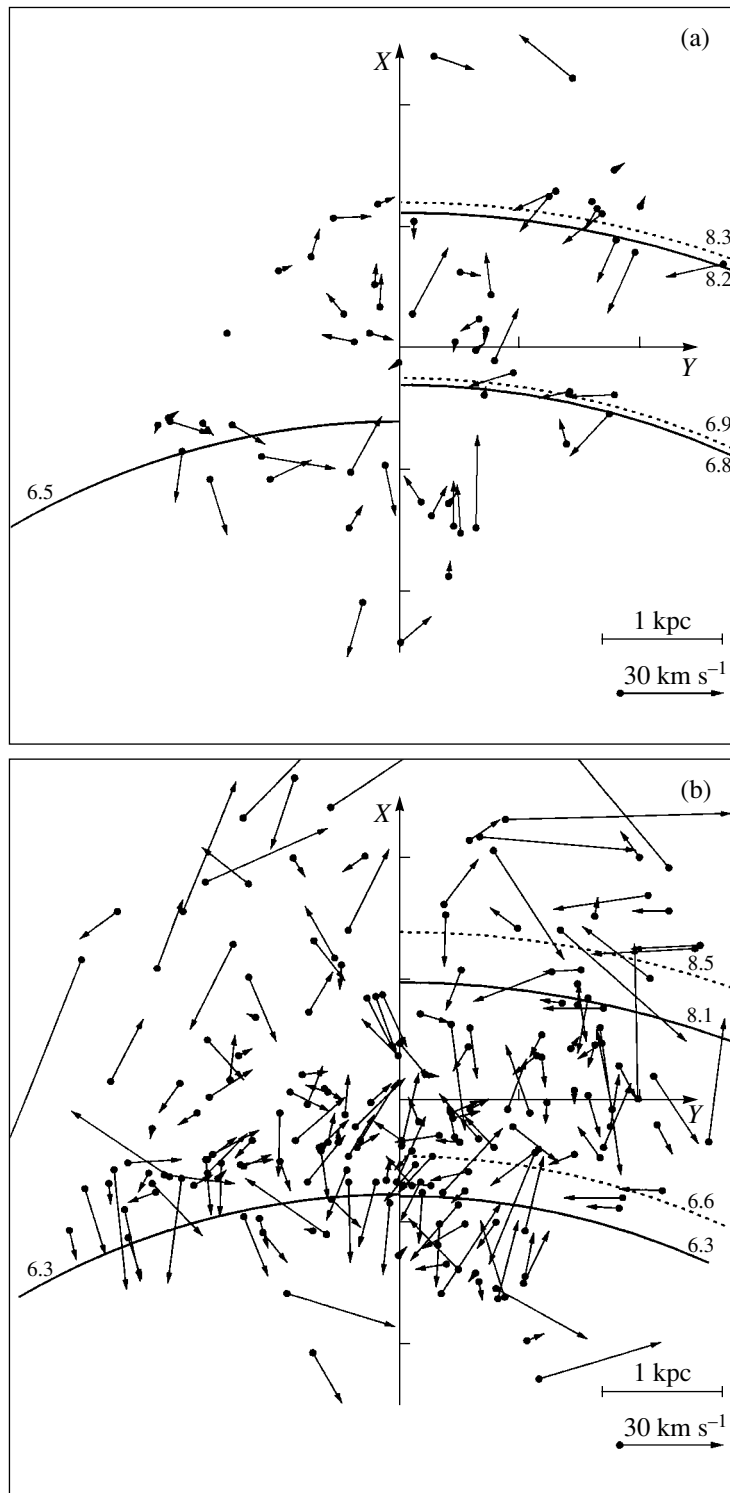
Fig. 6. The field of residual velocities of (a) OB associations and (b) Cepheids. The circular arcs correspond to the positions of Cygnus, Carina, and Perseus arm fragments as inferred from analyses of radial (solid line) and azimuthal (dashed line) residual velocities in the regions $30° < l < 180°$ and $180° < l < 360°$. Numbers indicate the Galactocentric distances of arms (in kpc).

of the entire sample of Cepheid located within 3 kpc from the Sun [see table in Mel'nik *et al.* (1999)]: $u_0^* = -7.6 \pm 0.8$ km s^{-1}; $v_0 = 11.6 \pm 1.0$ km s^{-1}; $\Omega_0' = -5.1 \pm 0.2$ km s^{-1} kpc^{-2}; $\Omega_0'' = 1.0 \pm 0.2$ km s^{-1} kpc^{-3}, and

$\Omega_0 = 29 \pm 1$ km s^{-1} kpc^{-1}. These parameters agree within the errors with the corresponding parameters of the velocity field of OB associations (Table 1).

It is evident from Table 5 that in the region $30° < l < 180°$ both radial and azimuthal velocity fields contain a

Table 5. Parameters of the periodic pattern in the velocity field of Cepheids located in different regions

Region	N	λ, kpc	f_R, km s^{-1}	f_θ, km s^{-1}	φ_R	φ_θ	σ_0, km s^{-1}
$0° < l < 180°$	217	1.8	6.7	5.1	85°	13°	10.2
		± 0.2	± 1.6	± 1.5	± 14°	± 17°	
$30° < l < 180°$	165	1.8	6.5	6.5	82°	9°	9.8
		± 0.2	± 1.8	± 1.7	± 16°	± 15°	
$180° < l < 360°$	208	1.8	5.8	2.0	78°	154°	10.4
		± 0.3	± 1.7	± 1.5	± 16°	± 48°	

periodic component. The amplitudes of velocity variations are equal to $f_R = f_\theta = 6.5 \pm 1.8$ km s^{-1}. Numerical simulations show that the hypothesis about the accidental nature of the periodic variations found in the fields of radial and azimuthal residual velocities in the region $30° < l < 180°$ can be rejected at a confidence level of $1 - P > 99\%$. The periodic pattern revealed in the radial-velocity field in the region $180° < l < 360°$ with an amplitude of $f_R = 5.8 \pm 1.7$ km s^{-1} is also by no means due to fluctuations ($1 - P > 99\%$); however, the variations of azimuthal velocities with an amplitude of $f_\theta = 2.0 \pm 1.5$ km s^{-1} can well ($P = 25\%$) be due to random fluctuations.

Figure 6b shows the field of Cepheid residual velocities and, based on f_R, f_θ, φ_R, and φ_θ from Table 5, the circular arcs corresponding to the minima of mean radial (V_R) (solid line) and azimuthal (V_θ) (dashed line) velocities. These arcs determine the kinematical positions of the Cygnus, Perseus–Cassiopeia, and Carina–Centaurus arms. The radii of arcs in Fig. 6b are determined with an accuracy of 0.1–0.2 kpc.

The fields of residual velocities of OB associations and Cepheids can be seen to have many features in common. First, the galactocentric distances of the Carina–Centaurus ($R = 6.3$–6.5 kpc) and Perseus–Cassiopeia ($R = 8.1$–8.2 kpc) arms as inferred from analyses of radial velocities of Cepheids and OB associations agree well with each other. Second, both the Cepheids and OB associations located in quadrants I and II exhibit periodic variations of the azimuthal velocity with an amplitude of $f_\theta \approx 6 \pm 2$ km s^{-1}, whereas the azimuthal velocities of both populations show no periodic pattern in quadrants III and IV. However, the velocity field of Cepheids somewhat differs from that OB associations. Thus, Cepheids do not show the 0.3-kpc shift between the positions of the Cygnus and Carina arms as inferred from radial velocities of OB associations. The Galactocentric distances of the Cygnus arm as inferred from analyses of radial velocities of Cepheids ($R = 6.3 \pm 0.1$ kpc) and OB associations ($R = 6.8 \pm 0.1$ kpc) differ significantly from each other. In contrast to OB associations, Cepheids do not show such a good agreement between the positions of the Cygnus and Perseus–Cassiopeia arms as inferred from analyses of the radial and azimuthal velocity fields.

CONCLUSION

An analysis of the field of space velocities of OB associations located within 3 kpc from the Sun revealed periodic variations in the magnitude and direction of radial residual velocities V_R along the galactic radius-vector with a typical scale length of $\lambda = 2.0 \pm 0.2$ kpc and a mean amplitude of $f_R = 7 \pm 1$ km s^{-1}.

We revealed five kinematically distinct star-forming regions where almost all OB associations have the same direction of radial residual velocity V_R. The radial velocities of OB associations in the Carina–Centaurus, Cygnus, and Perseus–Cassiopeia regions are directed mainly toward the Galactic center, whereas those of the Sagittarius–Scutum complex and of a part of the Local system, are directed away from the Galactic center. It is the alternation of star-forming regions with positive and negative radial velocities V_R that determines the periodic pattern of the radial velocity field of OB associations.

The fact that rich Carina–Centaurus and Perseus–Cassiopeia stellar-gas complexes lie in the vicinity of the minima in the distribution of radial velocities of OB associations indicates that the region considered is located inside the corotation radius. The enhanced density of high-luminosity stars in these regions cannot be due to observational selection, because the Carina–Centaurus and Perseus–Cassiopeia complexes are the most distant ones among those considered in this paper (Fig. 2 and Table 3). Furthermore, these regions cover sky areas extending for several tens of degrees and at a heliocentric distance of 2 kpc the mean extinction averaged over such large sectors depends little on the direction within the galactic plane. There is no doubt, the enhanced density of high-luminosity stars in the Carina–Centaurus and Perseus–Cassiopeia complexes is real and not due to the extremely low extinction along the corresponding lines of sight.

The fact that the Perseus–Cassiopeia complex ($R = 8.4$ kpc) is located inside the corotation radius imposes a lower limit on the corotation radius, $R_C - R_0 > 1.3$ kpc and an upper limit on the spiral pattern speed, $\Omega_p < 25$ km s^{-1} kpc^{-1}.

Our conclusion about the corotation radius R_C being located in the outer part of the Galaxy beyond the Perseus–Cassiopeia arm is in conflict with the conclusions of Mishurov and Zenina (1999a, 1999b) who argue that the Sun is located near the corotation radius $|R_0 - R_C| < 1$ kpc. The latter authors based their conclusions on the small value of radial ($|f_R| = 2 \pm 1$ km s^{-1}) and large value of azimuthal ($|f_\theta| = 8 \pm 1$ km s^{-1}) velocity perturbation amplitudes they inferred (Mishurov and Zenina 1999b). Our analysis yielded a reversed amplitude proportion with $f_R = 7 \pm 1$ km s^{-1} and $f_\theta = 2 \pm 1$ km s^{-1} both for Cepheid (Mel'nik *et al.* 1999) and OB association data (Table 1). At the same time, the pitch angle found $i = -5$ by Mishurov and Zenina (1999a, 1999b) for a two-armed spiral pattern corresponds to $\lambda = 2$ kpc and is consistent with our results.

As for the periodic pattern in the field of azimuthal velocities of OB associations, it is observed in quadrants I and II and is absent in quadrants III and IV. The mean amplitude of azimuthal velocity variations in the region of the Cygnus and Perseus arms ($30° < l < 180°$) is as high as $f_\theta = 6 \pm 2$ km s^{-1}, i.e., triple that of the entire sample of OB associations. Another specific feature is the striking agreement between the positions of the Cygnus and Perseus–Cassiopeia arms as inferred from separate analyses of radial and azimuthal velocity fields of OB associations. This feature can be explained by shocks that develop when a density wave propagates through gas at a supersonic velocity.

The periodic patterns in the residual velocity fields of Cepheids and OB associations have very much in common: similar scale length of radial velocity variations along the galactic radius vector, $\lambda = 2.0 \pm 0.2$ kpc and similar amplitudes of velocity variations. Moreover, in both cases the azimuthal velocity fields of objects located in the I and II quadrants exhibit a periodic pattern, whereas no such pattern can be seen in the azimuthal velocity field in quadrants III and IV.

The kinematical positions of the Carina–Centaurus ($R = 6.3$–6.5 kpc) and Perseus–Cassiopeia ($R = 8.1$–8.2 kpc) arms can be confidently inferred from an analysis of the field of radial velocities of both OB associations and Cepheids. It is the distance between these two arm fragments that determines the scale length of the variations of the radial velocity component along the galactic radius-vector, $\lambda \approx 2$ kpc.

The wavelength value that we inferred, $\lambda = 2$ kpc, seems to coincide with that of the most unstable mode of galactic disk oscillations at the given Galactocentric distance. The very existence of the spiral pattern suggests that the galactic disk is marginally unstable at the solar Galactocentric distance. Presently, the gaseous component of the galactic disk is considered to be instrumental in maintaining such a marginal instability (Jog and Solomon 1984; Bertin and Romeo 1988; Bertin *et al.* 1989). Jog and Solomon (1984) showed that the wavelength of the most unstable disk mode depends on the gas fraction. They found that the wavelengths of the most unstable disk modes at the solar Galactocentric distance should lie in the 1–5 kpc interval, where 1 and 5 kpc correspond to a purely gaseous and purely stellar disk, respectively. Our result $\lambda = 2$ kpc suggests that both components play important part in the dynamics of our Galaxy.

ACKNOWLEDGMENTS

REFERENCES

1. V. A. Ambartsumyan, Astron. Zh. **26**, 3 (1949).
2. M. Barbier-Brossat and P. Figon, Astron. Astrophys., Suppl. Ser. **142**, 217 (2000).
3. L. N. Berdnikov, Perem. Zvezdy **22**, 505 (1987).
4. L. N. Berdnikov and A. D. Chernin, Pis'ma Astron. Zh. **25**, 684 (1999) [Astron. Lett. **25**, 591 (1999)].
5. L. N. Berdnikov and Yu. N. Efremov, Astron. Tsirk., No. 1388, 1 (1985).
6. L. N. Berdnikov, A. K. Dambis, and O. V. Vozyakova, Astron. Astrophys., Suppl. Ser. **143**, 211 (2000).
7. G. Bertin and A. B. Romeo, Astron. Astrophys. **195**, 105 (1988).
8. G. Bertin, C. C. Lin, S. A. Lowe, and R. P. Thurstans, Astrophys. J. **338**, 78 (1989).
9. C. Blaha and R. M. Humphreys, Astron. J. **98**, 1598 (1989).
10. W. B. Burton, Astron. Astrophys. **10**, 76 (1971).
11. W. B. Burton and T. M. Bania, Astron. Astrophys. **33**, 425 (1974).
12. M. Creze and M. O. Mennessier, Astron. Astrophys. **27**, 281 (1973).
13. A. K. Dambis, A. M. Mel'nik, and A. S. Rastorguev, Pis'ma Astron. Zh. **21**, 331 (1995) [Astron. Lett. **21**, 291 (1995)].
14. A. K. Dambis, A. M. Mel'nik, and A. S. Rastorguev, Pis'ma Astron. Zh. **27**, 68 (2001) [Astron. Lett. **27**, 58 (2001)].
15. Yu. N. Efremov, *Sites of Star Formation* (Nauka, Moscow, 1989).
16. Yu. N. Efremov, Astron. Astrophys. Trans. **15**, 3 (1998).
17. Yu. N. Efremov and T. G. Sitnik, Pis'ma Astron. Zh. **14**, 817 (1988) [Sov. Astron. Lett. **14**, 347 (1988)].
18. B. G. Elmegreen, Astrophys. J. **231**, 372 (1979).
19. B. G. Elmegreen and M. Wang, in *Lecture Notes in Physics*, Vol. 315: *Molecular Clouds in the Milky Way and External Galaxies*, Ed. by R. L. Dickman, R. L. Snell, and J. S. Young (Springer-Verlag, Amherst, 1987), p. 240.
20. R. P. Fenkart and B. Binggeli, Astron. Astrophys., Suppl. Ser. **35**, 271 (1979).
21. C. D. Garmany and R. E. Stencel, Astron. Astrophys., Suppl. Ser. **94**, 211 (1992).
22. T. P. Gerasimenko, Astron. Zh. **70**, 953 (1993) [Astron. Rep. **37**, 480 (1993)].
23. E. V. Glushkova, private communication (2000).
24. E. V. Glushkova, A. K. Dambis, A. M. Mel'nik, and A. S. Rastorguev, Astron. Astrophys. **329**, 514 (1998).
25. R. M. Humphreys, in *Proceedings of the IAU Symposium No. 84 on the Large Scale Characteristics of the Galaxy,* Ed. by W. B. Burton (Reidel, Dordrecht, 1979), p. 93.
26. C. J. Jog and P. M. Solomon, Astrophys. J. **276**, 114 (1984).
27. P. G. Kulikovskiĭ, *Stellar Astronomy* (Nauka, Moscow, 1985).

28. C. C. Lin, C. Yuan, and F. H. Shu, Astrophys. J. **155**, 721 (1969).

29. A. M. Mel'nik and Yu. N. Efremov, Pis'ma Astron. Zh. **21**, 13 (1995) [Astron. Lett. **21**, 10 (1995)].

30. A. M. Mel'nik, T. G. Sitnik, A. K. Dambis, *et al.*, Pis'ma Astron. Zh. **24**, 689 (1998) [Astron. Lett. **24**, 594 (1998)].

31. A. M. Mel'nik, A. K. Dambis, and A. S. Rastorguev, Pis'ma Astron. Zh. **25**, 602 (1999) [Astron. Lett. **25**, 518 (1999)].

32. Yu. N. Mishurov and I. A. Zenina, Astron. Astrophys. **341**, 81 (1998a).

33. Yu. N. Mishurov and I. A. Zenina, Astron. Zh. **76**, 563 (1999b) [Astron. Rep. **43**, 487 (1999b)].

34. Yu. N. Mishurov, E. D. Pavlovskaya, and A. A. Suchkov, Astron. Zh. **56**, 268 (1979) [Sov. Astron. **23**, 147 (1979)].

35. Yu. N. Mishurov, I. A. Zenina, A. K. Dambis, *et al.*, Astron. Astrophys. **323**, 775 (1997).

36. W. W. Morgan, S. Sharpless, and D. Osterbrock, Astron. J. **57**, 3 (1952).

37. W. H. Press, B. P. Flannery, S. A. Teukoisky, and W. T. Vetterling, *Numerical Recipes: The Art of Scientific Computing* (Cambridge Univ. Press, Cambridge, 1987).

38. A. S. Rastorguev, O. V. Durlevich, E. D. Pavlovskaya, and A. A. Filippova, Pis'ma Astron. Zh. **20**, 688 (1994) [Astron. Lett. **20**, 591 (1994)].

39. A. S. Rastorguev, E. V. Glushkova, A. K. Dambis, and M. V. Zabolotskikh, Pis'ma Astron. Zh. **25**, 689 (1999) [Astron. Lett. **25**, 595 (1999)].

40. W. W. Roberts, Astrophys. J. **158**, 123 (1969).

41. T. G. Sitnik and A. M. Mel'nik, Pis'ma Astron. Zh. **22**, 471 (1996) [Astron. Lett. **22**, 422 (1996)].

42. T. G. Sitnik and A. M. Mel'nik, Pis'ma Astron. Zh. **25**, 194 (1999) [Astron. Lett. **25**, 156 (1999)].

43. T. G. Sitnik, A. M. Mel'nik, and V. V. Pravdikova, Astron. Zh. **78**, 40 (2001) [Astron. Rep. **45**, 34 (2001)].

44. *The Hipparcos and Tycho Catalogues* (European Space Agency, 1997), Vols. 1–20.

45. P. T. de Zeeuw, R. Hoogerwerf, J. H. J. de Bruijne, *et al.*, Astron. J. **117**, 354 (1999).

Translated by A. Dambis

Infrared Photometry of Sakurai's Object (V4334 Sgr) in 2000

A. M. Tatarnikov[1], V. I. Shenavrin[1], P. A. Whitelock[2], M. W. Feast[3], and B. F. Yudin[1]*

[1] *Sternberg Astronomical Institute, Universitetskiǐ pr. 13, Moscow, 119899 Russia*
[2] *South African Astronomical Observatory, South African Republic*
[3] *Cape Town University, Cape Town, South African Republic*
Received December 29, 2000

Abstract—The infrared photometric observations of V4334 Sgr in 2000 are presented. They show that a gradual, but nonmonotonic increase in the optical depth of its dust envelope, which was formed early in 1997, had continued until the mid-summer. In July 1999 and July 2000, $\tau(1.25 \ \mu m) \approx 7.7$ and 11.3, respectively. From July through October 2000, the optical depth decreased appreciably. From October 1998 (the first deep minimum of visual brightness) until now, the amplitude of the bolometric-magnitude variations in V4334 Sgr is $\sim 0.^m5$. The relation between the bolometric and L magnitudes (m_{bol}, L) can be fitted by a linear function, $m_{bol} = 1.25L + 4.04$. In the dust-envelope model chosen, the percentage of large ($a_{gr} = 0.2–0.3 \ \mu m$) dust grains by particle number increased by a factor of ~ 4. In the summer of 2000, their fraction by mass was $\sim 78\%$, and they mainly contributed to the optical depth of the dust envelope. No appreciable correlation between optical depth and bolometric flux was observed. © 2001 MAIK "Nauka/Interperiodica".

Key words: *stars—variable and peculiar*

INTRODUCTION

On February 20, 1996, the Japanese amateur astronomer Sakurai (1996) discovered a novalike variable in Sagittarius; it was designated as V4334 Sgr and is commonly referred to as Sakurai's object. The observations of V4334 Sgr by Duerbeck and Benetti (1996) immediately after its discovery show that the star is similar to an F supergiant whose atmosphere is depleted of hydrogen and enriched with carbon and oxygen. They also detected an old planetary nebula of low surface brightness around the star. All of these findings led them to suggest that V4334 Sgr was a star that underwent the so-called final helium flash at the stage when it was already a planetary nebula nucleus (Iben 1984). After the flash, the star returns to the post-AGB track, initially moving backward along it, i.e., gradually cooling down through its expansion. Such novalike stars were called born again AGB stars (red giants), which include FG Sge, V605 Aql, and V4334 Sgr.

C_2 molecular lines were detected in the spectrum of V4334 Sgr in March 1997 (Kerber *et al.* 1997). Subsequently, CN and CO molecular lines were also detected in its spectrum (Arkhipova *et al.* 1998; Eyres *et al.* 1998). Thus, it turned into a carbon star during the winter. An infrared excess was discovered in the spectral energy distribution of V4334 Sgr in March 1997

(Kimesvenger *et al.* 1997); this excess is attributable to the condensed dust envelope.

In 1998, three minima were recorded on the optical light curve of V4334 Sgr in March, June, and October (Liller *et al.* 1998a; Jacoby and de Marco 1998; Arkhipova *et al.* 1999). The star's visual brightness at the last, deepest minimum decreased by $\sim 7^m$ relative to its 1996–1997 level. It was lower by $\sim 9^m$ in March 1999 (Jacoby 1999), by $\sim 11^m$ in July 1999 (Duerbeck *et al.* 2000), and by $\sim 13^m$ in July 2000 (Duerbeck 2000).

Previously (Tatarnikov *et al.* 2000), we presented our infrared photometric observations of V4334 Sgr during 1996–1999. Combined with optical data, they allowed us to construct its bolometric light curve and to investigate the photometric behavior of the star in detail. It turned out that the star passed through four well-defined stages in these four years as it moved along the post-AGB track. Having analyzed the spectral energy distribution of V4334 Sgr in the wavelength range 0.44–10 μm, Shenavrin and Yudin (2001) traced the evolution of its dust envelope since the beginning of its formation in 1997. We consider in detail various models of the star's structure and the nature of the deep minima in its visual light curve.

Here, we present our infrared photometric observations of V4334 Sgr in 2000. Together with the 1999 observations, they are analyzed in terms of the dust-envelope model of V4334 Sgr proposed by Shenavrin and Yudin (2000). We performed all calculations, whose numerical results are given below, in terms of

---

* E-mail address for contacts: yudin@sai.msu.su

Photometric *JHKLM* observations of V4334 Sgr at the SAAO Observatory (1) and at the Crimean Station of SAI (2)

ID 24 500 004	*J*	*H*	*K*	*L*	*M*	Observatory
1625		10.06	6.82	3.41		1
1709		10.23	7.05	3.61		1
1715		10.24*	7.06	3.60		1
1741		10.52*	7.29	3.50	2.54	2
1769		10.51*	7.29	3.45	2.53	2
1771			7.26	3.44	2.58	2
1834	13.14	9.31	6.51	3.35		1

* The measurement error is $0\overset{m}{.}1$. It does not exceed $0\overset{m}{.}07$ in *M* and less than $0\overset{m}{.}03$ in the remaining bands.

this model. It seems of importance not to put off their publication in view of the rapid evolution of this unique object, which also continued in this year.

OBSERVATIONS

The photometric *JHKLM* observations of V4334 Sgr are being carried out with the 1.9-m SAAO telescope (South Africa) and with the 1.25-m telescope at the Crimean Station of the Sternberg Astronomical Institute (SAI). Their results for 2000 are given in the table.

Figure 1 shows *V, K* magnitude and *B–V, H–L* color variations in V4334 Sgr, as well as variations in its bolometric magnitude m_{bol} and in the optical depth of its dust envelope $\tau(J)$. We used the optical observations of the following authors: Liller *et al.* (1998a, 1998b), Jacoby and de Marco (1998), Jacoby (1999), Arkhipova *et al.* (1998, 1999), Duerbeck *et al.* (2000), and, in part, amateur observers of variable stars VSOLJ (http://www.kusastro.kyoto-u.ac.jp/vsnet). Data from Tatarnikov *et al.* (2000) were used to construct the infrared light curve (1996–1999) and the bolometric light curve.

Before calculating m_{bol}, we corrected the magnitudes for interstellar reddening with the color excess $E(B–V) = 0.54$ (Duerbeck *et al.* 1997). In this way, the bolometric light curve differs from the remaining light curves in Fig. 1, which were not dereddened. Figure 2 shows the spectral energy distributions of V4334 Sgr; they characterize the spectral evolution since July 1998, when the first profound visual fading of the star began and when the bolometric flux reached its maximum (Fig. 1). We designate this time as MBOL. It is marked by an arrow (JD 2 451 007) in the (*V*, JD) and ($\tau(J)$, JD) diagrams.

The procedure for calculating the bolometric flux from V4334 Sgr was described in detail by Tatarnikov *et al.* (2000). Since March 1999, the star has emitted almost all its energy in the infrared (Fig. 2). Less than 1% of the bolometric flux can be said to have been concentrated at wavelength $\lambda \leq 1.5$ μm. When it was estimated in 2000, the *J* magnitude of V4334 Sgr, if it is lacking in the table, was calculated from $J = 1.72H - 2.87$. This expression has fitted well the observed (*J, H*) relation from October 1998 [the first deep minimum of visual brightness (FDM)] until now. In the (*V*, JD) and

($\tau(J)$, JD) diagrams, the time of FDM is marked by an arrow (JD 2 451 094).

We estimated the star's *M* and *N* magnitudes by using the relations $L - M \approx 0.91$ (the mean in 2000; see the table) and $M - N \approx 1.3$ (the mean in 1999; see Tatarnikov *et al.* 2000). Note that no more than 5% of the bolometric flux is concentrated at wavelength $\lambda \geq 11$ μm. Therefore, if we change the *N* magnitude, say, by $0\overset{m}{.}3$, the bolometric flux will change by ≤2%.

In general, analyzing the possible errors that arise when extrapolating and integrating the spectral energy distribution of V4334 Sgr, we can say that the errors in the bolometric magnitude given in the table apparently do not exceed $0\overset{m}{.}1$.

DISCUSSION

In 2000, the variability amplitude of m_{bol} was $\sim 0\overset{m}{.}3$, and the bolometric flux from V4334 Sgr was on average higher than that in 1999. The peak-to-peak variability amplitude of m_{bol} is $\sim 0\overset{m}{.}5$ since FDM and $\sim 1^m$ since MBOL (Fig. 1). Note that this conclusion is also valid when the interstellar reddening is increased, say, to $E(B–V) = 0.8$ (Arkhipova *et al.* 1999), because $\sim 85\%$ of the bolometric flux was concentrated in the infrared even in July 1998.

Figure 3 shows the (m_{bol}, *L*) and (*H–L*, *L*) diagrams constructed from our observations of V4334 Sgr since FDM, when the dust envelope reached a sufficient optical depth [$\tau(J) \approx 3.6$]. We see from this figure that there is a clear correlation between m_{bol} and *L* and that the relation between these parameters can be fitted by a linear function, $m_{bol} = 1.25L + 4.04$. Model calculations indicate that the *L* magnitude of a star surrounded by an optically thick [$\tau(J) = 3–10$] dust envelope is a sensitive indicator of its luminosity variations. At the same time, the *L* magnitude responds weakly to variations in the optical and geometric depths of the dust envelope. It is not sensitive to the grain size either.

This is illustrated in Fig. 3. The straight-line segment in the (m_{bol}, *L*) diagram shows how much the *L* magnitude of the model will change when m_{bol} changes by $0\overset{m}{.}4$. In this case, the dust-envelope parameters were
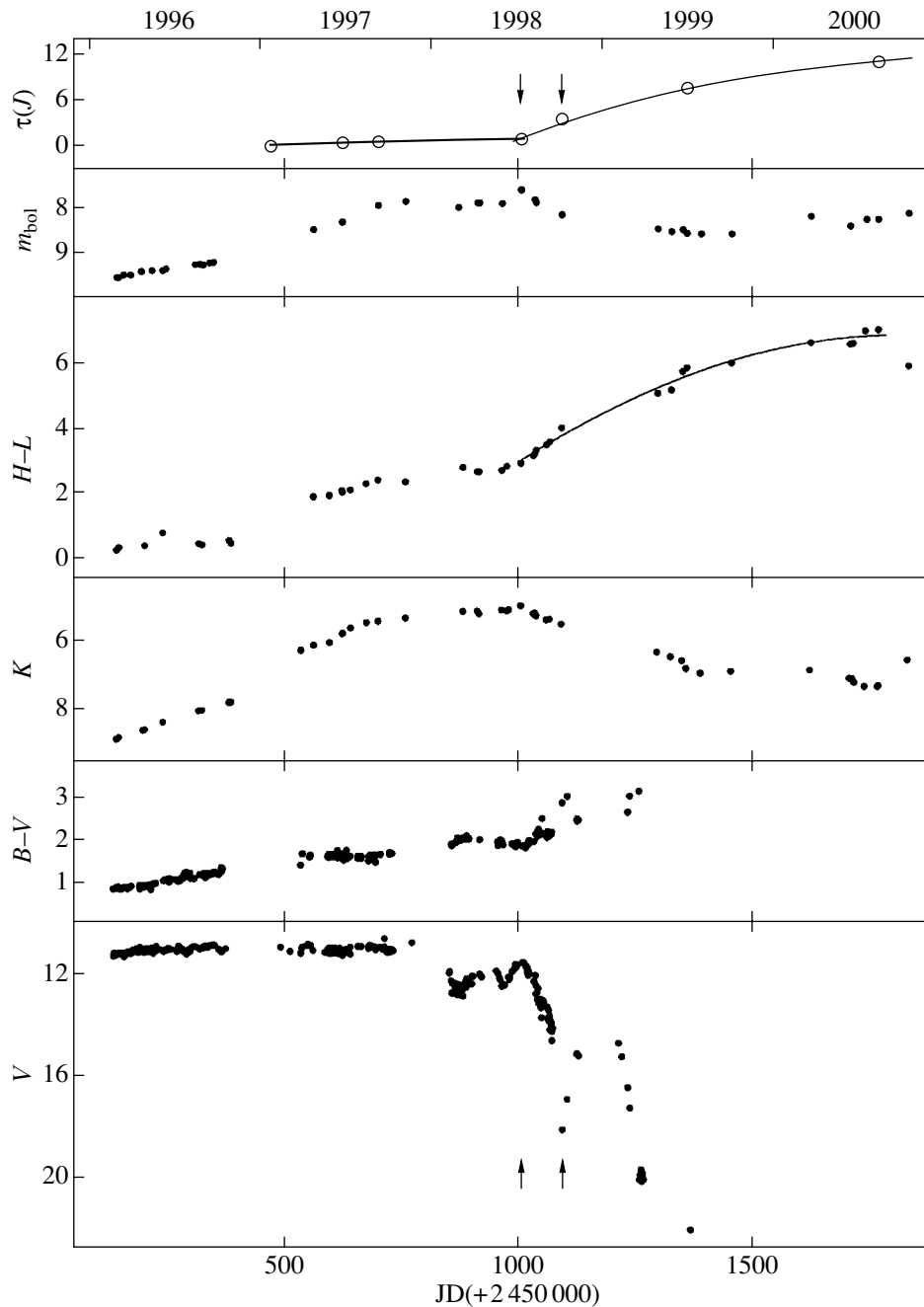
Fig. 1. Variations in the *V* and *K* magnitude, *B–V* and *H–L* color, and bolometric magnitude m_{bol} of V4334 Sgr and in the optical depth $\tau(J)$ of the dust envelope during 1996–2000. In the (*V*, JD) and ($\tau(J)$, JD) diagrams, the arrows mark the times of MBOL (JD 2 451 007) and FDM (JD 2 451 094). In the (*H–L*, JD) diagram, the solid line represents the second-degree polynomial that fits this relation in the corresponding time interval. In the ($\tau(J)$, JD) diagram, the solid line represents the computed relation between these parameters.

constant and generally similar to the parameters of the dust envelope around V4334 Sgr at the time of FDM (Shenavrin and Yudin 2001).

The polygonal line in the (*H–L*, *L*) diagram indicate changes in these parameters when either only the optical depth of the dust envelope changes from $\tau(J) = 3.6$ to 7.7 (almost vertical segment) or only m_{bol} changes by $0\overset{m}{.}4$ (almost horizontal segment). Note that the dust

envelope of V4334 Sgr had the latter value of $\tau(J)$ in July 1999 (see below). Thus, the *H–L* color index of the object (central star + dust envelope) is a sensitive indicator of variations in the optical depth of the dust envelope and responds weakly to variations in the luminosity of the central star. We see from Fig. 3 that the *H–L* color does not correlate with the *L* magnitude. Consequently, the optical depth of the dust envelope does not correlate with the stellar luminosity.
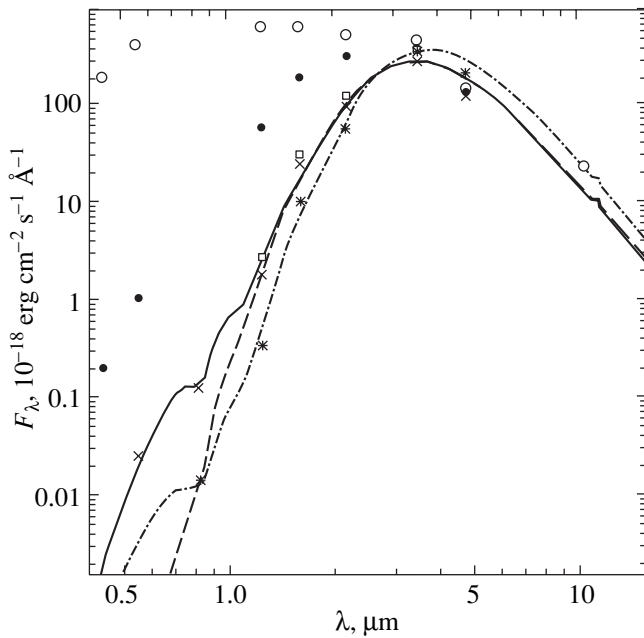
Fig. 2. The spectral energy distribution of V4334 Sgr in July 1998 (circles), October 1998 (dots), July 1999 (crosses), August 2000 (asterisks), and October 2000 (squares). The solid, dashed, and dash-dotted line represent the computed energy distributions in models 99M1, 99M2, and 00M1, respectively.

Fig. 3. The $(L, H–L)$ and (m_{bol}, L) diagrams for V4334 Sgr from the first deep minimum of its visual brightness in October 1998. The dashed line is a first-degree polynomial fit to the (m_{bol}, L) relation. The solid lines indicate the corresponding functional dependences in the models discussed in the text.

We plotted the first five points in the $(\tau(J), JD)$ diagram (Fig. 1), which trace the evolution of the optical depth of the dust envelope from the onset of its condensation in January 1997 until FDM, by using data from Shenavrin and Yudin (2001). Subsequently, based on the condition that the rate of dust condensation at the inner radius of the dust envelope was constant from the beginning of its formation $(0, 2\,450\,470)$ until MBOL $(1, 2\,451\,007)$, we calculated the $(\tau(J), JD)$ relation. The almost horizontal segment of the solid line corresponds to it in the $(\tau(J), JD)$ diagram. The rate of condensation was found to be $M_{dust} \approx 3.5 \times 10^{-8} M_\odot$ yr^{-1}.

As we see from the $(\tau(J), JD)$ diagram, the points for 1997 also lie almost on the calculated curve. Therefore, we can apparently take $M_{dust} \approx 3.5 \times 10^{-8} M_\odot$ yr^{-1} as the mean rate of increase in dust-envelope mass in the time interval under consideration. The ensuing first profound visual fading of V4334 Sgr was clearly attributable to an appreciable increase in M_{dust}.

Figure 2 shows the spectral energy distribution of V4334 Sgr in July 1999. Its visual and infrared observations were carried out on July 8 (Duerbeck *et al.* 2000) and July 1 (Tatarnikov *et al.* 2000), respectively. Computed energy distributions for these dates are indicated in Fig. 2 by the solid (model 99M1) and dashed (model 99M2) lines. In model 99M2, the percentage of grains with radii $a_{gr} = 0.05, 0.1$, and 0.25 μm is the same as that in the model of Shenavrin and Yudin (2001) (see the same paper for the details of calculations), which reproduces the star's spectral energy dis-
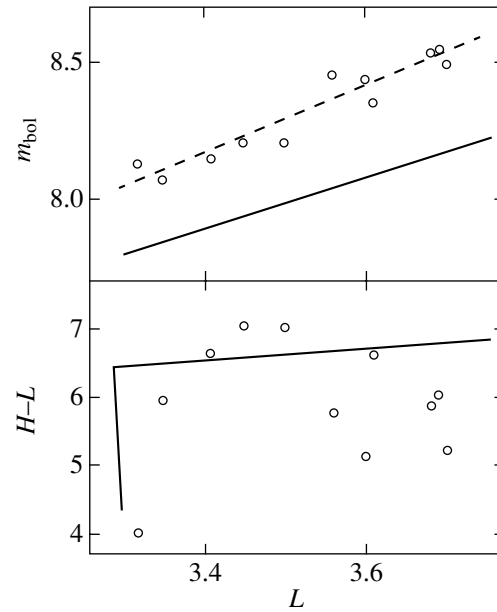
tribution at FDM: by particle number (mass), 85% (25%), 13.8% (32%), and 1.2% (43%), respectively. In model 99M1, it is 85% (17%), 12.5% (20%), and 2.5% (63%) by particle number (mass); i.e., in this model, the percentage of large ($a_{gr} = 0.25$ μm) grains is a factor of ~2 higher than that in model 99M2. The remaining input parameters in models 99M1 and 99M2 are the same.

In particular, the geometric structure of the dust envelope is such a parameter. It consists of two layers with an abrupt change in density at their boundary. The formation of the first (outer) layer with a mean rate of condensation $M_{dust} \approx 3.5 \times 10^{-8} M_\odot$ yr^{-1} completed at MBOL; subsequently, it expanded without any change in its thickness. Its parameters correspond to the parameters of the dust-envelope model calculated for this time (Shenavrin and Yudin 2001). Subsequently, the rate of grain condensation at the inner boundary of the dust envelope increased sharply, which gave rise to the first deep minimum on the visual light curve of V4334 Sgr and, in the dust-envelope model, to an abrupt change in density in the radial dust distribution. The thickness of this second (inner) layer increased with time. The ratio of its thickness to the inner radius of the dust envelope, $\Delta R_{env,\,in}/R_{in}$ was ≈0.5 in July 1999 and ~1.1 in July 2000.

The dust envelope in models 99M1 and 99M2 has the same optical depth at a wavelength of 1.25 μm, $\tau(J) = 7.7$. However, because of the different percentages of large grains (in the former model, it is a factor

of ~2 higher than that in the latter), the optical depth of the dust envelope at a wavelength of 0.55 μm in these models is $\tau(V) \approx 12.0$ and 18.1, respectively, which is reflected in the star's visual brightness (Fig. 2).

Calculations show that the change in optical depth of the dust envelope when the percentage of its medium-sized ($a_{gr} = 0.1$ μm) grains changes is insignificant; i.e., the effect of increase in the object's visual brightness is marginal. In this regard, large grains are of a fundamental importance. At the same time, if we replace $a_{gr} = 0.25$ μm grains with $a_{gr} = 0.5$ μm grains, we will then be unable to fit the computed energy distribution to the observed energy distribution in the infrared. Thus, 0.2–0.3-μm grains can be said to have played a dominant role by mass in the inner envelope of V4334 Sgr in the summer of 1999.

We see from Fig. 2 that models 99M1 and 99M2 have the same brightness at 3.5 μm (*L* band). In other words, as was already pointed out above, the *L* brightness of a star surrounded by a sufficiently dense dust envelope is insensitive to the percentage of grains of different sizes. This is because for the wavelength in question, Rayleigh approximation can be used even for large grains. In this approximation, the absorption coefficient of the particle does not depend on its radius and is entirely determined by the refractive index of the matter.

The optical depth of the inner layer accounts for ~92% of the total optical depth of the dust envelope. Its mass in models 99M1 and 99M2 is $M_{dust} \approx 2.0 \times 10^{-7} M_{\odot}$ and ~2.4 × 10$^{-7}M_{\odot}$, respectively. The small optical depth of the outer layer of the dust envelope is reflected in the fact that its radiation is essentially unnoticeable against the radiation from the inner layer. It is completely lost in the summer of 2000. Its reliable detection requires mid- and far-infrared observations of the star.

In Fig. 2, the asterisks indicate the spectral energy distribution of V4334 Sgr in July 2000. Its visual and infrared observations were carried out on July 18 (Duerbeck 2000) and July 15 (JD 2451741 in the table), respectively. The dash-dotted line represents the computed energy distribution (model 00M1). The model parameters are the following: $\tau(J) = 11.3$, the inner layer accounts for ~96% of the optical depth of the entire envelope, its mass is $M_{dust} \approx 4.0 \approx 10^{-7}M_{\odot}$, and the percentage of its grains with sizes of 0.05, 0.1, and 0.25 μm by particle number (mass) is 83% (10%), 12% (12%), and 5% (78%), respectively. Thus, from the summer of 1999 until the summer of 2000, the mass of the inner layer doubled, and the percentage of its large grains by particle number tripled.

In the ($\tau(J)$, JD) diagram (Fig. 1), we constructed the curve that passes through the points (1, 2451007) and (7.7, 2451361) based on the model of a two-layer dust envelope, in which the rate of grain condensation at the inner radius abruptly increased at MBOL (1, 2451007) and was subsequently constant. This parameter was found to be $\dot{M}_{dust} \approx 2.0 \times 10^{-7}M_{\odot}$ yr^{-1}; i.e., it

was a factor of ~5.7 higher than its value before MBOL. As we see from the ($\tau(J)$, JD) diagram, the points for October 1998 (FDM) and July 2000 (model 00M1) are located near this curve. Consequently, from the summer of 1998 until the summer of 2000, the mass of the dust envelope can be said to have increased approximately at a constant rate.

In the (*H–L*, JD) diagram (Fig. 1), the solid line indicates the second-degree polynomial that satisfactorily fits this relation in the above time interval. Since the *H–L* color index is a sensitive indicator of the optical thickness of the dust envelope, the optical depth can be said to have increased smoothly.

We see from Fig. 1 that the *H–L* color index decreased appreciably from July until October 2000. This, in turn, means that the optical depth of the dust envelope also decreased appreciably. In October 2000, *H–L* returned to its July 1999 value (Fig. 1). At the same time, the bolometric flux in October is a factor of ~1.5 higher than that in July (Fig. 2). Therefore, one might expect the visual brightness of V4334 Sgr in October 2000 to have been higher than 22^m.

CONCLUSION

Our observations of V4334 Sgr in 2000 have shown that the star is still at the protracted deep minimum of its visual brightness attributable to permanent grain condensation at the inner boundary of the dust envelope. Until the mid-summer of 2000, its optical depth had increased gradually, but nonmonotonically to its maximum $\tau(J) \approx 11.3$, which was reached in July. From July through October, the optical depth decreased appreciably. Subsequent observations will show whether this phenomenon can be considered temporary.

The variability amplitude of the bolometric magnitude from the beginning of the first profound visual fading of V4334 Sgr in July 1998 is ~1^m. Since there is every reason to believe that the observed bolometric flux corresponds to the star's bolometric luminosity (Tatarnikov *et al.* 2000; Duerbeck *et al.* 2000), we can say that at this stage of its evolution, its bolometric luminosity changed by a factor of ~2.5 without correlating with the optical depth of the dust envelope.

Since the first deep minimum of visual brightness of V4334 Sgr in October 1998, when the dust envelope gained a large optical depth ($\tau(J) \approx 3.6$), the object's *L* magnitude has been an indicator of variations in its bolometric flux: $m_{bol} = 1.25L + 4.04$.

The model of a two-layer dust envelope, in which each layer is formed with a constant rate of dust condensation (M_{dust}) at the inner boundary of the dust envelope, satisfactorily reproduces the rate of increase in its mass, at least until the mid-summer of 2000. The second, denser layer began to form in July 1998 through an approximately fivefold increase in $\dot{M}_{dust}$, from ~3.5 × 10^{-8} to ~2.0 × 10$^{-7}M_{\odot}$ yr^{-1}.

In July 1999 and July 2000, the optical depth of the inner layer accounted for ~92 and ~96% of the optical depth of the entire envelope, respectively. From October 1998 through July 2000, the fraction of its large ($a_{gr} = 0.2$–0.3 μm) grains by particle number increased by a factor of ~4. Their fraction by mass was ~78%.

The increase in the fraction of large particles is reflected in the fact that the visual optical depth of the dust envelope increases more slowly than does the infrared one. This causes a slower decline in the visual brightness of V4334 Sgr than might be expected in the case where the dust envelope is filled with particles with $a_{gr} \leq 0.1$ μm.

REFERENCES

1. V. P. Arkhipova, V. F. Esipov, R. I. Noskova, *et al.*, Pis'ma Astron. Zh. **24**, 297 (1998) [Astron. Lett. **24**, 248 (1998)].
2. V. P. Arkhipova, R. I. Noskova, V. F. Esipov, and G. V. Sokol, Pis'ma Astron. Zh. **25**, 711 (1999) [Astron. Lett. **25**, 615 (1999)].
3. H. W. Duerbeck, private communication (2000).
4. H. W. Duerbeck and S. Benetti, Astrophys. J. Lett. **468**, L111 (1996).
5. H. W. Duerbeck, S. Benetti, A. Gautschy, *et al.*, Astron. J. **114**, 1657 (1997).
6. H. W. Duerbeck, W. Liller, C. Sterken, *et al.*, Astron. J. **119**, 2360 (2000).
7. S. P. S. Eyres, A. Evans, T. R. Geballe, *et al.*, Mon. Not. R. Astron. Soc. **298**, L37 (1998).
8. I. Iben, Astrophys. J. **277**, 333 (1984).
9. G. Jacoby, IAU Circ., No. 7155 (1999).
10. G. Jacoby and O. de Marco, IAU Circ., No. 7065 (1998).
11. F. Kerber, H. Gratl, and M. Roth, IAU Circ., No. 6601 (1997).
12. S. Kimesvenger, H. Gratl, F. Kerber, *et al.*, IAU Circ., No. 6608 (1997).
13. W. Liller, M. Janson, H. W. Duerbeck, and A. van Genderen, IAU Circ., No. 6825 (1998a).
14. W. Liller, H. W. Durbeck, A. van der Meer, and A. van Genderen, IAU Circ., No. 7049 (1998b).
15. Yu. Sakurai, IAU Circ., No. 6322 (1996).
16. V. I. Shenavrin and B. F. Yudin, Astron. Zh. **78** (8) (2001) (in press) [Astron. Rep. **45** (8) (2001) (in press)].
17. A. M. Tatarnikov, V. I. Shenavrin, B. F. Yudin, *et al.*, Pis'ma Astron. Zh. **26**, 587 (2000) [Astron. Lett. **26**, 506 (2000)].

Translated by V. Astakhov

Close Binary Systems in Star-Forming Regions: BZ Mon in the OB Association Mon OB2

M. M. Zakirov*

Astronomical Institute, Academy of Sciences of Uzbekistan, Astronomicheskaya ul. 33, Tashkent, 700052 Uzbekistan
Received January 9, 2001; in final form, March 19, 2001

Abstract—Photoelectric *UBVR* observations of the eclipsing variable early-type star BZ Mon are presented. A new ephemeris of its minima was determined: Min I = JDH 2451 121.294(14) + $3^{d}.4518062(94) \times E - (172 \pm 13)^{d} \times 10^{-10} \times E^{2}$. Brightenings by several hundredths of a magnitude, particularly pronounced in the red, are observed at maximum light. We solved all light curves by Lavrov's method and obtained highly accurate photometric orbital elements of the system. The positions of its components are analyzed in two-color (*U–B*), (*B–V*) and (*U–B*), (*V–R*) diagrams. The spectral types of the hot and cool stars are B5 V and G2 III, respectively. The cool component exhibits an ultraviolet excess of $0^{m}.15$. Fundamental parameters of the components were estimated: $M_{h} = 4.90 M_{\odot}$, $M_{c} = 2.70 M_{\odot}$, $R_{h} = 3.25 R_{\odot}$, and $R_{c} = 5.20 R_{\odot}$. The age of the stars is 3×10^{5} years. The binary is a member of the OB association Mon OB2. © 2001 MAIK "Nauka/Interperiodica".

Key words: *stars—variable and peculiar*

INTRODUCTION

The eclipsing variable BZ Mon (=63.1936, *m* = 12.1–15.4 pg) was discovered by Hoffmeister (1936). Visual and photographic observations yielded basic data on the light curve of this binary system (Ahnert 1943; Ahnert *et al.* 1947; Kordilewski 1959; Schaefer 1980). The most comprehensive information on BZ Mon was obtained by Schaefer (1980), who performed about a hundred visual observations of the variable during 1977–1978 and supplemented these data with more than 500 photographic estimates on plates of the Harvard Observatory taken since 1900. This author managed to improve the ephemeris of primary minima for BZ Mon, which were included in the General Catalog of Variable Stars:

$$\text{Min I} = \text{JDH} 2\,443\,192.663 + 3^{d}.451804 \times E.$$

The eclipse duration at primary minimum was $0^{p}.06$, and the brightness was at a standstill for $0^{p}.030$ at the minimum. No fading was detected at a secondary minimum. In the Palomar Observatory Sky Atlas, the exposure time of blue and red photographs coincided with the epoch of the variable's primary minimum; Schaefer (1980) determined the binary's color index $B–V = 0^{m}.82 \pm 0^{m}.10$, which belongs to its cool component. (Recall that a total eclipse occurs at primary minimum, and only the faint component is seen.) He found the color index of the hot component to be $B–V = -0^{m}.28 \pm 0^{m}.15$. He also estimated the expected spectral types of the components as B4 V and G5 III.

The variable is seen in the region of the OB association in Monoceros. Semeniuk (1962) believed that it was only projected onto the region of the Mon I association and was not its member. Sahade and Beron (1963) did not rule out the possibility that BZ Mon belongs to the open cluster Cr 106 (the star lies at a distance of three angular radii of the cluster from its center). BZ Mon and the OB association Mon OB2 turned out to be close in distance (Schaefer 1980).

The star was included in the catalog of approximate absolute and photometric elements of eclipsing variables by Svechnikov and Kuznetsova (1990).

OBSERVATIONS

Photoelectric *UBVR* observations of BZ Mon in Johnson's system were begun in 1989 with the 60-cm telescope and continued in 1998–1999 with the 1-m and 60-cm Maidanak Observatory telescopes. Most (more than 90%) observations of the variable were obtained with the 1-m telescope in 1998. We used the monthly mean atmospheric extinction coefficients at Mount Maidanak (Zheleznyakova 1984) to reduce our measurements. On good photometric nights, when the airmass difference of the comparison star during the night exceeded 0.5, we determined the extinction coefficients by Bouguer's method. The magnitudes and colors of the comparison (BD + 5°1333) and check stars

* E-mail address for contacts: mamnun@astrin.uzsci.net

Table 1. Photometric quantities for the reference stars

Star	V	$U–B$	$B–V$	$V–R$	Sp
Comparison BD + 5°1333	8.095 ± 0.002	0.483 ± 0.009	0.852 ± 0.001	0.703 ± 0.002	K0
Check	12.524 ± 0.012	0.035 ± 0.010	0.674 ± 0.016	0.600 ± 0.011	B5–6*

* We estimated the star's spectral type in the two-color ($U–B$), ($B–V$) and ($U–B$), ($V–R$) diagrams.

Table 3. A summary of orbital-period determinations for BZ Mon

Author	Observing interval JD 2 400 000+	Number of passed periods	Number of known minima	Period, days
Ahnert *et al.* (1947)	27 100–29 316	642	5	3.4517021
Kordilewski (1959)	27 100–29 316	642	5	3.452002
Schaefer (1980)	27 100–43 544	4764	8	3.451804 ± 0.00030
Borovička (1995)	27 100–48 922	6322	16	3.451721 ± 0.000100
Pascke (personal communication)	27 100–51 138	6964	18	3.451755

were determined relative to the photometric standard SA 97 (Landolt 1983). To minimize the correction for atmospheric extinction, we measured the reference stars and the standard area at close airmasses. Our results are given in Table 1. The check star lies $1'.5$ south of the comparison star; we determined its coordinates by using the standard MEGASTAR code: $\alpha_{2000} = 6^h37^m35^s$ and $\delta_{2000} = +4°53'54''$.

Over the entire period of our observations of BZ Mon, we obtained 384, 377, 369, and 388 measurements in U, B, V, and R, respectively (Table 2[1]). The error of a single photometric measurement for the variable at maximum was $\pm0^m.012$ in U, $\pm0^m.012$ in B, $\pm0^m.013$ in V, and $\pm0^m.028$ in R.

ORBITAL PERIOD

The reduction of our observations of BZ Mon using the above ephemeris shows that the minima in 1998 occurred earlier by $0^d.179$. In 1989, we failed to trace the minima, but the available observations of the ascending branch of the primary minimum indicate that the minimum does not coincide with the ephemeris. The 1999 observations covered only phases outside eclipse.

The period determinations for BZ Mon by different authors are summarized in Table 3. Although the observing interval of the variable increased, the accuracy of determining the period did not increase significantly.

To refine the light elements of BZ Mon, we used all the available reliably observed epochs of maximum fading of the close binary system (CBS). In our analysis, we also included the observations of minima published in BBSAG (Bedeckungsveranderlichen Beobachter der Schweizerichen Astronomischen Gesell-

shaft) bulletins. The linear fitting of the epochs of CBS minima yielded a period that matched the period determined by Schaefer (1980), but the initial epoch was displaced by $0^d.101$. Figure 1 shows a diagram of $O–C$ residuals to this ephemeris. There is a large gap between the observations of Ahnert *et al.* (1947) and Schaefer (1980), and we do not know the behavior of $O–C$ residuals in this time interval. If the $O–C$ variations in this interval is assumed to be parabolic, then they can be represented by the formula

$$\mathrm{Min\,I} = \mathrm{JDH}\,2427369.415(13) + 3^d.4519278(88) \times E - (178 \pm 12) \times 10^{-10} \times E^2.$$

In Fig. 1, the $O–C$ residuals are fitted by this formula, and Table 4 gives deviations of the epochs of minima. Since JD 2 443 192, the observations of minima have pointed to a parabolic law of period variations. We fitted the epochs of minima by a quadratic function, which provided the best fit to the 1988 and 1998 observations, including Schaefer's observations (personal communication), and obtained the following ephemeris:

$$\mathrm{Min\,I} = \mathrm{JDH}\,2451121.278 + 3^d.4518062 \times E - (172 \pm 13)^d \times 10^{-10} \times E^2. \atop \pm 0.014 \ \pm 0.0000094.$$

The $O–C$ residuals to this ephemeris are given in Table 4. The time of observation of the minimum JD 24 100.373 was excluded from our analysis because of the large deviation from the remaining values.

A detailed analysis of the epochs of minima for BZ Mon shows that its orbital period can undergo small abrupt changes and that its general behavior can be represented as a parabola, at least in the last sixty years.

THE LIGHT CURVE AND ITS SOLUTION

The light curve of BZ Mon constructed from the new ephemeris (5) is shown in Fig. 2. The secondary
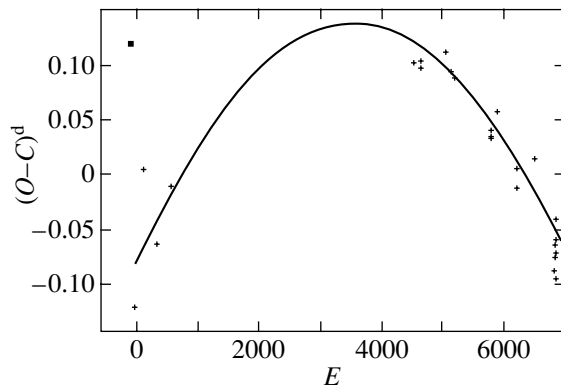
Fig. 1. A diagram of *O–C* residuals to the linear ephemeris and its parabolic fit (solid line). The square represents the observation of Ahnert *et al.* (1947) excluded from the analysis of light elements.

minimum is very shallow, and it is clearly seen only on the *V* and *R* light curves. The eclipse duration at primary minimum is $0\overset{p}{.}13$, and the brightness is at a standstill for about $0\overset{p}{.}006$, which is a factor of 5 shorter than the value estimated by Schaefer (1980). Photometric

Table 4. Epochs of minima and *O–C* residuals for BZ Mon

Source	JDH 2400000+	*E*	$(O–C)^{\mathrm{d}}$
Ahnert *et al.* (1947)	27100.373	−78	(+0.209)
	27369.373	0	−0.042
	27842.395	137	+0.066
	28629.339	365	−0.027
	29316.302	564	+0.005
Schaefer (1980)	43192.663	4584	−0.014
	43482.615	4668	−0.010
	43544.739	4686	−0.017
BBSAG	44911.669	5082	+0.018
BBSAG	45308.609	5197	+0.008
BBSAG	45398.349	5223	0.002
Borovička (1995)	47538.415	5843	−0.004
	47538.416	5843	−0.003
	47538.421	5843	0.002
BBSAG	47859.454	5936	+0.025
BBSAG	48922.557	6244	0.001
Borovička (1993)	49005.384	6268	−0.013
BBSAG	49999.528	6556	+0.042
This paper	51107.467	6877	−0.011
	51110.932	6878	+0.003
	51114.359	6879	−0.022
	51121.291	6881	+0.007
	51124.753	6882	+0.017
	51128.182	6883	−0.006
	51131.611	6884	−0.027

magnitudes at the main phases of the light curve are listed in Table 5. We also included the data of Schaefer (personal communication) in this table. This author observed the star in Kron–Causins's *RI* system, and we recalculated the color indices to Johnson's system by using formulas from Landolt (1983). As we see from Table 5, some of the results differ by as much as $0\overset{m}{.}08$ (the amplitude of primary minimum). These differences may be real, or they may result from the use of different photometric standards.

The light curve of BZ Mon exhibits an interesting feature detectable in all its segments outside eclipse and near the secondary minimum, which is particularly pronounced in *V* and *R*: a brightening by several hundredths of a magnitude. The same phenomena may occur at primary minimum, but they are undetectable in the rapidly changing segments of the light curve. We carefully checked the comparison star for possible variability against the check star and against the comparison stars of other program stars observed at close times. The comparison star maintained a constant brightness to within $0\overset{m}{.}02$ in *U* (and even less in other bands) over the entire observing period in 1998. In other years, the number of data points was too small to detect the brightenings noted above. If these brightenings are attributable to flares and if the flares themselves are similar to solar prominences, then their source can be an active cool component of spectral type G5 III. Red flares were observed on several stars (Zakirov 1993, 1996).

We solved the light curve of BZ Mon by using the code of Lavrov (1993), which is based on Russell–Merrill's rectifiable model. Limb-darkening coefficients of the stars were taken from Rubashevskiĭ (1985). We brought all our 1989 and 1998 observations into the closest coincidence in phase. A total eclipse occurs at primary minimum, and we see the large cool component alone. The derived photometric orbital elements are listed in Table 6. The parameters of the large, cool and small, hot components are denoted by the subscripts "c" and "h," respectively. The relative radii of the components are in units of the orbital semimajor axis, and the brightness is in units of $L_{\mathrm{h}} + L_{\mathrm{c}}$.

Column 6 gives the color-averaged geometric orbital elements, and column 7 lists the photometric orbital elements as inferred by Svechnikov and Kuznetsova (1990); the latter were obtained from the photographic light curve by using statistical correlations between fundamental stellar parameters. A comparison of the photometric orbital elements estimated by these authors with our estimates shows good agreement between all parameters except for the orbital inclination to the line of sight. The last row gives the rms deviations of a single normal point from the corresponding theoretical light curve.

Table 5. Photometric parameters of the light curve for BZ Mon

Phase	This paper				Schaefer (private communication)				
	V	$U–B$	$B–V$	$V–R$	V	$U–B$	$B–V$	$V–R$	$R–I$
Max	12.11	−0.21	0.37	0.43	12.11	−0.20	0.39	0.50	0.29
Min I	14.19	0.54	0.99	0.92	14.27	0.51	1.06	0.95	0.66
Min II	12.17	−0.16	0.36	0.38	12.18				

DISCUSSION

We discuss the above data by following the scheme outlined by Zakirov (1996). The results of our photometry and light-curve solution for BZ Mon allow the photometric magnitudes of each component to be calculated separately (Table 7). These calculations were performed by using the standard procedure with allowance for the reflection effect; the required quantities are determined by the code of Lavrov (1993). The accuracy of determining the magnitudes for the hot component proved to be less than $0\overset{m}{.}01$ in all bands. In the two-color ($U–B$), ($B–V$) and ($U–B$), ($V–R$) diagrams, the high-temperature component is unambiguously characterized by the spectral type B5 (Fig. 3), while the cool component crosses the standard curves at three points. We considered the stars' positions in these diagrams by using the recommendations of Straĭzys (1977). In the two-color diagrams constructed for the giant branch [Schaefer (1980) classified the cool component of the CBS as belonging to G5 III], the star crosses the standard curves near G1. We will make the final choice of the spectral type for the cool component after discussing its possible fundamental parameters.

The photometric magnitudes of the low-temperature component (Table 7) turned out to be close to the CBS magnitude at primary minimum (Table 5) in U, B, and V, as expected for a total eclipse (the magnitude differences are less than $0\overset{m}{.}01$).

We estimate the mass and radius of the cool component of the CBS by assuming tabulated values of these quantities for its primary B5 V star (Straĭzys 1982). The radius of the low-temperature component can be determined from the ratio of the stars' photometric radii. The mass of this component can be estimated from Kepler's third law; assuming that $M_\mathrm{h} = 4.90 M_\odot$, we find $M_\mathrm{c} = 2.70 M_\odot$. Possible absolute parameters of the components of BZ Mon were considered in the Hertzsprung–Russell (H–R) diagrams for evolving stars of various masses. We analyzed the positions of the CBS components in the H-R diagrams for single stars both after they left the zero-age main sequence (ZAMS) (Maeder 1976; Maeder and Mermilliod 1981) and evolving toward the ZAMS (Palla and Stahler 1993). The best agreement between the fundamental parameters of the CBS components was achieved in the H–R diagram for pre-ZAMS stars (Fig. 4). In this case, as a check on internal agreement between the quantities, we used the ratio of stellar radii, the sum of masses according to

Kepler's third law, and the difference between the visual magnitudes of the components (Table 7) and the theoretical absolute magnitudes calculated from the stellar radii and temperatures with allowance for bolometric corrections. The basic physical quantities of the components of BZ Mon estimated in this way are given
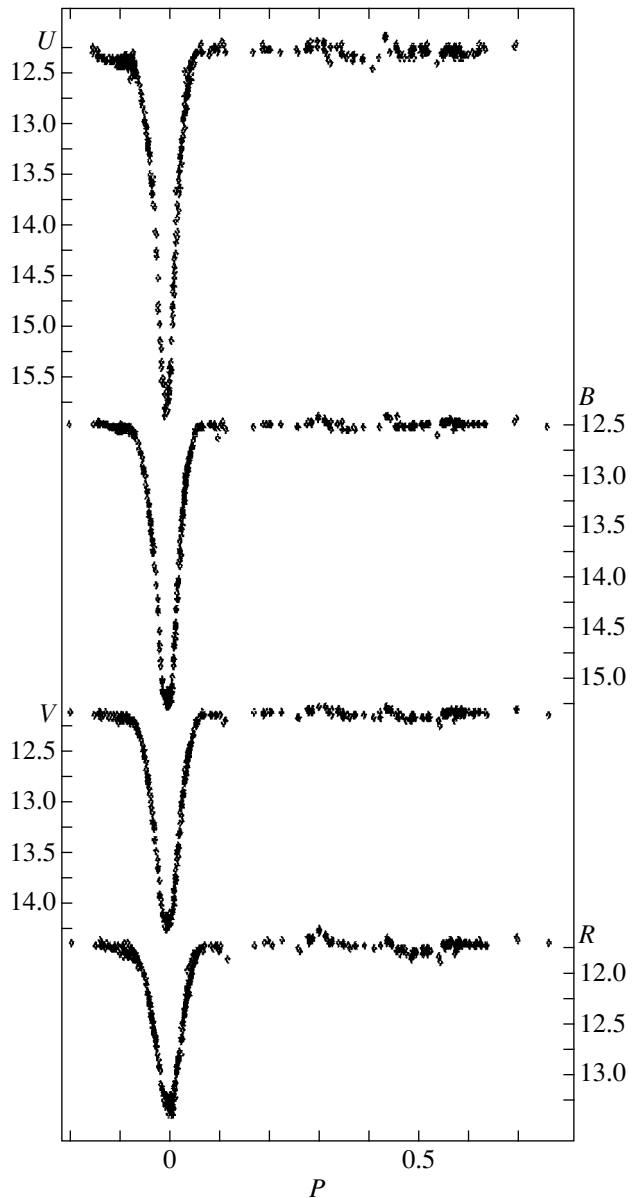

Fig. 2. Light curves of the eclipsing variable BZ Mon.

Table 6. Photometric orbital elements for BZ Mon

Parameter	U	B	V	R	$\langle UBVR \rangle$	Svechnikov and Kuznetsova (1990)
r_c	0.270	0.268	0.274	0.284	0.274 ± 0.004	0.267
r_h	0.172	0.172	0.167	0.176	0.172 ± 0.002	0.150
x_c	0.98	0.86	0.70	0.58		
x_h	0.54	0.55	0.45	0.36		
i^0	84.4	84.8	83.6	82.4	83.8 ± 0.5	90
L_c	0.050 ± 0.0001	0.092 ± 0.001	0.157 ± 0.004	0.210 ± 0.015		0.07
σ^m	0.032	0.027	0.030	0.027		

in Table 8. As was pointed out by the referee, the mass of the cool component estimated from Kepler's third law is unreliable, because it is proportional to the cube of the orbital radius. However, the interconsistency between the above quantities gives hope that the mass estimate of this component is realistic. A comparison of our quantities with those of Svechnikov and Kuznetsova (1990) reveals large discrepancies because of the difference in the stars' spectral types. Both CBS components fall nicely on the 3×10^5-year isochrone (Fig. 4), which also confirms that the estimates of the CBS fundamental parameters are valid. The cool component is near the birth line of stars. The time it takes for a star of mass M_* to contract to the main sequence can be estimated from the following formula (Masevich and Tutukov 1988):

$$\tau \approx 5 \times 10^7 (M_\odot / M_*) \text{ years.}$$

The massive and cool components of BZ Mon will reach the main sequence in 9×10^5 and 4×10^6 years, respectively.

Table 7. Photometric quantities for the components of BZ Mon

Component	V	$U–B$	$B–V$	$V–R$
Hot	12.30 ± 0.01	-0.22 ± 0.00	0.28 ± 0.01	0.33 ± 0.02
Cool	14.20 ± 0.03	0.54 ± 0.02	0.99 ± 0.03	0.77 ± 0.08

Table 8. Absolute parameters for the components of BZ Mon

Parameter	Hot component		Cool component	
	this paper	Svechnikov and Kuznetsova (1990)	this paper	Svechnikov and Kuznetsova (1990)
$M/M_\odot$	4.90	2.25	2.70	0.60
$R/R_\odot$	3.25	2.0	5.20	3.6
M_{bol}	-2.10	1.35	$+1.32$	3.05
T_e, K	15490		6135 ± 30	
Sp	B5 V	A2	G2 III	K2 IV

We found the spectral type of the cool component to be G2 III, which is similar to its spectral type determined in the two-color diagrams (G1). If we wish to reconcile the spectral type of the cool star inferred from its estimated fundamental parameters with its position in the two-color diagrams, then we will have to assume that it has an ultraviolet excess, $\delta(U–B) = -0^m14 \pm 0^m02$ (Fig. 3). Given the cool component's color error in these quantities (Table 7), agreement with the temperatures in Table 8 can be achieved. Analyzing the eclipse depth at the primary minimum of BZ Mon and the normal colors of the CBS components, we can confirm that the spectral type of the cool component is G2 III.

To this end, we plot the difference between the amplitude of primary minimum in different bands and the depth of the minimum in the visual range against wavelength. To extend the spectral range, we use Schaefer's *UBVRI* photometry (Table 5). At primary minimum, a total eclipse occurs and the system's brightness corresponds to the cool component. We calculate the photometric magnitudes of the hot component from the following simple relations:

$$m_h = m_c + \Delta m,$$

$$m_c - m = \Delta m + 2.5 \log(1 + 10^{-0.4\Delta m}),$$

where m is the total brightness of the stars (maximum); m_h and m_c are the magnitudes of the hot and cool components, respectively. Solving the second equation numerically yielded the magnitudes of the bright component in each band. In Fig. 5, the relative depth of primary minimum is plotted against wavelength:

$$\Delta A_{U,B,R,I} = A_{U,B,R,I} - A_V.$$

This figure also shows the differences between the normal colors of B5 V and G2 III stars (Straĭzys 1977):

$$\Delta CI = CI_c - CI_h,$$

we assume that $V_h = V_c = 0$ to bring the zero points of the two dependences into coincidence.

As we see from Fig. 5, these zero points almost coincided except for the U band. The difference between the zero points in U is -0^m15, which matches
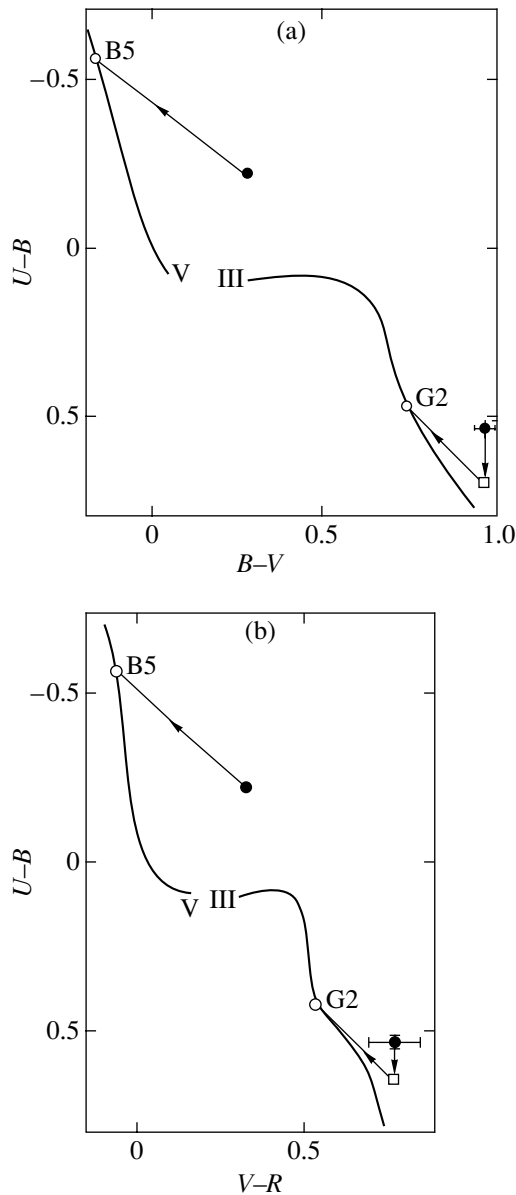
Fig. 4. Positions of the components of BZ Mon in the H–R diagram for single stars evolving toward the ZAMS, as calculated by Palla and Stahler (1993). The dashed line represents the 3×10^5-year isochrone. The birth line of stars is indicated by dots.

Fig. 3. Two-color (a) $(U–B)$, $(B–V)$ and (b) $(U–B)$, $(V–R)$ diagrams and positions of the components of BZ Mon. The filled circles are the components' true positions, the open circles are the components' positions in standard diagrams, and the square is the position of the cool component with an ultraviolet excess.

the ultraviolet excess of the cool component estimated in the two-color diagrams (Fig. 3). Thus, the spectral type of the cool component is G2 III, which is very close to G5 III obtained by Schaefer (1980).

The mass ratio of the CBS components is $q = 0.55$; the critical radii $r_{\text{h, cr}} = 0.431$ and $r_{\text{c, cr}} = 0.331$ of the hot and cool stars correspond to this ratio (Plavec and Kratochvil 1964). The radii of the stars account for 40 and 85% of their critical radii, respectively. A progressive change in period is observed in the system, sug-
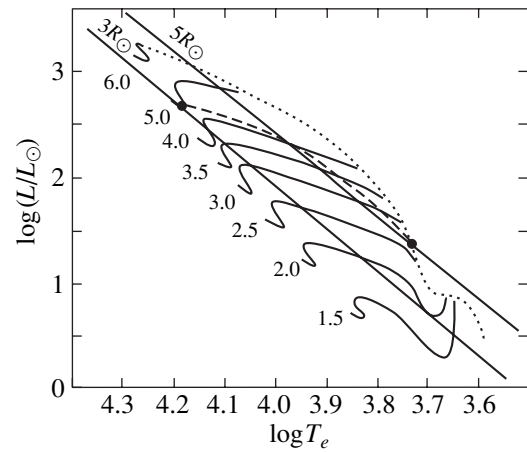
gesting mass loss by a component or by the system as a whole. If mass transfer from one component to the other takes place without mass loss by the entire system (a conservative process), then the direction in which the period changes is associated with the source of the mass loss (Batten 1976; Pribulla 1998). In BZ Mon, the period decreases and, for a conservative process, the flow of matter must be directed from the massive component to the secondary star. However, the hot component of the CBS is immersed deep into its Roche lobe, while the secondary component of the CBS fills 85% of its Roche lobe; as a result, one might expect mass outflow from the latter star. We believe that the flow of matter becomes nonconservative and mass is lost by the entire system; i.e., matter flows out of the cool component into the circumstellar space. The brightenings at maximum may result from mass ejections. These mass ejections can take place from the cool component as a very young star (age 3×10^5 years), and they cause the observed progressive decrease in CBS orbital period. The mass loss by the cool component may be transient and coupled with an active phase of young stars (Imhoff 1982; Grinin and Petrov 1989).

The hot star of BZ Mon exhibits the color excess $E_{B–V} = 0\overset{m}{.}45$ (Fig. 3a), and we obtain the visual absorption $A_V = 1\overset{m}{.}48$ for $R = 3.29$ (Straǐzys 1977). Assuming that the visual absolute magnitude of this component (spectral type B5 V) is $M_V = -0\overset{m}{.}8$ (Straǐzys 1982), we find the CBS distance modulus to be $11\overset{m}{.}6$. The distance to the CBS can also be estimated from the Barnes–Evans relation (Lacy 1977)

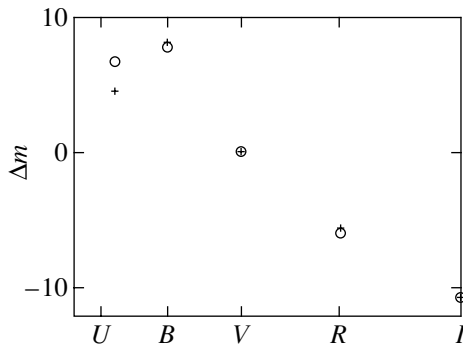$$F_V = 6.6576 - 0.1V_0 - 0.5\log R_* \pi",$$

Fig. 5. Relative depth of the primary minimum of BZ Mon (crosses) and the difference between the standard color indices of B5 V and G2 III stars (circles) versus wavelength.

where F_V is the star's surface brightness in V, V_0 is the apparent magnitude free from absorption, R_* is the radius (in km), and π'' is the parallax (in arcsec). We can calculate F_V (Lacy 1977) or use its tabulated values (Popper 1980). Substituting the data for the bright component of BZ Mon in the formula yields $m - M = 11\overset{m}{.}7$. The accuracy of this method depends on the accuracy of the input data; Lacy (1977) estimated it for well-observed CBSs to be $\pm 0\overset{m}{.}2$. The two independent methods yielded similar distances of BZ Mon.

As was noted above, the star is projected onto the region of the Mon OB2 association, and, according to the new breakdown of OB associations by Mel'nik and Efremov (1995), the distance to this association is 1.62 kpc, or its distance modulus is $m - M = 11\overset{m}{.}04$. Mel'nik and Efremov (1995) made a new breakdown of OB association in which BZ Mon falls within the Mon 1B region ($r = 1.48$ kpc or $m - M = 10\overset{m}{.}85$). Recently, Dambis *et al.* (2001) have made new distance determinations for OB associations and, in particular, found the distance to the Mon OB2 association to be $r = 1.5$ kpc ($m - M = 10\overset{m}{.}9$). Given the cosmic dispersion of the absolute magnitudes for B stars (Mdzinarishvili 1985) and the accuracy of the spectral classification for stars in two-color diagrams (Belyakina and Chugaĭnov 1960), the CBS distance modulus was found to be $11\overset{m}{.}6 \pm 0\overset{m}{.}6$. Taking into account the youth of the CBS components and their angular and spatial proximity to the Mon OB2 association, we believe BZ Mon to be a physical member of this star grouping.

CONCLUSION

A complete photoelectric *UBVR* light curve of the eclipsing variable BZ Mon in the star-forming region Mon OB2 has been constructed for the first time. A new formula was derived for the ephemeris of minima with a negative parabolic term. We detected low-amplitude

brightenings in the out-of-eclipse segments of the light curve, which are particularly pronounced in the red. Mass ejections from the cool component appear to take place, whose nature is similar to that of solar prominences. We analyzed all light curves of the star by Lavrov's method and obtained highly accurate photometric orbital elements. We calculated the photometric magnitudes of each component and estimated their spectral types and expected absolute parameters. BZ Mon was classified as a member of the OB association Mon OB2. Its age is 3×10^5 years.

REFERENCES

1. P. Ahnert, Mitt. Veröff. Sonnenberg, No. 39, 1 (1943).
2. P. Ahnert, C. Hoffmeister, E. Rohlfs, and A. van de Voorde, Veröff. Sternwarte Sonnenberg **1** (2), 117 (1947).
3. A. Batten, *Binary and Multiple Systems of Stars* (Pergamon, Oxford, 1973; Mir, Moscow, 1976).
4. T. S. Belyakina and P. F. Chugaĭnov, Izv. Krym. Astrofiz. Obs. **22**, 257 (1960).
5. J. Borovička, Inf. Bull. Var. Stars, No. 3877 (1993).
6. J. Borovička, Contrib. Obs. Plan. Brno, No. 31, 60 (1995).
7. A. K. Dambis, A. M. Mel'nik, and A. S. Rastorguev, Pis'ma Astron. Zh. **27**, 68 (2001) [Astron. Lett. **27**, 58 (2001)].
8. V. P. Grinin and P. P. Petrov, in *Modern Problems of Physics and Stellar Evolution*, Ed. by A. G. Masevich (Nauka, Moscow, 1989), p. 64.
9. C. Hoffmeister, Astron. Nachr. **259**, 37 (1936).
10. C. A. Imhoff, in *Protostars and Planets,* Ed. by T. Gehrels (Univ. of Arisona Press, Tucson, 1978; Mir, Moscow, 1982), p. 699.
11. K. Kordilewski, Ročn. Astron. (SAC), No. 31, 133 (1959).
12. C. H. Lacy, Astrophys. J. **213**, 458 (1977).
13. A. U. Landolt, Astron. J. **88**, 439 (1983).
14. M. I. Lavrov, Tr. Kazan. Gor. Astron. Obs. **53**, 34 (1993).
15. A. Maeder, Astron. Astrophys. **47**, 389 (1976).
16. A. Maeder and C. Mermilliod, Astron. Astrophys. **93**, 136 (1981).
17. A. G. Masevich and A. V. Tutukov, *Stellar Evolution: Theory and Observations* (Nauka, Moscow, 1988).
18. T. G. Mdzinarishvili, Byull. Akad. Nauk Gruz. SSR, Abastumanskaya Astrofiz. Obs. **59**, 117 (1985).
19. A. M. Mel'nik and Yu. N. Efremov, Pis'ma Astron. Zh. **21**, 13 (1995) [Astron. Lett. **21**, 10 (1995)].

20. F. Palla and S. W. Stahler, Astrophys. J. **418**, 414 (1993).

21. M. Plavec and P. Kratochvil, Bull. Astron. Inst. Czech. **15** (5), 171 (1964).

22. D. M. Popper, Annu. Rev. Astron. Astrophys. **18**, 115 (1980).

23. T. Pribulla, Contrib. Astron. Obs. Skalnate Pleso **28**, 101 (1998).

24. A. A. Rubashevskiĭ, Byull. Akad. Nauk Gruz. SSR, Abastumanskaya Astrofiz. Obs. **58**, 389 (1985).

25. J. Sahade and F. D. Beron, Ann. Astrophys. **26**, 153 (1963).

26. B. E. Schaefer, J. Am. Assoc. Var. Star Obs. **9** (1), 45 (1980).

27. I. Semeniuk, Acta Astron. **12**, 122 (1962).

28. V. Straĭzys, *Multicolor Stellar Photometry* (Mokslas, Vilnius, 1977; Pachart Publ. House, Tucson, 1992).

29. V. Straĭzys, *Metal-Deficient Stars* (Mokslas, Vilnius, 1982).

30. M. A. Svechnikov and É. F. Kuznetsova, *A Catalog of Approximate Photometric and Absolute Elements of Variable Stars* (Ural'skiĭ Goc. Univ., Sverdlovsk, 1990), Vol. 2.

31. M. M. Zakirov, Inf. Bull. Var. Stars, No. 3925 (1993).

32. M. M. Zakirov, Pis'ma Astron. Zh. **22**, 664 (1996) [Astron. Lett. **22**, 593 (1996)].

33. A. I. Zheleznyakova, *Astronomical Climate and Telescope Efficiency* (Nauka, Leningrad, 1984), p. 55.

Translated by V. Astakhov